GEORG-AUGUST-UNIVERSITÄT GÖTTINGEN

II. Physikalisches Institut

ATLAS High-Level Muon Trigger Studies

Development of a Method to Extract Trigger Efficiencies from Data

von

Fabian Kohn

This thesis aims at the development of a quantitative method to measure Trigger efficiencies from data without the need to rely on Monte Carlo simulations for the efficiency measurement itself. Moreover, it should be possible to take into account arbitrary background normalisations for efficiency measurement.

Post address:
Friedrich-Hund-Platz 1
37077 Göttingen
Germany

II.Physik-UniGö-Dipl-2008/02
II. Physikalisches Institut
Georg-August-Universität Göttingen
April 2008

GEORG-AUGUST-UNIVERSITÄT

GÖTTINGEN

II. Physikalisches Institut

ATLAS High-Level Muon Trigger Studies

Development of a Method to Extract Trigger Efficiencies from Data

von

Fabian Kohn

Dieser Forschungsbericht wurde als Diplomarbeit von der Fakultät für Physik der Georg-August-Universität zu Göttingen angenommen.

Angenommen am:	25. April 2008
Referent:	Prof. Dr. Arnulf Quadt
Korreferent:	Prof. Dr. Markus Klute

II.Physik-UniGö-Dipl-2008/02

Contents

1 Introduction

1.1 The Standard Model of Particle Physics

Physicists all over the world have always tried to understand the fundamental building blocks of matter and the forces that bind them together, making an effort to analyse the properties of elementary particles and their interactions to unprecedented precision. Hence, the Standard Model of Particle Physics [1–6] is evidently one of the best understood theories in physics, with almost all experimental effects observed up to date being in agreement with their predictions.

Within the Standard Model, the fundamental particles and interactions are described by a relativistic quantum field theory which is consistent with both quantum mechanics and special relativity combining the electroweak theory and quantum chromodynamics into a structure denoted by the gauge groups $\mathrm{SU}(3) \times \mathrm{SU}(2) \times \mathrm{U}(1)$.

The theory constitutes all matter to consist of leptons and quarks, which can be classified into three generations or families, as can be seen in Figure F-1.1. The first generation, which all visible stable matter is made of, is constituted by the Up (u) and Down (d) quark doublet (the building blocks of proton and neutron) alongside with the electron (e) and the electron-neutrino (ν_e).

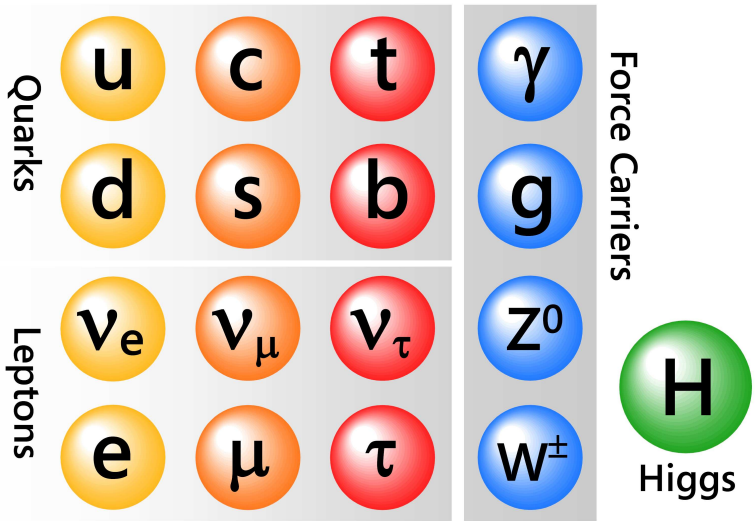

Figure F-1.1: The particle content of the Standard Model of Particle Physics. Aside from the quarks (upper left box) and leptons (lower left box), the force carrier particles (right vertical box) and the postulated Higgs boson are shown.

The second generation is made up by the Charm (c) and Strange (s) quarks as well as the muon (μ), being observed in cosmic radiation, and the muon-neutrino (ν_μ).

Finally, the Top (t) and Bottom (b) quark compose the third generation, together with the tau (τ) and the tau-neutrino (ν_τ) in the lepton sector. Moreover, the Top quark (the last of the six quarks, which was discovered in 1995 [7, 8]) assumes a quite distinct role among the other quarks due to its large mass which exceeds the mass of the heaviest of the other quarks (the

Bottom quark) by a factor of about 40, resulting in a very short lifetime making it impossible for the Top quark to form hadronic bound states.

In addition to quarks and leptons (which are fermions), the interactions between them are mediated by force carrier particles (bosons), representing the underlying relativistic quantum field theories. Among these, the photon carries the electromagnetic force. Furthermore, the $W^{\pm}$ and Z^0 bosons are the mediators of the weak force. These bosons are the only force particles to carry a mass, that is why they are called *heavy* gauge bosons. The strong force is carried by the eight gluons, binding quarks together and confining nuclei despite their positively charged protons. Being only effective over short distances in the range of $2.5 \cdot 10^{-15}$ m due to the non-abelian structure of the underlying quantum theory, the strong force exceeds the electromagnetic force by a factor of about 100 in amount at this range (depending on momentum transfer).

Finally, gravitation is not yet understood on a quantum theory level, thus not being included in the Standard Model.

Aside from the fundamental forces, the hypothetical Higgs boson [9,10] is theorised to give rise to mass itself among all particles, where the mass corresponds to the coupling strength of the respective particle to the Higgs. Since the Higgs Boson is the only Standard Model particle that has not yet been observed experimentally, its discovery and the determination of its properties is one of the central goals of current and future Particle Physics experiments.

Tables T-1.1, T-1.2 and T-1.3 summarise all described particles and their properties. For further reading on the Standard Model, see [11, 12].

Leptons (spin $s = \frac{1}{2}$)			
Flavour		**Mass [MeV]**	**Charge**
(ν_e)	e neutr.	$< 1 \cdot 10^{-5}$	0
(e)	electron	0.511	-1
(ν_μ)	μ neutr.	< 0.19	0
(μ)	muon	105.658	-1
(ν_τ)	τ neutr.	< 18.2	0
(τ)	tau	1776.9 ± 0.2	-1

Table T-1.1: Leptons [13]

Quarks (spin $s = \frac{1}{2}$)			
Flavour		**Mass [MeV]**	**Charge**
(u)	up	3.0 to 7.0	$\frac{2}{3}$
(d)	down	1.5 to 3.0	$-\frac{1}{3}$
(c)	charm	1250 ± 90	$\frac{2}{3}$
(s)	strange	95 ± 25	$-\frac{1}{3}$
(t)	top [14]	$(172.6 \pm 1.4) \cdot 10^3$	$\frac{2}{3}$
(b)	bottom	$(4.20 \pm 0.07) \cdot 10^3$	$-\frac{1}{3}$

Table T-1.2: Quarks [13]

Bosons (integer spin)				
Particle		**Mass [GeV]**	**Charge**	**Spin**
(γ)	Electromagn. force	0	0	1
(g)	Strong force	0	0	1
(W^-)		80.403 ± 0.029	-1	1
(W^+)	Weak force	80.403 ± 0.029	$+1$	1
(Z^0)		91.188 ± 0.003	0	1
(H)	Mass (hypoth.)	> 114.4	0	0

Table T-1.3: Bosons [13]

Despite the Standard Model being very successful in explaining the fundamental particles and interactions, it is not without flaws. There are still several open questions left to be answered some of which are covered in the following breakdown, which is by far not exhaustive:

- Why are the strengths of the fundamental forces (electromagnetism, weak and strong forces, and gravity as well (even if it is not included in the Standard Model)) what they are? Furthermore, is there a Grand Unification at a GUT (*Grand Unified Theory* [15]) scale combining all forces and their couplings, similar to the Electroweak Unification at the weak scale?

- Why do we observe an excess of matter in our present universe although matter and antimatter should have been created equally during the process of the Big Bang, thus annihilating and leaving behind a universe containing photons only. Or is there antimatter we just do not observe? And though it is true that the Standard Model comprehends the phenomenon of charge-parity violation that can explain this asymmetry, we are not yet able to describe the exact magnitude of this effect.

- It can be shown that the fraction of visible matter in the universe is much lower than the total amount of matter that must necessarily exist to explain the motion of galaxies and stars within space (the visible fraction is believed to constitute only about 4 % of all matter and energy in the universe). The invisible *dark matter*, which is theorised to constitute a fraction of about 23 % of the total amount of matter and energy in the universe (with the remaining 73 % consisting of *dark energy*), is eagerly being searched for and thus is part of many recent studies in both Particle Physics and Astrophysics as well [16].

As a matter of fact, finding the answers to these questions is crucial in order to fully understand the Standard Model and physics beyond it as well. This can be achieved by making use of particle accelerators, colliding highly energetic particles and measuring their properties with particle detectors. In this context, advancing into new regions of physics (that is, higher particle masses and therefore energies) is only possible by increasing both centre-of-mass energy and collision rate as well (in order to enhance statistics to compensate for new physics events occurring so rarely) with respect to former accelerator machines. Hence, the development and construction of a new machine to cope with these challenges is the logical consequence.

1.2 The Large Hadron Collider & The ATLAS Detector

The Large Hadron Collider (LHC) [17] is currently being built at CERN, the European Centre for Nuclear Research near Geneva, Switzerland, and will be the technologically most advanced particle accelerator so far. One of its main goals is to shed light upon the many unanswered questions that were mentioned earlier.

The LHC is designed as proton-proton accelerator with the potential to accelerate heavy ions as well. Its construction started in 1999 and its operation is scheduled to start in the course of 2008. The collider is being built in the former accelerator ring of the Large Electron Positron Collider (LEP), being about 27 kilometres in circumference and 100 to 125 metres below ground level, partly making use of the already existing infrastructure of the LEP ring as well as two existing caverns.

The accelerator complex will incorporate six experiments, two of them being multi-purpose experiments (ATLAS [19] & CMS [20]), while the other four were designed for particular fields

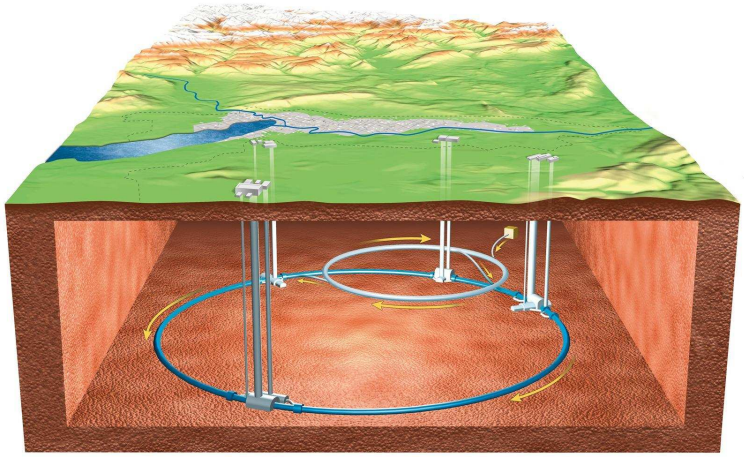

Figure F-1.2: Layout of the LHC tunnel. [18]

of research. Having two independently designed multi-purpose detectors is vital for cross-confirmation of any potential new discoveries made and allows to combine the results of both experiments. Among the four other detectors, LHCb [21] focuses on b physics, while the ALICE [22] experiment is conceived for heavy ion physics. TOTEM [23] and LHCf [24] both concentrate on forward physics.

The ATLAS (*A Toroidal LHC ApparatuS*) detector will investigate a wide range of physics, including the search for the Higgs boson, extra dimensions, and particles that could make up dark matter.

The ATLAS collaboration involves (as of Jan./Feb. 2008) about 2100 scientists and engineers (including 450 students) from 167 institutions and 37 countries all over the world [25].

The detector features an onion-like structure, which will be discussed in detail in Chapter 2. However, the unprecedented requirements of the Large Hadron Collider – extremely high energy and collision rate, both being crucial to advance into regions of new physics – require the ATLAS detector to be even more complex and powerful than any detector ever built.

1.3 Trigger Overview

At the LHC, bunches of protons will collide every 25 ns. Together with a total amount of direct proton - proton collisions of 23 per bunch in nominal operation this sums up to a total interaction rate of 1 GHz. Given the ATLAS event data size to be about 1.6 Megabyte [26], the unfiltered data rate would be in the range of $1.6 \cdot 10^{15}$ bytes ($\sim$1 Petabyte) per second and a theoretical annual cumulative in the range of 10^{22} bytes respectively.

This assessment clearly shows the infeasibility to store all the data on tape (or any other storage medium) from the point of data transfer rates and storage size considerations as well.

On the other hand, the estimated rate of new physics according to the design parameters is in the mHz regime and below, making it necessary to select the fraction of one interesting interaction in 10^{12} events and store it on tape in order to facilitate analysis. Since this selection has to be conducted during run-time, the stated challenges give rise for a sophisticated online selection system, the *ATLAS Trigger System*. Its functionality and technical details will be covered in Chapter 2.4.

This thesis is aimed at the development of a method to measure the efficiency of the Trigger System (in particular the Muon Trigger) with respect to different conditions and dependencies and – even more important – the corresponding statistical and systematic uncertainties. The developed method should be capable of determining the Trigger efficiency for any specific physics process or a single object from a data sample without the need to rely on simulations for the efficiency measurement itself.

The document is structured as follows: In Chapter 2, the detector and its subsystems are explained in detail. Chapter 3 focuses on the development of the method itself and its verification, while Chapter 4 is reserved for the results of the method being applied to several simulated physics samples. Finally, a conclusion is drawn in Chapter 5.

2 Experimental Setup

This Chapter deals with the technical details of the LHC collider and the ATLAS experiment, focusing on the detector subsystems and their properties after a short general overview. In addition, the ATLAS Trigger System is explained in more detail with respect to technical and functional parameters.

2.1 LHC & ATLAS Technical Overview

The two LHC proton beams deliver a beam energy of 7 TeV each and bunches of about 10^{11} protons are brought to collision at a bunch crossing rate (BCR) of 40 MHz within one of the LHC particle detectors. One possibility to characterise the particle beam is to introduce the instantaneous Luminosity $\mathcal{L}$, which relates the cross section σ of a given process to the corresponding event rate R:

$$\mathcal{L} = \frac{R}{\sigma} \tag{2.1}$$

At the design Luminosity of $\mathcal{L} = 10^{34}\,\mathrm{cm}^{-2}\mathrm{s}^{-1}$ and for the given beam parameters, this leads to a total of roughly 23 proton - proton collisions per bunch crossing on average, that is an overall interaction rate in the GHz regime.

The ATLAS detector is 46 m in length, 25 m in height and 25 m in width, with a total weight of about 7 000 tons. As a comparison, CMS, the second LHC multi-purpose experiment weighs about 12 500 tons while being 21 m long, 15 m wide, and 15 m high.

A summary of the ATLAS and the LHC specifications to other accelerator/detector combinations is shown in Table T-2.1.

	Type	$\sqrt{s}$	**BCR**	N_{CH}	**Event Size**	**Year**
ATLAS, LHC (CERN)	p - p	14 TeV	40 MHz	$\sim 10^8$	~ 1600 kB	2008
CDF/DØ, Tevatron[1](FNAL)	p - $\overline{\mathrm{p}}$	1.960 TeV	2.5 MHz	$\sim 10^6$	~ 250 kB	2001
ZEUS, HERA (DESY)	$\mathrm{e}^{\pm}$ - p	0.318 TeV	10 MHz	$\sim 10^5$	~ 100 kB	1992

Table T-2.1: Comparison of LHC/ATLAS to other accelerators/detectors. Shown are the particle types brought to collision, the centre-of-mass energy $\sqrt{s}$, the bunch crossing rate (BCR), the amount of readout channels (N_{CH}), the average event size and the year of startup.

As can be seen from the table, the LHC collides protons on protons in normal operation mode instead of using protons and antiprotons like it is done at the Tevatron. This is due to the fact that the production of new particles from the collision is dominated by gluon interaction in the energy regime of the LHC, while production at lower centre-of-mass energies is dominated by quark-antiquark annihilation, according to the proton structure function [27]. Hence, colliding

[1] Tevatron Run II

protons on antiprotons at LHC energies would not increase the total cross-section substantially compared to proton-proton reactions. In addition, despite the fact that a proton-antiproton collider has the advantage of being able to keep both counter-rotating beams in the same beam pipe, production of the large quantities of antiprotons required for the high design Luminosity is not practicable and would in fact be more expensive than a proton-proton solution with separate beam pipes.

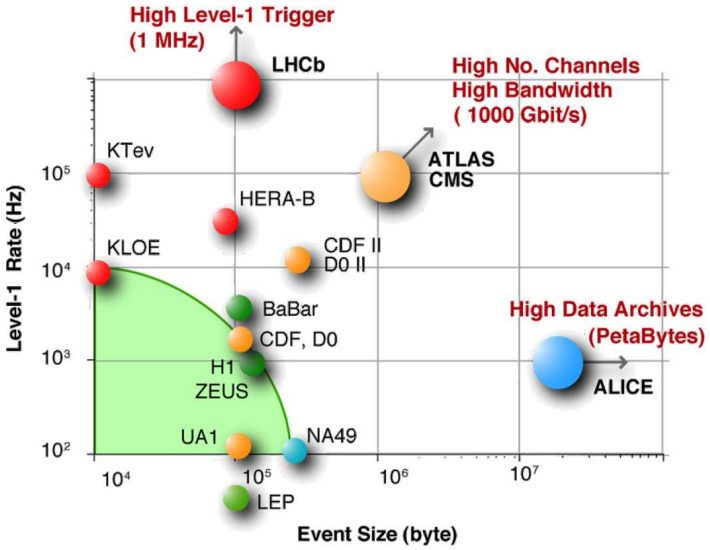

Figure F-2.1: Event size (amount of data per event in bytes) and initial data rate after the first Trigger level for several former, current and future experiments. Depending on the experiment and the collider, there exist different requirements with respect to Trigger rate and bandwidth.

As can be seen from the comparison table as well as from Figure F-2.1, not only do the LHC and ATLAS, respectively, exceed the bunch crossing rate of the largest particle accelerator up to date (Tevatron in RUN II, Fermi National Accelerator Laboratory) by a factor of seven. Furthermore, the amount of detector readout channels increased by two orders of magnitude alongside with the average event size increasing by about one order of magnitude, resulting in a much higher total raw data throughput rate the readout and data acquisition system has to cope with.

As a consequence, a sophisticated Trigger System focused on the reduction of collision and data rates is needed to facilitate analysis. This can only be achieved by selecting only a subset of interesting events out of the large amount of collisions that take place at LHC/ATLAS.

2.2 ATLAS Coordinate Frame

The ATLAS coordinate system is a right-handed coordinate frame with the x-axis pointing towards the centre of the LHC ring and the z-axis being directed along the beam pipe, while the y-axis points upwards (slightly tilted with respect to vertical (0.704 °) due to the general tilt of the tunnel). In this context, the pseudorapidity can be introduced as

$$\eta = -\ln \tan \frac{\theta}{2} \tag{2.2}$$

with θ being the azimuthal angle with respect to the positive y-axis. The advantage of this detector variable lies in the invariance of pseudorapidity intervals under Lorentz transformations.

In addition, the transverse momentum p_{T} of a particle in the detector is defined as the momentum perpendicular to the z-axis:

$$\vec{p}_{\mathrm{T}} = \begin{pmatrix} p_x \\ p_y \end{pmatrix} \quad ; \quad p_{\mathrm{T}} = \sqrt{p_x^2 + p_y^2} \tag{2.3}$$

2.3 The ATLAS Detector Subsystems

In order to allow for reliable detection of particles and measurement of their properties, the ATLAS detector requirements include:

- Good hermiticity with respect to detector acceptance.
- High spatial and timing resolution, in particular to minimise occupancy of individual detector components, to measure p_{T} with high resolution and to allow for distinguishment between different particles.
- Low material budget to minimise particle interaction with detector components where not required for detection itself (which is only the case for calorimetry).

ATLAS has a cylindrical shape with layers of detector components stacked onto each other. Each of these layers is designed to detect different types of particles which are mostly originating from the primary interaction point of the proton beams at the centre of ATLAS. As they travel

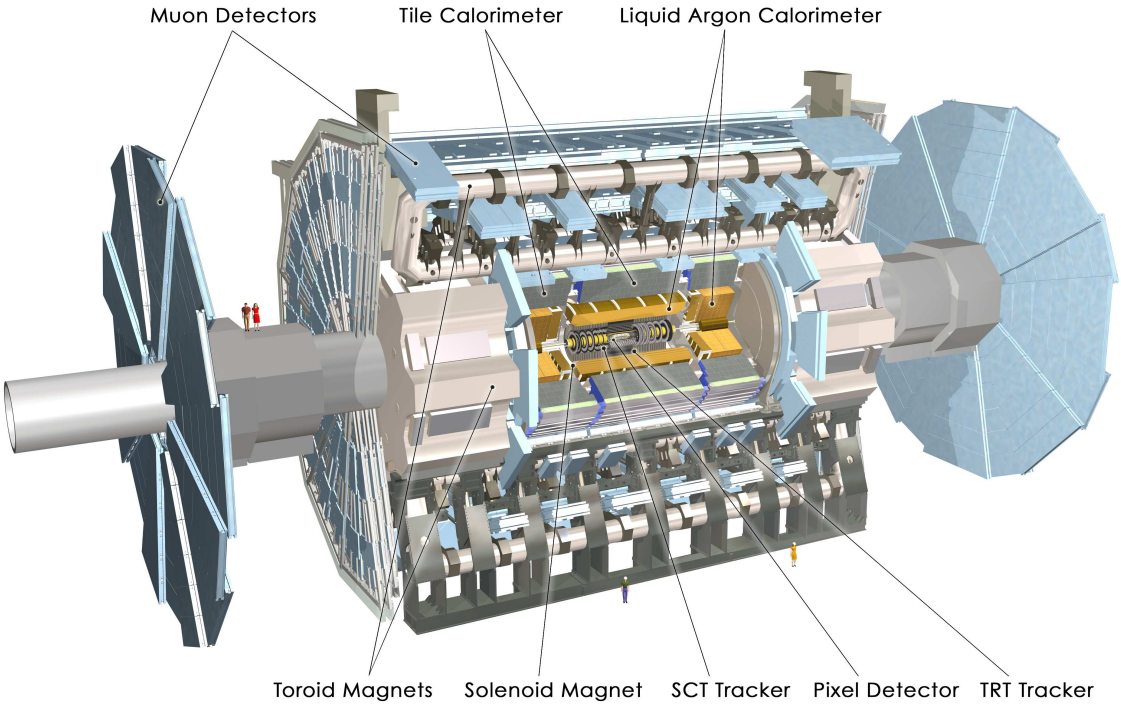

Figure F-2.2: ATLAS detector subsystems [25]

throughout the detector, they can be measured by its successive layers. These different detector layers or subsystems are shown in Figure F-2.2. That is, from the innermost to the outermost layer:

- The Inner Detector,
- The Solenoid Magnet,
- The Electromagnetic Calorimeter,
- The Hadronic Calorimeter,
- The Toroidal Magnet,
- The Muon Spectrometer.

The detectors are complementary: Charged particles are detected in the innermost layers by their hits in the tracking chambers, the particle tracks being bent by the magnetic field of the superconducting Solenoid Magnet. With this tracking information, the momentum of the particles can be determined. Around the magnet, the Electromagnetic and Hadronic Calorimeters are designed to measure the energy of particles. These are brought to a stop in the calorimeter by characteristic interaction (ionisation) with the detector material [13], thus depositing all of their energy in the optimal case, which is measured by the calorimeter cells. Finally, the Muon Chambers perform additional momentum measurements of muons penetrating all other layers of the detector only depositing very little energy in the material. This measurement is again conducted from the shape of the tracks in the Muon Chambers being bent by the magnetic field of the Toroidal Magnets.

2.3.1 Inner Detector

In the following, the Inner Detector [28, 29] is described in more detail. It is situated near the interaction point to allow for high precision measurement of charged particle trajectories. It covers a pseudorapidity range of ± 2.5 and consists of three subsystems:

- The Silicon Pixel Detector,
- The Semiconductor Tracker (SCT),
- The Transition Radiation Tracker (TRT).

The innermost layers of the Inner Detector (three in the cylindrical barrel region, three endcap disks on each side of the forward region) constitute the Pixel Detector which is designed to measure particle vertices and track momenta. Due to its location in close proximity to the primary interaction point, a very high spatial resolution of the Pixel Detector is required, which is achieved by very small pixel sizes of $50\,\mu\text{m} \times 400\,\mu\text{m}$ ($1.4 \cdot 10^8$ readout channels), with the Pixel Detector covering a total area of $2.3\,\text{m}^2$.

Around the Pixel Detector, the Semiconductor Tracker (or *Silicon Strip Tracker*) measures the momentum of charged particles. It is build out of four barrel layers and nine endcap wheels on each side, taking up a total area of $61.1\,\text{m}^2$ and making use of $6.3 \cdot 10^6$ readout channels.

The outermost part of the Inner Detector is constituted by the Transition Radiation Tracker, which consists of straw tubes filled with an ionisable gas with a diameter of 4 mm and a maximum length of 80 cm, where the barrel tubes are divided in two at the centre and read out at each

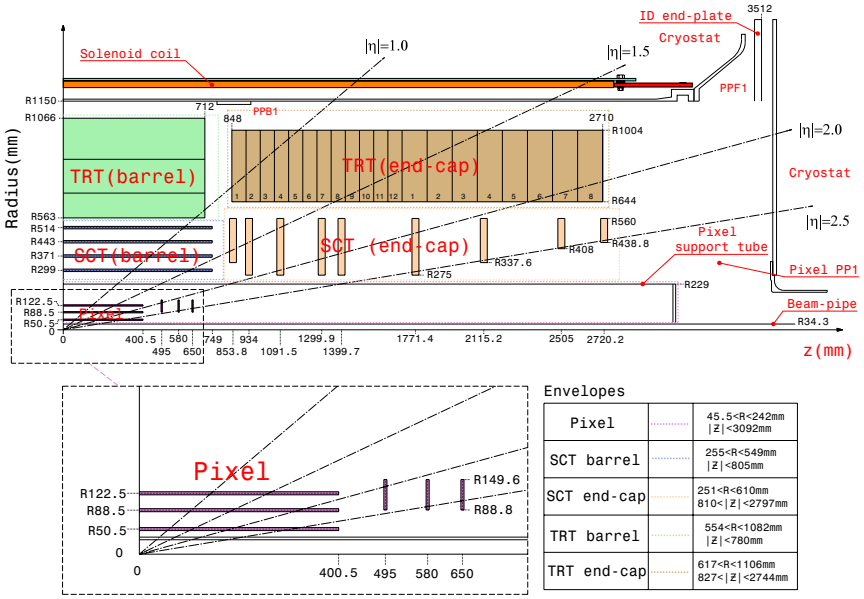

Figure F-2.3: Plan view of a quarter-section of the ATLAS Inner Detector showing each of the major detector elements alongside with its active dimensions and envelopes [29].

end to reduce occupancy. The ionisation charges created by charged particles travelling through the gas filled tubes are used to enhance track pattern recognition and to improve momentum resolution of the Pixel Detector and Semiconductor Tracker with an additional average of 36 hits per track. On top of that, its function is to distinguish electrons and pions using the different amount of Transition Radiation [30] photons emitted by these particles when crossing the interface of two media with different dielectric constants (in this case a special radiator foam with a large amount of air bubbles). The Transition Radiation Tracker has a total of 351 000 readout channels.

The resulting tracking performance of the Inner Detector subsystems for single particles and particles in jets can be found in Table T-2.2.

Track Parameter	$\mathbf{0.25 < \lvert\eta\rvert < 0.50}$		$\mathbf{1.50 < \lvert\eta\rvert < 1.75}$	
	$\boldsymbol{\sigma_X(\infty)}$	$\boldsymbol{p_X}$**[GeV]**	$\boldsymbol{\sigma_X(\infty)}$	$\boldsymbol{p_X}$**[GeV]**
Momentum $(1/p_{\mathrm{T}})$	$0.43\,\mathrm{TeV}^{-1}$	31.0	$0.48\,\mathrm{TeV}^{-1}$	64.0
Azimuthal angle (ϕ)	80 µrad	35.0	95 µrad	49.0
Polar angle $(\cos\theta)$	0.7×10^{-3}	5.3	1.1×10^{-3}	10.0
Transv. impact parameter (d_0)	10.5 µm	16.0	12.8 µm	20.0
Longit. impact parameter $(z_0 \times \sin\theta)$	100 µm	2.2	87 µm	3.9

Table T-2.2: Expected track-parameter resolutions at infinite momentum $\sigma_X(\infty)$ and the transverse momentum p_X for which the intrinsic and multiple-scattering contribution equals the intrinsic resolution. The momentum and angles correspond to muons, while the impact parameters correspond to pions. The values are shown for two η regions, one in the barrel Inner Detector (where the amount of material is close to its minimum) and one in the endcap (where the amount of material is close to its maximum, cf. Figure F-2.4) [29].

Furthermore, Figure F-2.4 shows the material distribution of the Inner detector with respect to radiation lengths X_0 (the mean distance over which a high-energy electron looses all but 1/e of its energy by Bremsstrahlung as well as 7/9 of the mean free path for pair production by a high-energy photon [13]) and interaction lengths λ (the mean free path of a particle before undergoing an interaction that is neither elastic nor quasi-elastic (diffractive), in a given medium).

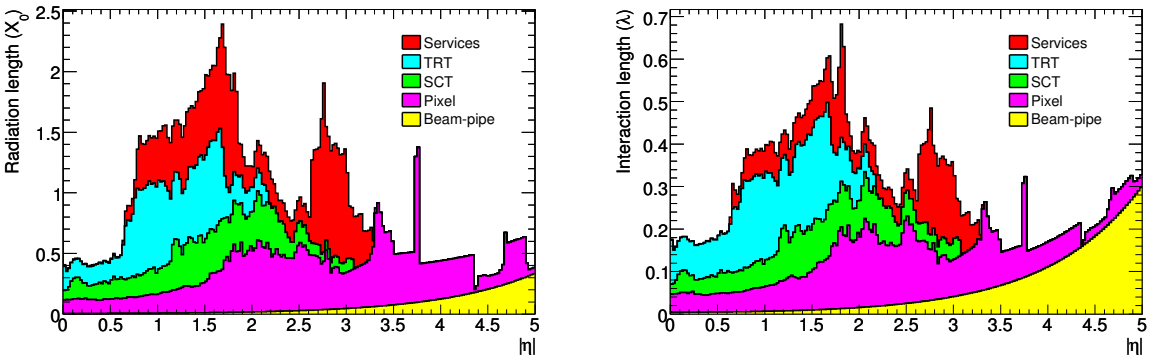

Figure F-2.4: Material distribution at the exit of the Inner Detector envelope, including the services and thermal enclosures. The distributions are shown as a function of $|\eta|$ and are averaged over ϕ. The breakdown indicates the contributions of external services and of individual sub-detectors, including services in their active volume [29]. Left: Radiation length X_0; Right: Interaction length λ.

2.3.2 Calorimeters

Around the Solenoid Magnet (which is described in more detail in the *Magnet System* section of this chapter), an electromagnetic (EM) liquid argon calorimeter detects and identifies electromagnetically interacting particles and measures their energy [19, 29, 31, 32]. It also provides, in combination with the Hadronic Calorimeters, for reconstruction of hadronic jets and measurement of the missing energy of an event.

The EM Calorimeter covers an η range of ± 3.2 and comprises several layers of accordion-shaped kapton-copper electrodes and stainless steel-clad lead absorber plates, with the gaps in between filled with liquid argon at a temperature of 87 K. Whenever an electromagnetically interacting particle passes through one of the lead absorber plates, it creates a particle shower that ionises the liquid argon. Exposed to the detector's magnetic field, the ionisation charge drifting in the liquid argon induces a signal in the electrodes by capacitive coupling. The resulting signal is sampled and digitised with 40 MHz, according to the bunch crossing rate. The EM Calorimeter has a total of 170 000 readout channels, and provides an energy resolution of

$$\frac{\sigma_{\mathrm{EM}}^{\mathrm{sp}}}{E} = \frac{(10.1 \pm 0.4)\,\%}{\sqrt{E\,[\mathrm{GeV}]}} \text{ (stochastic) and } 0.2 \pm 0.1\,\% \text{ (constant)},$$

as measured in particle beam tests [29] and a total module thickness in the barrel region of at least 22 radiation lengths (X_0), increasing from $22\,X_0$ to $30\,X_0$ between $|\eta| = 0$ and $|\eta| = 0.8$ and from $24\,X_0$ to $33\,X_0$ between $|\eta| = 0.8$ and $|\eta| = 1.3$. In the endcaps, the total active thickness is greater than $24\,X_0$ except for $|\eta| < 1.475$, increasing from $24\,X_0$ to $38\,X_0$ in the outer wheel

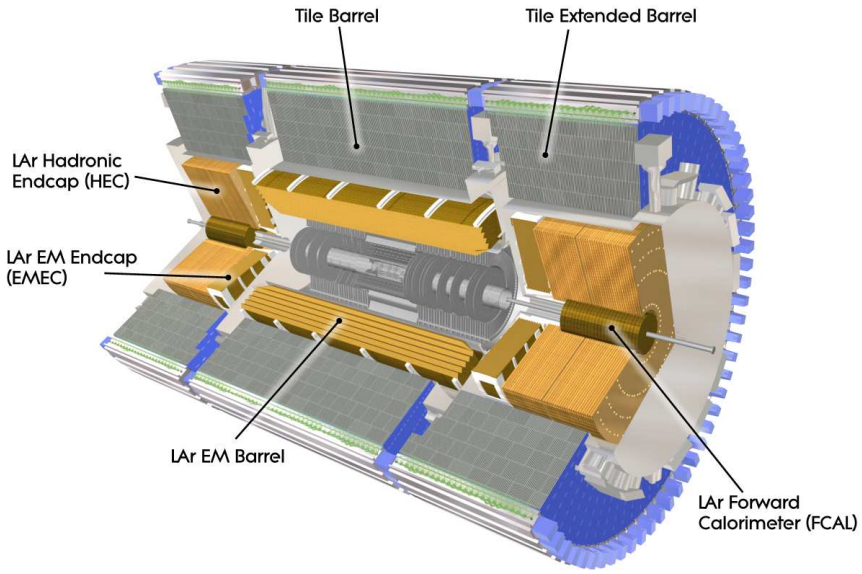

Figure F-2.5: Overall layout of the ATLAS Calorimeters [29].

($1.475 < |\eta| < 2.5$) and from $26\,X_0$ to $36\,X_0$ in the inner wheel ($2.5 < |\eta| < 3.2$). This is shown in more detail in Figure F-2.6, where the cumulative material amount for the calorimeter system is plotted for the individual subsystems.

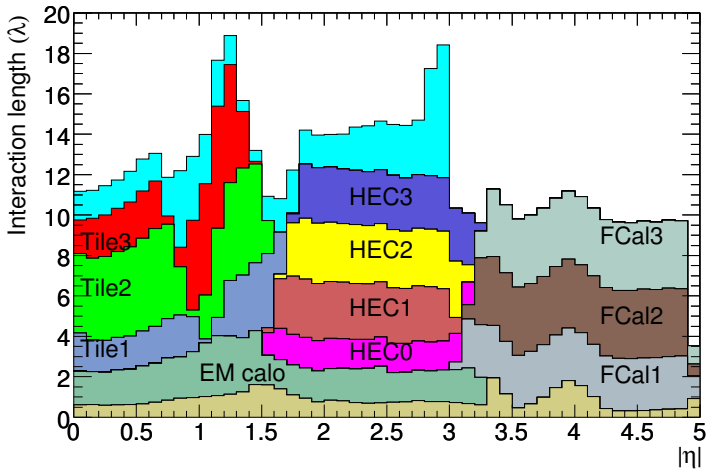

Figure F-2.6: Cumulative amount of material for the calorimeter system in units of interaction lengths λ as a function of $|\eta|$ for the different calorimeter subsystems. Abbreviations: Tile$X$ - Tile Calorimeter compartment X; HECX - Hadronic Endcap compartment X; FCal$X$ - Forward Calorimeter compartment X. The topmost contribution is the total amount of material in front of the first active layer of the Muon Spectrometer (up to $|\eta| < 3.0$), shown for completeness [29].

In analogy, the Hadronic Calorimeter (hCAL) [19,29,31] is designed to measure the energy of hadronic particles that can penetrate the Electromagnetic Calorimeter. This sampling calorimeter consists of iron absorbers for showering which are interleaved with plastic scintillator tiles

(thus being referred to as *tile calorimeter*) in the barrel-shaped part of the detector ($|\eta| < 1.7$). The scintillator tiles emit a shower of photons whenever charged particles pass through them due to excitation of the atoms in the scintillating material and subsequent emission of visible or UV photons. These light pulses are carried by optical fibres to photomultiplier tubes and converted to an electric signal, where the total number of Tile Calorimeter readout channels is of the order 10 000.

Due to the scintillating tiles being very sensitive to radiation damage, in the forward endcap regions ($1.5 < |\eta| < 3.2$) liquid argon is used again as sampling medium in close proximity to the proton beams alongside with copper absorbers, providing better radiation hardness. The total number of channels for both endcaps is 5 632. For the same reason, a high density copper/tungsten absorber liquid argon Forward Calorimeter (FCAL) covers the pseudorapidity region $3.1 < |\eta| < 4.9$, with an additional 3 524 channels for both forward regions together.

For estimates of the performance of the Hadronic Calorimeter, beam tests were conducted, showing an energy resolution of

$$\frac{\sigma_\pi^{\mathrm{HAD}}}{E_\pi} = \frac{(56.4 \pm 0.4)\,\%}{\sqrt{E\,[\mathrm{GeV}]}} \text{ (stochastic) and } 5.5 \pm 0.1\,\% \text{ (constant)}$$

for pions, and a radial depth of approximately 7.4 interactions lengths (λ) for the tile calorimeter. The hadronic endcaps show an energy resolution of

$$\frac{\sigma_e^{\mathrm{HEC}}}{E_e} = \frac{(21.4 \pm 0.1)\,\%}{\sqrt{E\,[\mathrm{GeV}]}} \text{ (stochastic) (constant term compatible with zero)}$$

for electrons, and

$$\frac{\sigma_\pi^{\mathrm{HEC}}}{E_\pi} = \frac{(70.6 \pm 1.5)\,\%}{\sqrt{E\,[\mathrm{GeV}]}} \text{ (stochastic) and } 5.8 \pm 0.2\,\% \text{ (constant)}$$

for pions.

The jet energy resolution for the overall calorimeter system for central jets in the region $0.2 < |\eta| < 0.4$ is described by the parametrisation

$$\frac{\sigma_{\mathrm{jet}}}{E_{\mathrm{jet}}} = \sqrt{\frac{a^2}{E_{\mathrm{jet}}} + \frac{b^2}{E_{\mathrm{jet}}^2} + c^2},$$

with $a \approx 60\,\%\sqrt{\mathrm{GeV}}$ (stochastic), $c \approx 3\,\%$ (constant) and the noise term b increasing from 0.5 GeV to 1.5 GeV from barrel to endcap ranges.

The cumulative amount of material for the Hadronic Calorimeter and the Forward Calorimeter can be found in Figure F-2.6 as well.

2.3.3 Muon Chambers

Finally, the Muon Chambers [19, 29, 33] are designed to detect muons, which are able to pass all other detector systems depositing only a small amount of energy in the material. This is due to the fact that muons in the GeV regime are minimum ionising particles, which can be seen in Figure F-2.7, where the stopping power for positive muons in copper is shown, which is defined as the average differential energy loss per distance, $\langle -dE/dx \rangle$.

Being deflected by the magnetic field in the detector, it is possible to determine the muon momentum and sign of electric charge by measuring the trajectories of the muons as they pass

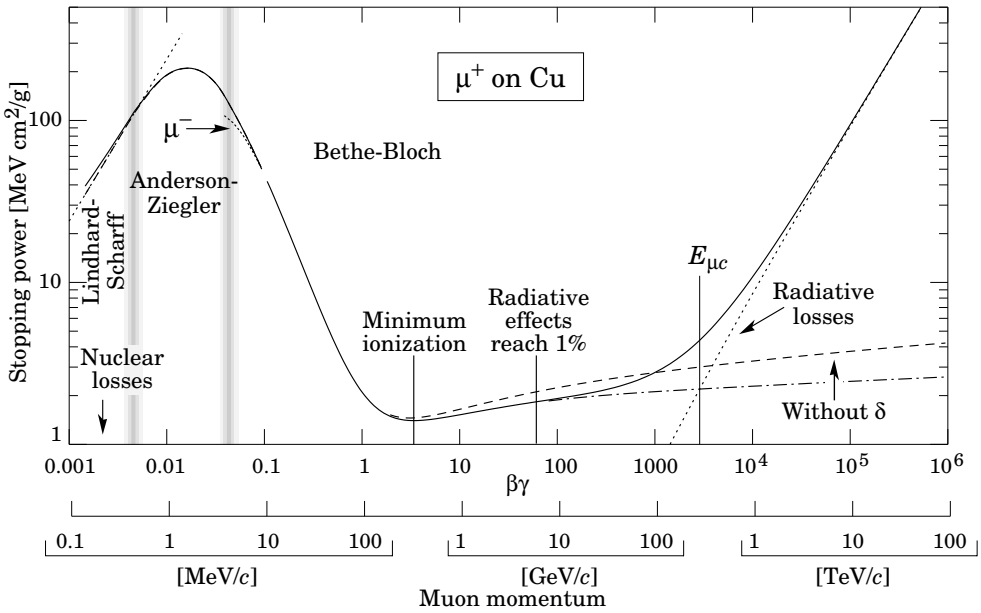

Figure F-2.7: Average energy loss per distance $\langle -dE/dx \rangle$ (stopping power) for positive muons in copper as a function of $\beta\gamma = p/Mc$. The solid curve indicates the total stopping power. Data below $\beta\gamma \approx 0.1$ are taken from ICRU 49 [34], and data at higher energies are from [35]. Vertical bands indicate boundaries between different approximations. The short dotted lines labelled μ^- illustrate the *Barkas effect*, the dependence of stopping power on projectile charge at very low energies [36]. Muons from interesting processes are expected to be mainly produced in the GeV regime, which means that they are minimum ionising according to the curve and thus deposit only very little fractions of their energy in the detector material.

through the tracking chambers. The muon spectrometer is also designed to trigger on these particles, utilising dedicated Trigger Chambers. The driving performance goal is a standalone transverse momentum resolution of approximately 10 % for 1 TeV tracks, which translates into a sagitta along the z axis of about $\chi = 500\,\mu\text{m}$, to be measured with a resolution of $\sigma_\chi \leq 50\,\mu\text{m}$. The sagitta χ is given by

$$\chi = R - R\cos\frac{\theta}{2}, \tag{2.4}$$

where R is the radius of the track curvature and θ is the angle enclosed by the outermost of three equidistant points along the track, as can be seen in Figure F-2.8.

To achieve high spatial tracking resolution, three layers (stations) of drift chambers (Precision Chambers) are employed both in the barrel and in the endcap region. In the barrel, being arranged in concentric cylinders, with the radii of the detector layers being at about 5 m, 7.5 m and 10 m, covering an η range of ± 1. Two of these layers are placed near the inner and outer field boundary, while the third is situated within the field volume. The muon momentum is then determined from the track sagitta, which is illustrated in Figure F-2.8. In this region, exclusively Monitored Drift Tube Chambers (MDTs) are used.

Due to the magnet cryostats in the endcap region, however, placing one station within the field is not possible. Hence it is necessary to rely on a point-angle measurement to determine the track momentum in this detector region (a point in the inner station and an angle in the combined middle-outer stations). The endcap layers are arranged in four concentric discs at 7 m, 10 m, 14 m, and 21-23 m from the detector origin, covering an η range of $1.0 < |\eta| < 2.7$. Here,

in addition to MDT chambers, Cathode Strip Chambers (CSCs) are used in the innermost layer of the inner station due to radiation hardness issues.

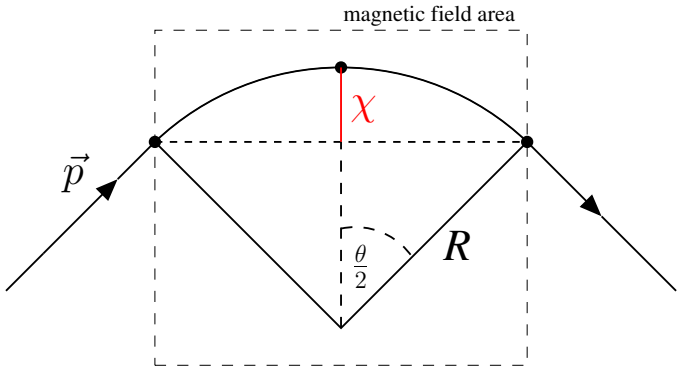

Figure F-2.8: Illustration of the track sagitta χ and its geometric relation to the bending radius R for a track of a particle with a given momentum $\vec{p}$ travelling through a homogeneous magnetic field, shown for the case of three equidistant track hits along the curvature.

The only exception from the continuous η coverage of the Muon Chambers was made at $|\eta| < 0.05$ in the R-ϕ plane to allow for cable and service outlets for the Inner Detector, the central solenoid and the calorimeters (central gap)

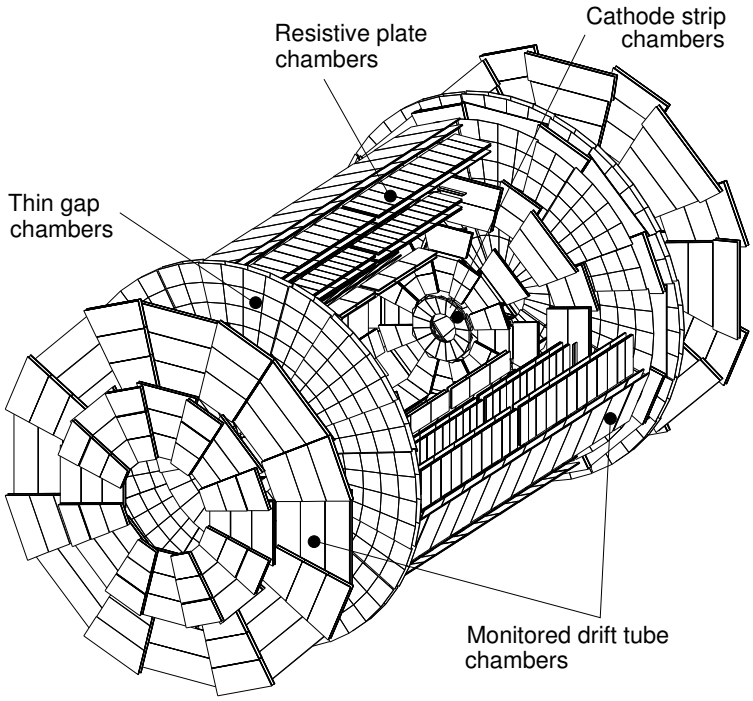

Figure F-2.9: The ATLAS Muon System. Shown are the Trigger Chambers (RPC, TGC) and the precision chambers (MDT, CSC).

Regardless of the high spatial resolutions, the timing resolution of the Precision Chambers as shown in Table T-2.3 is too low due to the drift time to ensure differentiation between muons from subsequent bunch crossings for the Trigger (where the scale of the required timing resolution is set by the bunch crossing interval of 25 ns). Thus it is necessary to employ additional

drift chambers with high timing resolution (at cost of spatial resolution), the Trigger Chambers. These provide a fast momentum estimate and are mostly used for the Trigger (since their spatial resolution is too low with respect to the Precision Chambers), which will be described in Chapter 2.4.

As for the Trigger Chambers, in the barrel region two out of three Resistive Plate Chambers (RPCs) are placed directly in front of and behind the central MDT, while the third is situated directly below or above (according to the mechanical constraints in the respective region) the outermost Precision Chamber. The RPCs are furthermore used to determine the second coordinate for the MDT chambers (in tube wire direction). In the endcaps, three layers of Thin Gap Chambers (TGCs) are located near the central endcap MDT layer for triggering.

A comparison of the different chamber technologies necessary to allow for both fast triggering and high precision measurements is shown in Table T-2.3.

	MDT	**CSC**	**RPC**	**TGC**
z/R **resolution [µm]**	35 (z)	40 (R)	10×10^3 (z)	(2-6) $\times 10^3$ (R)
# readout channels	339 000	30 700	359 000	318 000
# chambers	1 088	32	544	3 588
Area covered [m^2]	5 500	27	3 650	2 900
ϕ **resolution [mm]**	–	5	10	3-7
timing resolution [ns]	–	7	2	4

Table T-2.3: Comparison of Muon Chamber technologies.

2.3.4 Magnet System

Right outside the Inner Detector follows a Solenoid Magnet [29, 37] that bends the tracks of charged particles on their way through the Inner Detector, making it possible to measure the particle's momentum with high resolution. Its axial field strength is about 2 T (peak 2.6 T),

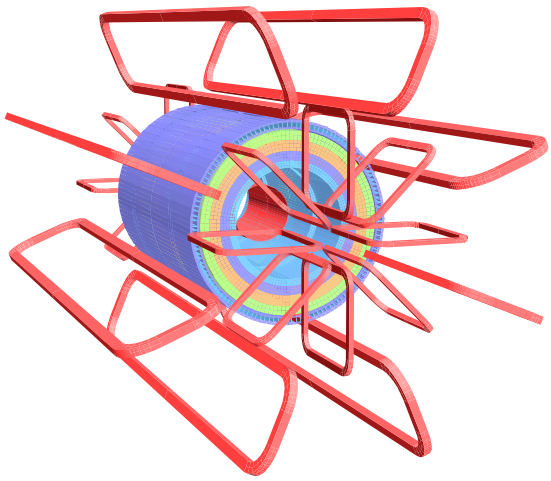

Figure F-2.10: Schematic view of the ATLAS Solenoidal (inner cylinder) and Toroidal Magnets (outer coils) [33].

while it weighs 4 t and contains about 10 km of low-temperature superconducting cables cooled down to 1.8 K with liquid helium during operation with a nominal current flow of 8 000 A.

In addition, a large Toroidal Magnet [38] consisting of eight superconducting coils in the barrel region and eight more at each of the forward regions extends throughout the Muon Chambers, providing a magnetic field strength of 4 T (peak 4.7 T). The whole toroid system contains over 70 km of superconducting cable, allowing for a design current of 20 000 A with a stored energy of above 1 GJ. To minimise multiple scattering of the muons, the toroid design incorporates an air core. Together with the Solenoid Magnet, its purpose is to bend the paths of muons in order to measure their transverse momentum (in combination with the tracking information from the Inner Detector).

2.4 The ATLAS Trigger System

As mentioned earlier, the design Luminosity of $10^{34}\,\mathrm{cm}^{-2}\mathrm{s}^{-1}$ together with the bunch crossing rate of 40 MHz and the amount of protons contained in each single bunch leads to a proton collision rate in the GHz regime, which corresponds to a certain amount of data (*data rate*). Being able to store only a fraction of this amount of data on storage medium ($\sim 300\,\mathrm{MBs}^{-1}$) and only a fraction of these collisions being useful for further studies, the ATLAS Trigger System [19,26,29] has to reduce the initial data rate by several orders of magnitude. Figure F-2.11 shows the total rates of several physics processes in comparison to the total interaction rate and the

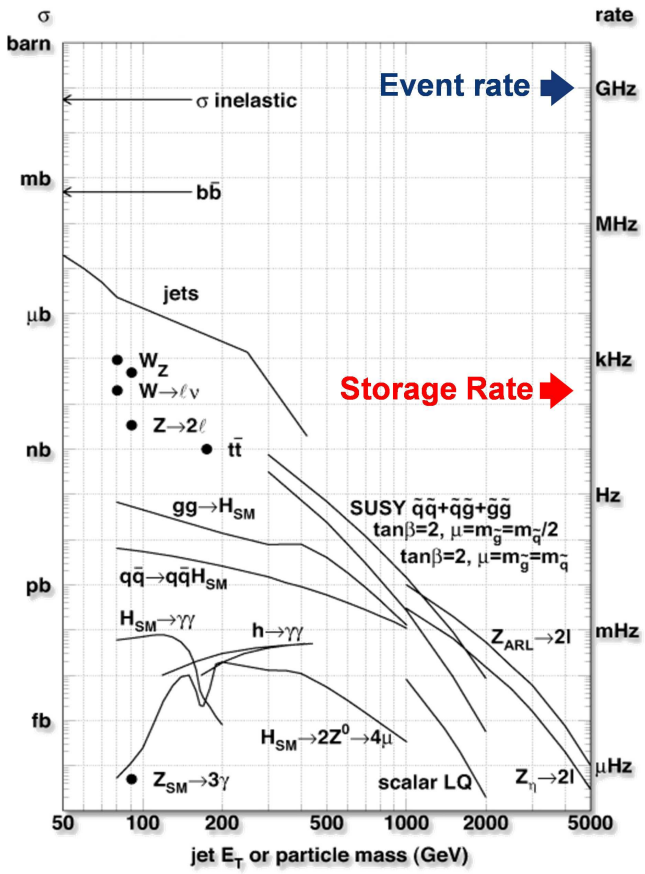

Figure F-2.11: Typical cross-sections and event rates for different production and decay channels (at the design Luminosity of $10^{34}\,\mathrm{cm}^{-2}\mathrm{s}^{-1}$) at the LHC.

maximum achievable storage writing rate. As can be seen, the frequency of the Standard Model Higgs production and decay to two photons ($H_{SM} \rightarrow \gamma\gamma$) for example lies in the mHz regime for the design Luminosity, constituting only a small fraction of the total amount of events per second, making the selection of this and other physics processes a crucial task.

In order to achieve such a reduction and to select only interesting physics events / processes, ATLAS uses a three-level Trigger System for online event selection (with the upper two levels being referred to as *High-Level Trigger*), while each Trigger level refines the decisions of its predecessor. An overview of the different Trigger levels and the global structure is shown in Figure F-2.12 and will be discussed in more detail in the following sections.

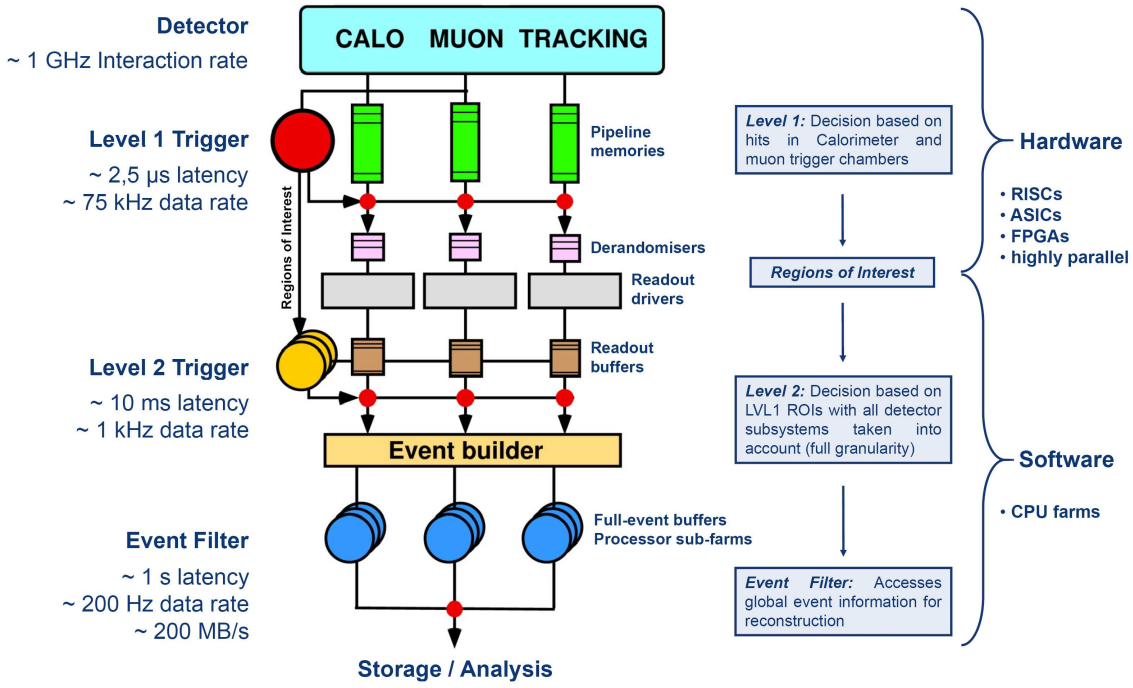

Figure F-2.12: Block diagram of the Trigger/DAQ system. On the left side the typical collision and the data equivalent at the different stages of triggering are shown, while in the middle section the different components of the Trigger system are show schematically. The right side of the graphic gives a short summary of the operations and the technologies used at the respective level.

2.4.1 Level 1 Trigger (LVL1)

The LVL1 Trigger is completely hardware-based, where highly specialised components are deployed, that is Field Programmable Gate Arrays (FPGAs), Application Specific Integrated Circuits (ASICs) and Reduced Instruction Set Computing (RISC). Since most of this hardware is integrated directly into the particular detector components in order to reduce material occurrence from cabling and additional readout electronics, the LVL1 Trigger System necessarily works highly parallelised.

Being based on the muon and calorimeter system only, the LVL1 Trigger [39] performs an initial selection on the basis of the hits in the Muon Trigger Chambers and calorimeters. In the Muon Chambers, low p_T and high p_T muons are identified by measuring the tracks in the Trigger Chambers (RPCs & TGCs) exclusively using coincidence windows for discrimination. Since low p_T muons show a smaller bending radius, thus allowing for detection by two layers in

close proximity to each other (Moreover, a track hit matching can be difficult if the in-plane hit distance in the coincidence layers is too large due to the curvature of the track), in the barrel region, low p_T muons are identified by the consecutive layers RPC1 and RPC2 (The number after the chamber type identifies the layer). In contrast, high p_T muons produce an almost straight track and therefore the coincidence layers used should be as separate as possible to allow for the measurement of the track radius. Hence, high p_T muons are measured by the combination of the outermost RPC1 and RPC3 hits in the barrel. In the endcaps, low p_T muons are identified by the TGC2 - TGC3 coincidence window, while TGC1 and TGC3 are used to identify high p_T tracks. This is shown in Figure F-2.13, where a quadrant layout of the Muon Trigger Chambers is shown.

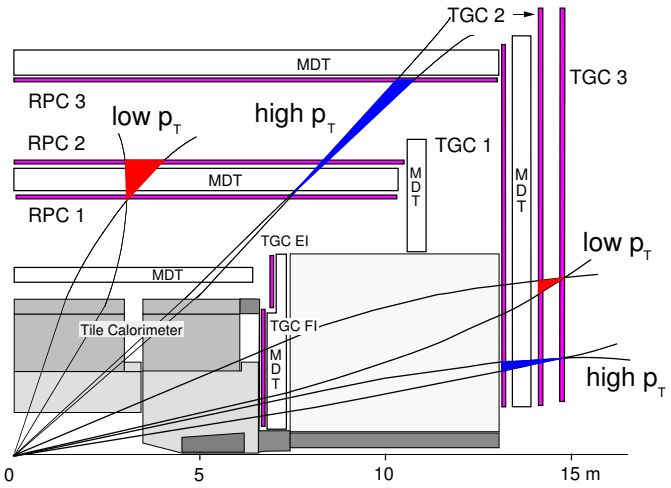

Figure F-2.13: Layout of the Muon Trigger Chambers [33]. Shown is a quarter cross-section in the bending plane with typical low p_T and high p_T muon tracks and the corresponding coincidence windows in the different layers for barrel (RPC1-3) and endcap (TGC1-3).

Classification of transverse momentum is then achieved by using large lookup tables of track hits only to find an estimate for the track momentum. Six exclusive p_T thresholds are predefined (6, 8, 10, 11, 20 and 40 GeV) and can be modified if necessary.

The calorimeter Trigger selection is based on low resolution information from all ATLAS calorimeters and is designed to identify high p_T electrons and photons, hadron jets and the total transverse energy alongside with large missing transverse energy $\not{E}_T$, where this is defined by the sum of all vectored energy depositions $\vec{E}_T$ in the transversal plane:

$$\vec{\not{E}}_T = -\sum \vec{E}_T. \tag{2.5}$$

This definition arises from the fact that the initial transverse momentum of the incoming protons is approx. zero and due to conservation of energy in the transverse plane, the total vector sum of final state transverse energies has to be zero as well. Furthermore, isolation requirements based on the calorimeter information are available for the calorimeter Trigger on this Trigger level.

Since the LVL1 Trigger works synchronised with data taking, the latency for a decision is about 2.5 µs, which is achieved despite the bunch crossing and data taking frequency of 40 MHz by making use of pipeline memories. The decision is then conducted while the information from the sensors is kept in the buffer memory for about 100 bunch crossings. At the end of the latency time, the readout data is rejected or accepted (after leaving the pipeline memory).

Only in the latter case the geometric information of the triggered object is forwarded to the next Trigger level as *Region Of Interest* (ROI), which includes spatial position (η and ϕ) and p_{T} estimates of the embedded objects (e, μ, τ, γ and jet candidates) as well as global energy information (scalar E_{T} and $\not{E}_T$) for further analysis. This way, the data rate is reduced to about 75 kHz (upgradeable to 100 kHz).

2.4.2 Level 2 Trigger (LVL2)

After a LVL1 accept, events are read out from the pipeline memories and stored in *Readout Buffers* (ROBs) until being processed by the LVL2 Trigger [40]. This Trigger level uses the ROIs from the previous level to further reduce the data rate to about 1 kHz. This is achieved by analysing each ROI in the detector system from which it originated, but additionally accessing the data from other detector subsystems in the ROI, including the Inner Detector tracking information, the full-granularity calorimeter hits and the Precision Chamber measurements from the Muon Spectrometer.

With an increased processing latency of 10 ms and the date rate already reduced in LVL1, the LVL2 Trigger allows for more complex algorithms being applied to the Trigger objects and the information from the respective ROIs. As a part of the High-Level Trigger, the LVL2 stage is completely software-based and runs on dedicated computing farms. To be more specific, the Trigger decision is then performed by an event-driven sequential selection procedure upon the detector data. Despite the LVL2 Trigger providing more time to conduct the Trigger decision than the LVL1 stage, the selection algorithms still have to be kept simple and efficient. Hence, the sequence of the different algorithms / requirements is determined by their complexity, simple (with respect to CPU time and memory) ones are executed first, while each algorithm uses the result of its predecessor to conduct analysis (*seeded reconstruction*).

2.4.3 Event Filter (EF)

In the final execution level of the Trigger which is software based and runs on CPU farms, the global event is collected from the ROBs. Thus, the Event Filter accesses the complete event information and all detector subsystems using full granularity. An event reconstruction at Trigger level is possible by using similar algorithms as it is the case for Offline reconstruction, accessing calibration and alignment information from databases.

In addition to the reconstruction of the event as a whole, the Event Filter performs extended tasks that are not possible at earlier Trigger levels, such as vertex reconstruction, final track fitting and algorithms requiring larger ROIs than available at LVL2 (e.g. the calculation of global $\not{E}_T$).

The latency of the Event Filter is of the order of seconds, after which events passing this final Trigger level are stored for further analysis or, in some cases, may be redirected to special storage elements as well (if needed for calibration or alignment exclusively).

2.4.4 Trigger Implementation

The information used to conduct the LVL1 decision is given in terms of multiplicities of *Trigger Elements* resembling candidates for physics objects (like electrons, muons, jets,...) detected in the calorimeters or Muon Trigger Chambers which have sufficiently high p_{T}. These are sent to the Central Trigger Processor (CTP) together with threshold information on global energy sums. The delivered multiplicities are discriminated against multiplicity requirements or conditions,

leading to truth values 'yes' or 'no' for each condition within so-called *Trigger Menus*. Examples for LVL1 Trigger Menus would be:

EM25i: Electromagnetic, $p_{\mathrm{T}} > 25\,\mathrm{GeV}$, isolated.
MU20: Muon, $p_{\mathrm{T}} > 20\,\mathrm{GeV}$.

The condition truth values are then logically combined to complex *Trigger Items*, which represent the signatures to be triggered by LVL1, e.g.

'at least one muon with $p_{\mathrm{T}} > 25\,\mathrm{GeV}$ **AND** $\not{E}_T > 200\,\mathrm{GeV}$'.

The final LVL1 event decision is derived from the truth values of the defined Trigger Items by applying a logical 'OR'. If the event is accepted, the ROIs for all Trigger Items and the contained Trigger Elements above the defined thresholds are delivered to the High-Level Trigger, where they are used as *seed* for further algorithms.

The step-by-step execution of Trigger algorithms as it is done on LVL2 and EF level is called a *Trigger Chain*, consisting of different intermediate *Trigger Signatures* (cf. Trigger Items on LVL1), where the successive Trigger algorithms keep refining the intermediate Trigger Signatures in the course of a Trigger Chain. These signatures are again defined by Trigger Menus, e.g.

e30i: Electron, $p_{\mathrm{T}} > 30\,\mathrm{GeV}$, isolated.
mu20i: Muon, $p_{\mathrm{T}} > 20\,\mathrm{GeV}$, isolated.

An example for a particular dimuon Trigger Chain, corresponding to the latter Trigger Menu is shown in Figure F-2.14. In each step of the Chain, two identical Trigger Elements are combined to a Trigger Signature. Finally, if all requirements were passed for both Elements, the final dimuon Trigger Signature is delivered.

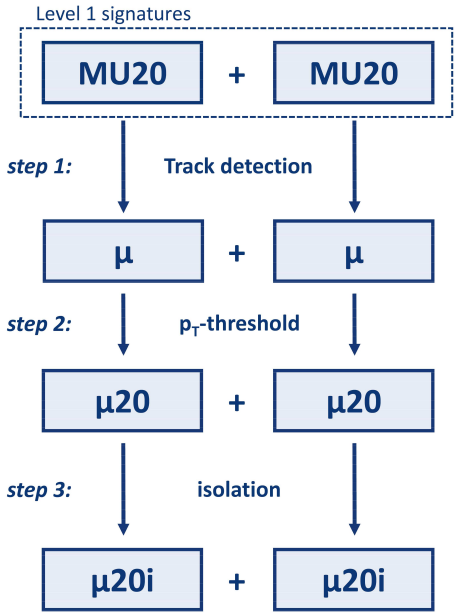

Figure F-2.14: An example of a Trigger Chain (Dimuon, isolated, high p_{T}). In each step of the Trigger Chain, the requirements are applied to both Trigger Elements (with the "+" indicating a logical *OR*) and combined to an intermediate Trigger Signature if accepted, before finally yielding the resulting mu20i Trigger Signature.

As an additional requirement on the High-Level Trigger, parallel execution of different Trigger Chains without interference must be ensured in so called independent *slices* (e.g. *electron slice* and *muon slice*) to ensure transparency and scalability of the Trigger System.

3 Analysis

This Chapter deals with the development and verification of methods to measure Trigger Efficiencies from data without having to rely on Monte Carlo simulations, in particular the Trigger simulation, for the efficiency measurement itself.

3.1 Analysis Overview

With the primary goal to reduce data rates, the ATLAS Trigger System has to select potentially interesting events for further storage and analysis from a large amount of information. To allow for this task to be performed, the Trigger is required to be

- Simple,
- Inclusive,
- Robust,
- Efficient,
- Redundant[1].

Hence, extensive knowledge about the performance parameters of the Trigger and in particular the respective uncertainties of these parameters is crucial, especially when considering that every measurement at ATLAS is affected by the Trigger and its performance, including

- Discoveries,
- Cross-section measurements,
- Measurement of particle properties (can only be ensured if all according events are triggered correctly (cf. background considerations)).

In general, Trigger performance can be characterised in terms of rejection rate (how many events/objects pass the Trigger) and efficiency (what percentage of interesting events gets accepted), where the resulting performance is given by the combination of both aspects[2]

$$\text{Performance} = \text{Rejection} \times \text{Efficiency}$$

This analysis focuses on the development of a method to determine the Trigger efficiency from data, where only the Muon Trigger System was taken into account. Thus, *performance* in this context is equal to the *efficiency* of the Muon Trigger. In order to conceive the Trigger efficiency and the corresponding statistical and systematic uncertainties with respect to the upcoming ATLAS data, it is desirable to have a method at hand that does not rely on Monte Carlo simulations to determine Trigger efficiencies. Furthermore, it should be possible to take

[1] This is only necessary for the efficiency measurement.
[2] This definition only makes sense provided the performance and both factors can be measured from data.

into account arbitrary background normalisations for efficiency measurement. The developed method can then be applied to real data in order to determine the Trigger performance and the obtained parametrised efficiencies can then be used on any physics process to determine the Trigger efficiency for that process without actually having to use the Trigger information of the sample.

Under the aspect of efficiency, two kinds of *errors* that can affect Trigger performance have to be taken into account:

- Type I error, that is rejecting events that should have been accepted (*(in)efficiencies*).
- Type II error, that is accepting events that should have been rejected (*fake efficiencies*).

The first part of this thesis focuses on the determination of the Trigger efficiency from two different simulated processes to examine the influence of different process kinematics on several parameterisations of the Trigger efficiency. This will be done by simply counting the objects in the simulated samples on the different Trigger levels and relating them to each other (*Monte Carlo counting method*). This is the "true efficiency" of the Trigger. Furthermore, a second method to determine the Trigger efficiency, the actual data method, will be introduced and the results will be compared to the counting method as a cross-check.

In the second part, the influence of fake efficiencies due to detector effects will be analysed and methods to quantify these effects from data will be developed and verified. The impurity of the data sample for the signal efficiency measurement can then be determined and the data method can be corrected for the Trigger (fake) efficiency of this contribution.

3.1.1 Monte Carlo Simulation

In order to analyse and verify the data methods to be discussed in the following, several physics processes were simulated, including multiple background sources. In addition, a single muon sample, flat in p_{T}, η and ϕ was produced to allow for a kinematically independent Trigger analysis.

All samples were restricted to a pseudorapidity region of $|\eta| < 2.8$ considering the coverage of the Muon Chambers to be $|\eta| < 2.7$ to enhance statistics in the observable region. A more detailed list of the generated samples, including the individual parameters of generation can be found in the Appendix.

For event generation, simulation, digitisation and reconstruction, the Athena Framework (version 12.0.6) [41] was used. Athena is a control framework and is a concrete implementation of an underlying architecture called Gaudi [42], a kernel of software common to both LHCb and ATLAS, while Athena is the sum of this kernel plus ATLAS-specific extensions. The framework can be used to perform the following tasks:

- Monte Carlo simulation via interfaces to several generators, such as Pythia [43], MC@NLO [44, 45], HepMC [46] and more.
- Simulation of detector and Trigger response by utilising Geant [47] (*GEometry ANd Tracking*), a toolkit for the simulation of the passage of particles through matter.
- Digitisation of the GEANT simulated detector hits.
- Reconstruction of both simulated and real data.
- Analysis of reconstructed events.

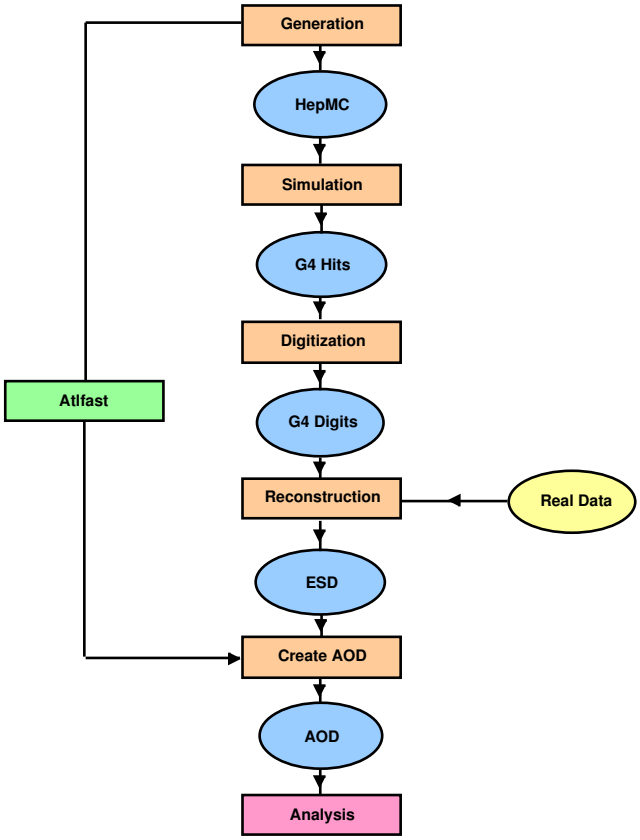

Figure F-3.1: Schematic representation of the full ATHENA chain.

The ATHENA processing structure can be seen in Figure F-3.1. When using simulations, the first step in the chain is the generation of the Monte Carlo four-vectors of the simulated process. The resulting information is then fed into the GEANT toolkit to simulate material interactions with the detector. This interaction information is then further processed in the digitisation step to mimic the detector and Trigger response for the simulated interactions with the detector. When compared to the case of taking real data, the output from the digitisation procedure resembles the detector output from real data, making the following steps identical for simulation and data.

The raw digitised detector response is used to reconstruct the different objects (Physics, Trigger, MC, ...) within each event which can then be stored in files together with several event variables, where different data types with different levels of abstraction and amount of data contained are available. ESD (*Event Summary Data*) files aside from the reconstructed events contain sufficient information to re-run parts of the reconstruction, with the object connections (like mother – daughter vertex relations) still available. Optionally, the amount of available information and therefore the file size can be further reduced to AOD files (*Analysis Object Data*), containing a reduced size of physics quantities from the reconstruction.

It is possible to perform a fast simulation of the whole process by utilising ATLFAST [48], a toolkit to simulate the detector response by introducing simple smearing algorithms to mimic the interactions in the detector, in particular resolution effects.

For this thesis, PYTHIA 6.403 and PARTICLEGENERATOR were used for generation[3], while GEANT 4 was used for full detector simulation and digitisation (detector geometry ATLAS-CSC-01-02-00 [49]), both tools via their respective interfaces to ATHENA. The results from ATHENA offline reconstruction was stored in the AOD format.

Since the ATHENA simulation/reconstruction does not conserve the information that links objects from the Monte Carlo generator level to offline reconstruction objects (and neither to Trigger objects), it is necessary to perform a matching procedure to identify corresponding objects and their affiliation at the different Trigger levels and at offline reconstruction level for further analysis. In this case, this is of particular importance for the muons since the efficiency measurements to be conducted relate the objects on the different Trigger levels and offline level to each other.

This is achieved by a geometric matching in ΔR, where this is defined for example for the matching of muons from offline reconstruction level to the corresponding Monte Carlo generated particle as

$$\begin{aligned} \Delta R &= \sqrt{(\Delta\eta)^2 + (\Delta\phi)^2} \\ &= \sqrt{(\eta_{\mathrm{MC}} - \eta_{\mathrm{offline}})^2 + (\phi_{\mathrm{MC}} - \phi_{\mathrm{offline}})^2} \end{aligned} \tag{3.1}$$

and for the different Trigger levels, accordingly.

A positive match of the muons is denoted by a ΔR below a predefined threshold. If that is the case, the two objects are then identified with each other, indicating a high probability of representing the same physics muon. If there are multiple possibilities or combinations of objects that may be matched, the optimum combination is determined by calculating the matching values for all possible object relations as a matrix ΔR_{ij}, where i and j denote the ith and jth muon on the different levels, respectively. The best global matching for that event is then defined by the combination with the lowest sum of matching values, of course without the possibility of double matching. This algorithm is independent of the order of the muons in the sample.

To further optimise the matching process, a preselection is performed, discarding all combinations with values exceeding a certain, very loose ΔR requirement to reduce matrix permutations.

Since possible matching inefficiencies introduce a bias and therefore affect Trigger efficiencies that are determined from the simulated samples, quantification of systematic uncertainties may become more difficult. Since this will not be an issue when applying the developed methods to real data and Monte Carlo simulations are performed only for verification and testing purposes, these effects are not taken into account for this analysis.

After the procedure is completed, the matched muons and all other object and event information necessary for further analysis are stored in a tree-like tuple structure for further analysis, which is performed with ROOT [50] (version 5.14), an object oriented data analysis framework based on C++.

3.1.2 The Drell-Yan Process

In order to determine the Trigger efficiency with a data method, a particular process within the sample has to be selected. In this case, the Drell-Yan [51] production of two muons was chosen. The Drell-Yan interaction describes the annihilation of a quark-antiquark pair and the production of a dilepton pair via the exchange of an intermediate $W^{\pm}$ or Z^0 boson or a virtual photon, in this case $q\overline{q} \rightarrow Z^0/\gamma^* \rightarrow l^+l^-$. The leading order Feynman Graph of the dimuon part of this process is shown in Figure F-3.2.

[3] Monte Carlo generation was performed in leading order

The differential cross-section for the Drell-Yan reaction can be obtained by squaring the matrix element, integrating over the azimuthal angle, averaging over the polarisation of the incoming particles and summing over the spin and polarisation of the final state particles, yielding for a given centre-of-mass energy s of the partons:

$$\begin{aligned}\frac{d\sigma}{d\cos\theta} = C\frac{\pi\alpha^2}{2s}\Big\{ & Q_l^2 Q_q^2 (1+\cos^2\theta) \\ & + Q_l Q_q \Re\left[\chi(s)\right]\left[2g_V^q g_V^l (1+\cos^2\theta) + 4g_A^q g_A^l \cos\theta\right] \\ & + |\chi(s)|^2\left[(g_V^{q2}+g_A^{q2})(g_V^{l2}+g_A^{l2})(1+\cos^2\theta) + 8g_V^q g_A^q g_V^l g_A^l \cos\theta\right]\Big\},\end{aligned} \tag{3.2}$$

where C is the colour factor, θ the emission angle of the (anti-)lepton with respect to the (anti-)quark in the dilepton rest frame, Q_l and Q_q the charges of the leptons and quarks, respectively and g_V^f and g_A^f the vector and axial-vector couplings of the fermions to the Z^0, where $f = \{l, q, l2, q2\}$. In addition, it is

$$\chi(s) = \frac{1}{\cos^2\theta_W \sin^2\theta_W} \cdot \frac{s}{s - M_\mathrm{Z}^2 + i\Gamma_\mathrm{Z} M_\mathrm{Z}}, \tag{3.3}$$

with the electroweak mixing angle θ_W and the Z^0 pole mass M_Z and the corresponding width Γ_Z.

The first and the third term in Equation 3.2 correspond to the pure Z^0 and γ^* exchange, respectively, while the second term represents the Z^0/γ^* interference. This mediation is dominated by virtual photons for low values of dilepton invariant mass, and by the Z^0 contribution at invariant masses near the Z^0 pole mass.

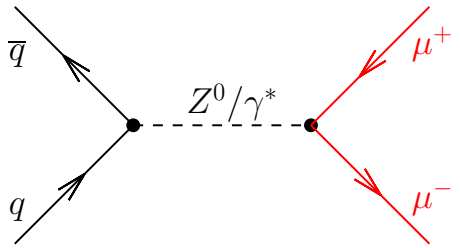

Figure F-3.2: $q\overline{q} \to \mathrm{Z}^0/\gamma^* \to \mu^+\mu^-$ leading order Feynman Graph.

The simulated $q\overline{q} \to \mathrm{Z}^0/\gamma^* \to \mu^+\mu^-$ kinematics (abbreviated $\mathrm{Z}^0/\gamma^* \to \mu\mu$ in the following), that is the generated (four-vector level) and offline reconstruction distributions in p_T, η and ϕ for the simulated sample, are shown in Figure F-3.3 for comparison.

The p_T distribution shape indicates the γ^* and Z^0 fractions of the Drell-Yan process, respectively. Since a photon is a massless particle, it must always be produced off-shell in this process in order to create a dilepton pair, with a maximum probability of having mass equal zero. Hence, the photon part of the distribution diverges for low muon transverse momenta, as expected. A second peak can be identified at about half the Z^0 pole mass from the Z^0 boson contribution to the dimuon production. In addition, the generator requirement at 5 GeV for the muon p_T can easily be recognised on both generator and offline level, smeared in the latter case by resolution effects. Furthermore, a second part of the distribution can be found on generator level below the introduced constraint, which is due to the fact that the p_T constraint was only applied to the two muons from the Z^0/γ^* decay, while other muons in the event (e.g. from gluon radiation) are not affected by this cut. This effect is not visible on offline level, since only the two highest p_T muons were taken into account here in order to allow for the examination of the muons from the $\mathrm{Z}^0/\gamma^* \to \mu\mu$ decay only.

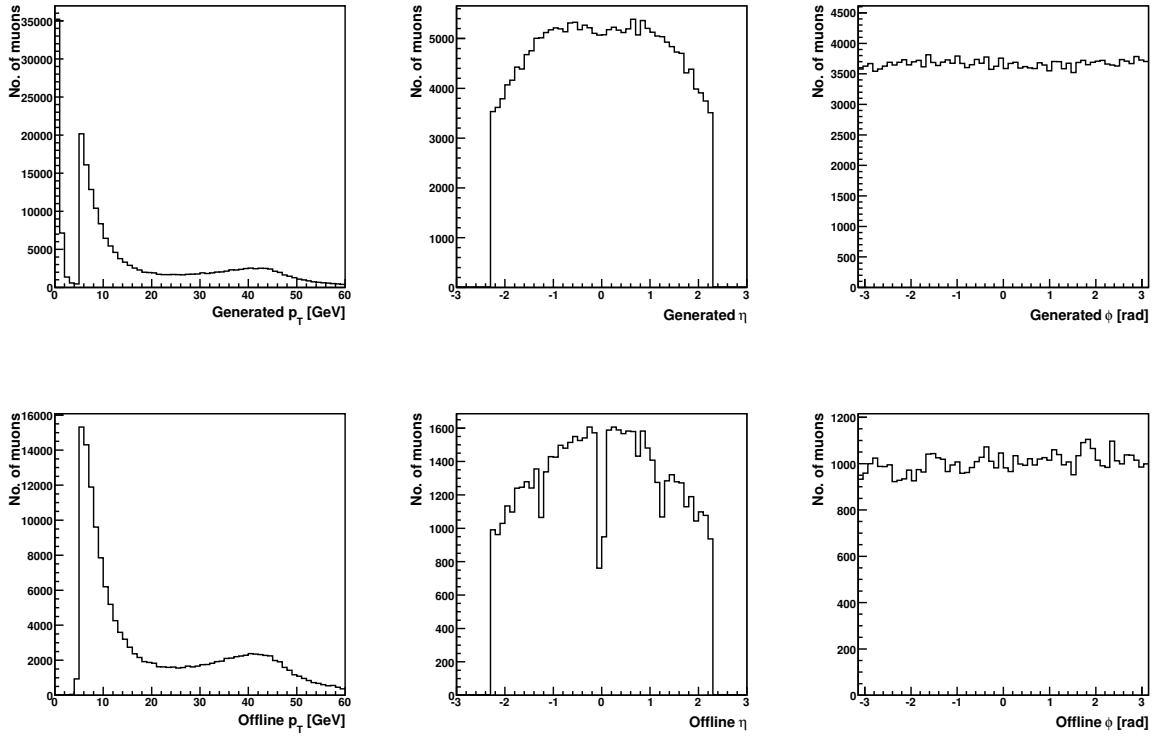

Figure F-3.3: $Z^0/\gamma^* \to \mu\mu$ kinematics (generated (top row) and offline (bottom row) variables). Left: Muon transversal momentum with 5 GeV constraint applied on generator/four-vector level to Z^0 decay products; Middle: Muon pseudorapidity η in the centre-of-mass system; Right: Muon azimuthal angle ϕ. As can be seen, the reconstructed kinematics are different from the generated four-vector distributions due to detector/resolution effects.

The η distributions drop noticeably towards higher rapidities indicating that most of the observed muons emerge into the barrel region of the detector due to the generator p_T constraint which introduces an implicit bias in rapidity by removing muons which possess a higher longitudinal momentum component boosting them in forward direction. Moreover, gaps in the acceptance of the detector can be seen at offline level at $\eta \approx 0$ (central gap), where several supply lines and the corresponding outlets for the Inner Detector and the calorimeters can be found over the full radius of ATLAS, and at $|\eta| \approx 1$, in the transition area of barrel and endcap Muon Chambers.

The ϕ distribution is mostly flat for generated and reconstructed muons as expected from the fact that there is no initial transverse momentum carried by the incoming proton beams and thus no preferred polar angle for the final state particles in the event. Furthermore, the detector design is almost cylindrically symmetric, except for two dips in the lower detector area (at $\phi \approx -1$ and $\phi \approx -2$) on offline level. These are caused by the two ATLAS feet, affecting almost the whole barrel region at those polar angles and therefore having a visible effect on the integrated ϕ distribution.

Figure F-3.4 shows the invariant mass of the two reconstructed muons side by side with the corresponding $\Delta\phi$ distribution and the $\cos(\theta)$ distribution for the two muons, where θ is the muon polar angle in the Z^0 rest frame.

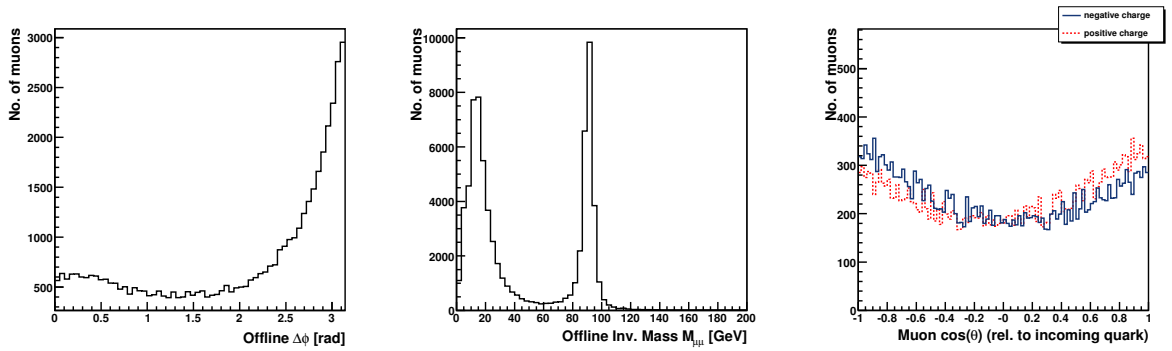

Figure F-3.4: $Z^0/\gamma^* \to \mu\mu$ kinematics. Left: offline dimuon emission angle; Middle: offline dimuon invariant mass; Right: Muon $\cos\theta$ distribution (generator level), relative to the (anti-)quark, where the distribution was obtained from the Z^0 contribution only.

As can be seen, muons emerging from the γ^* or Z^0 boson decay are mostly created back-to-back due to conservation of energy and momentum. Nevertheless, this would be only precisely correct if the photon or Z^0 boson is produced at rest. Since it can carry a momentum itself as well, the dilepton system may be boosted, thus changing the incident angle between the constituents in the centre-of-mass frame. The second peak is due to the low p_T photon fraction in the sample, causing the produced leptons to be strongly boosted and thus being preferably collinear.

The invariant mass distribution again shows the dual structure of the photon and Z^0 boson fractions of the Drell-Yan process, with the Z^0 peak clearly visible at about 91 GeV, obeying a Breit-Wigner distribution in this range as expected ($M_Z = 91.1876 \pm 0.0021$ GeV [13]). The photon contribution, almost vanishing at the Z^0 pole, shows the expected s^{-1} dependency.

Finally, the $\cos(\theta)$ distribution shows a forward-backward asymmetry caused by the weak (and thus maximum parity violating) gauge boson contribution to the interaction. The presence of both vector and axial-vector couplings of the quarks and leptons to the Z^0 boson gives rise to an asymmetry in the polar emission angle θ of the muon in the dimuon rest frame.

3.2 Trigger Efficiency Studies

When considering a given set of n objects to be triggered, the Trigger efficiency ε is defined as fraction k out of n that pass the Trigger:

$$\varepsilon = \frac{k}{n}, \tag{3.4}$$

where the geometric acceptance of the Trigger System has to be taken into account for the denominator (only objects that would be detectable by the Trigger should contribute to the efficiency). For this analysis, this is in particular of importance with respect to the LVL1 Trigger, where the geometric acceptance of the Muon Trigger Chambers is 94.67 % [19] for $\eta < 2.4$. Thus, this acceptance was corrected for in the following when examining LVL1 efficiencies. Since both offline reconstruction and High-Level Trigger use the Precision Chambers for the p_T estimate and all efficiencies were determined with respect to the offline values, the geometric acceptance for LVL2 and EF is assumed to be identical.

Trigger efficiencies are typically characterised as function of transverse momentum with respect to a given Trigger threshold for p_{T} (Only the 20 GeV threshold for the Muon Trigger is taken into account in the following, if not stated otherwise). In this context, an ideal Trigger response would resemble a Heaviside function. That is, below the Trigger threshold, no object would pass the Trigger, while every object above would be accepted, as shown in Figure F-3.5.

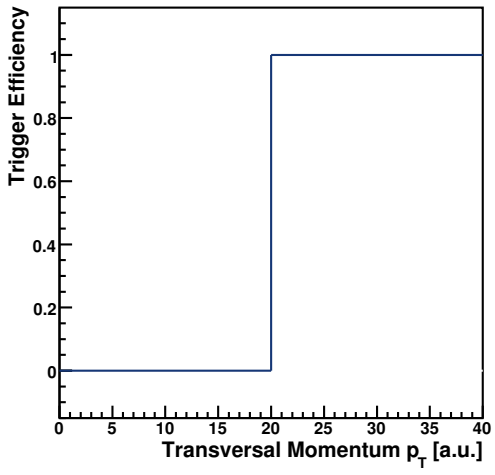

Figure F-3.5: Ideal Trigger response resembling a Heaviside function discriminating between objects below or above the given threshold without any inefficiencies or resolution effects.

In reality, the measured transverse momentum is smeared with respect to the p_{T} of the physics muon (or the generated four-vector p_{T} from Monte Carlo simulations, respectively) due to finite resolution of the measurement. With respect to the shape of the Trigger efficiency curve in p_{T} this would lead to a Gaussian Error Function under the assumption of Gaussian distributed resolution effects by convoluting Heaviside function with a Gaussian resolution function, as it can be seen in Figure F-3.6. This leads to a *turn-on* region in the p_{T} dependent efficiency instead of the Heaviside response, which can be defined by the efficiency range from 5 % to 95 % on the p_{T} axis, while the p_{T} region above the turn-on is defined as *saturation range*, which should quickly approach a constant efficiency for a good Trigger.

In addition, high p_{T} muon tracks will show a lower relative momentum resolution than low p_{T} tracks due to the fact that tracks of muons with high transverse momentum are basically straight, making it difficult to determine the track shape properties from the resulting large bending radius.

Since the actual measured quantity in the transverse momentum estimation process is the track sagitta χ, being inversely proportional to the transverse momentum p_{T} of the track, p_{T}^{-1} is Gaussian distributed for high statistics.

This is shown in Figure F-3.7, where the normalised relative momentum measurement resolutions σ_{rel} with respect to the Monte Carlo value,

$$\sigma_{\mathrm{rel}} = \frac{\frac{1}{p_{\mathrm{T}}^{\mathrm{MC}}} - \frac{1}{p_{\mathrm{T}}^{\mathrm{Measure}}}}{\frac{1}{p_{\mathrm{T}}^{\mathrm{MC}}}} = 1 - \frac{p_{\mathrm{T}}^{\mathrm{MC}}}{p_{\mathrm{T}}^{\mathrm{Measure}}} \tag{3.5}$$

are shown for offline reconstruction, LVL2 Trigger and EF, in each case divided into two p_{T} bins below and above 20 GeV (generator level) to distinguish between low an high p_{T} muons. The

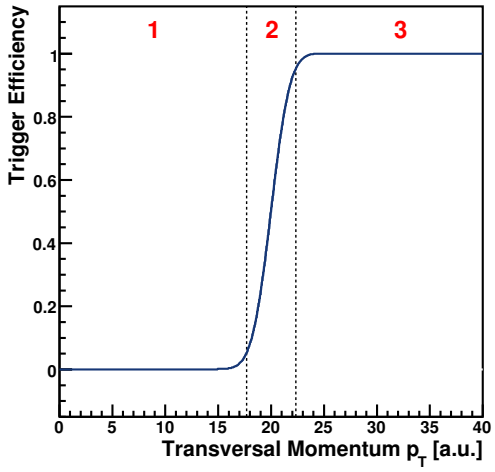

Figure F-3.6: Trigger turn-on curve resembling a Gaussian Error Function (under the assumption of Gaussian smearing of the p_{T} measurement. Region 1: Region of minimum efficiency (should quickly approach zero for decreasing p_{T} with respect to the Trigger threshold); Region 2: Turnon region, defined by the p_{T} axis covered by the efficiency range from 5 % to 95 %; Region 3: Saturation range.

LVL1 Trigger is not included, since there is no actual p_{T} value measured at that Trigger level. Only the highest passed Trigger threshold, determined from the lookup tables, is stored in the Region of Interest and delivered to the High-Level Trigger.

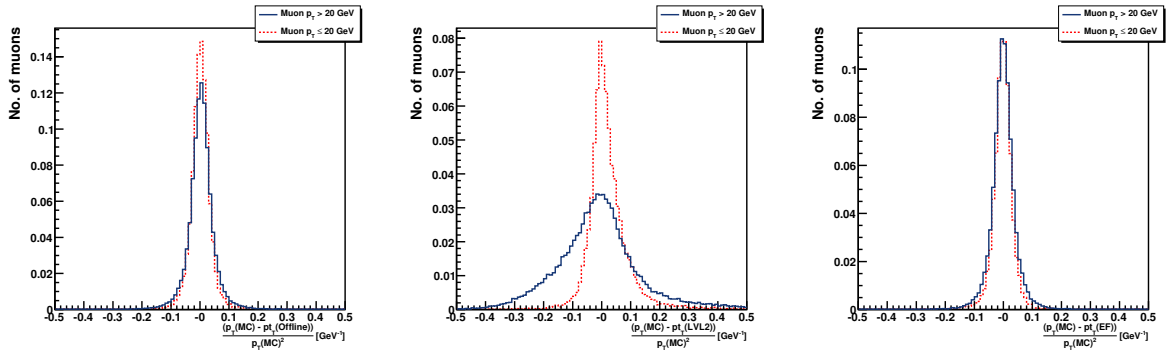

Figure F-3.7: Muon transverse momentum resolution for offline reconstruction (left), LVL2 Trigger (middle) and EF (right) for two different p_{T} bins (below (dashed line) and above (solid line) 20 GeV). The LVL2 transverse momentum measurement is obviously biased towards higher p_{T} values than generated for muons with $p_{\mathrm{T}} \leq 20\,\mathrm{GeV}$ as can be seen in the middle plot.

As expected, the relative resolution depends on p_{T}, being better for muons with lower transverse momentum, which can be seen at all analysed Trigger levels and offline reconstruction as well. Table T-3.1 shows a summary of the obtained resolutions, assuming a Gaussian resolution and thus performing a Gaussian fit in an appropriate range for each level and p_{T} bin.

The LVL2 transverse momentum estimate shows an unexpected behaviour, typically being higher than the generated transverse momentum for low p_{T} muons and vice versa for high p_{T} muons. In addition, the widths of the distribution for muons with transverse momentum

Level	Rel. resolution	
	$p_{\mathrm{T}} > 20\,\mathrm{GeV}$	$p_{\mathrm{T}} \leq 20\,\mathrm{GeV}$
offline	$(3.00 \pm 0.02)\,\%$	$(2.56 \pm 0.02)\,\%$
LVL2	$(9.21 \pm 0.06)\,\%$	$(3.23 \pm 0.05)\,\%$
EF	$(3.10 \pm 0.01)\,\%$	$(2.50 \pm 0.03)\,\%$

Table T-3.1: Transverse momentum resolutions for offline reconstruction, LVL2 Trigger and EF with respect to Monte Carlo generator level for two different p_{T} bins.

above and below 20 GeV differ very strongly, especially when being compared to offline/EF level and taking into account that the LVL2 p_{T} estimate utilises the Precision Chambers as well.

This effect is due to an anomaly in the LVL2 Trigger realisation in the ATHENA FRAMEWORK. While the offline reconstruction and EF p_{T} estimates resemble the generated distribution within resolution effects, the LVL2 p_{T} distribution is biased towards higher transverse momenta. This is shown in Figure F-3.8, where the three p_{T} distributions from offline reconstruction, LVL2

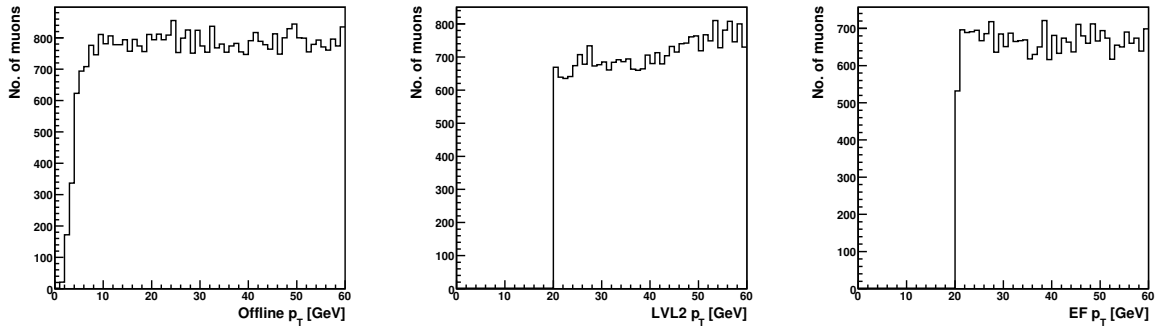

Figure F-3.8: Single muon transverse momentum distributions for offline, LVL2 and EF. The LVL2 distribution is not flat as expected from the single muon sample and as it is the case for offline reconstruction and EF.

Trigger and EF for the single muon sample (which is generated to be flat in p_{T}) are compared before any offline selection criteria were applied to the samples.

As can be seen, the transverse momentum is systematically overestimated. This effect is not yet understood to its full extend, but is most probably due to the LVL2 Trigger implementation in the used ATHENA version not being final and only providing information about the endcap region in combination with the hits from the tracking system. Porting to a more recent version should solve this problem, since it is obviously a computational issue, while this was not performed in the context of this thesis. Due to several changes in the structure of the subsequent version, adapting and more importantly verifying the code would be very time-consuming. Furthermore, waiting for the upcoming release of a newer version could further improve the benefits of this effort.

When considering a p_{T} dependent resolution of the measurement, a more realistic Trigger turn-on curve resembles a Gaussian Error Function with p_{T} dependent width of the Gaussian resolution distribution, where the resolution is evidently better at the lower end of the turn-on curve than towards the saturation range. This is shown in Figure F-3.9.

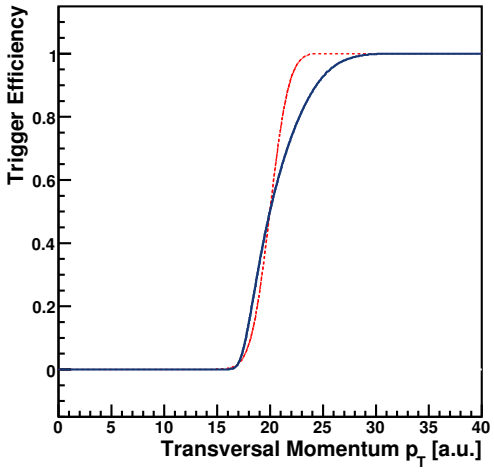

Figure F-3.9: Realistic Trigger response curve. Since the measurement resolution of muon transversal momentum is a function of p_{T} itself, the (approximately) Gaussian resolution is not constant over the whole range, thus leading to a broadening of the Trigger turn-on towards the saturation range. The dashed red curve shows the Gaussian Error Function as in Figure F-3.6 for direct comparison.

In order to study the Trigger response with respect to single objects (here: muons) and to avoid any kinematic bias to be introduced, a Monte Carlo sample of single muons is examined first. The generated sample contains one isolated muon per event and was produced with Monte Carlo generator parameters for the sample to be flat in p_{T}, η and ϕ. The resulting kinematic distributions on four-vector and offline reconstruction level can be seen in Figure F-3.10.

The offline p_{T} distribution is almost flat, where the lowest p_{T} muons are not being reconstructed at all due to the muons being stopped in the detector material or not being detected in the Precision Chambers due to a track bending radius that is too small to be recognised in the muon spectrometer. Since this analysis focuses on the 20 GeV threshold, this is not relevant, but has to be kept in mind when considering low p_{T} thresholds in the following. The generated p_{T} spectrum shows a minimum transverse momentum that can be generated below 1 GeV, while the offline reconstruction distribution shows a minimum accessible p_{T} of a few GeV with a steep rise and the measured distribution being almost flat from a transverse momentum of 8 GeV onwards.

Furthermore, the spatial distributions show the ATLAS typical acceptance gaps at the central barrel and the transition region, as seen in the $\mathrm{Z}^0/\gamma^* \rightarrow \mu\mu$ sample. Compared to this, the pseudorapidity distribution maintains almost constant towards higher rapidities, since for the single muons there is basically no bias in transverse momentum for the analysed kinematic region, since only a high p_{T} generator requirement at 100 GeV was introduced.

To determine the actual Trigger efficiency for an isolated muon (as the muons from the $\mathrm{Z}^0/\gamma^* \rightarrow \mu\mu$ sample to be examined are expected to be isolated as well, this criterion is very important to allow for a comparison) from the single muon sample, a Monte Carlo counting method is applied to the events. This can be done by counting the muons at offline reconstruction level $\mathrm{N}_{\mu}^{\mathrm{offline}}$ and by then determining the fraction of muons that fired the Trigger, $\mathrm{N}_{\mu}^{\mathrm{Trigger}}$. The Trigger efficiency with respect to offline reconstruction is in this case given by:

$$\varepsilon_{\mathrm{MC}}^{\mathrm{Trigger}} = \frac{\mathrm{N}_{\mu}^{\mathrm{offline\,\&\,Trigger}}}{\mathrm{N}_{\mu}^{\mathrm{offline}}} \tag{3.6}$$

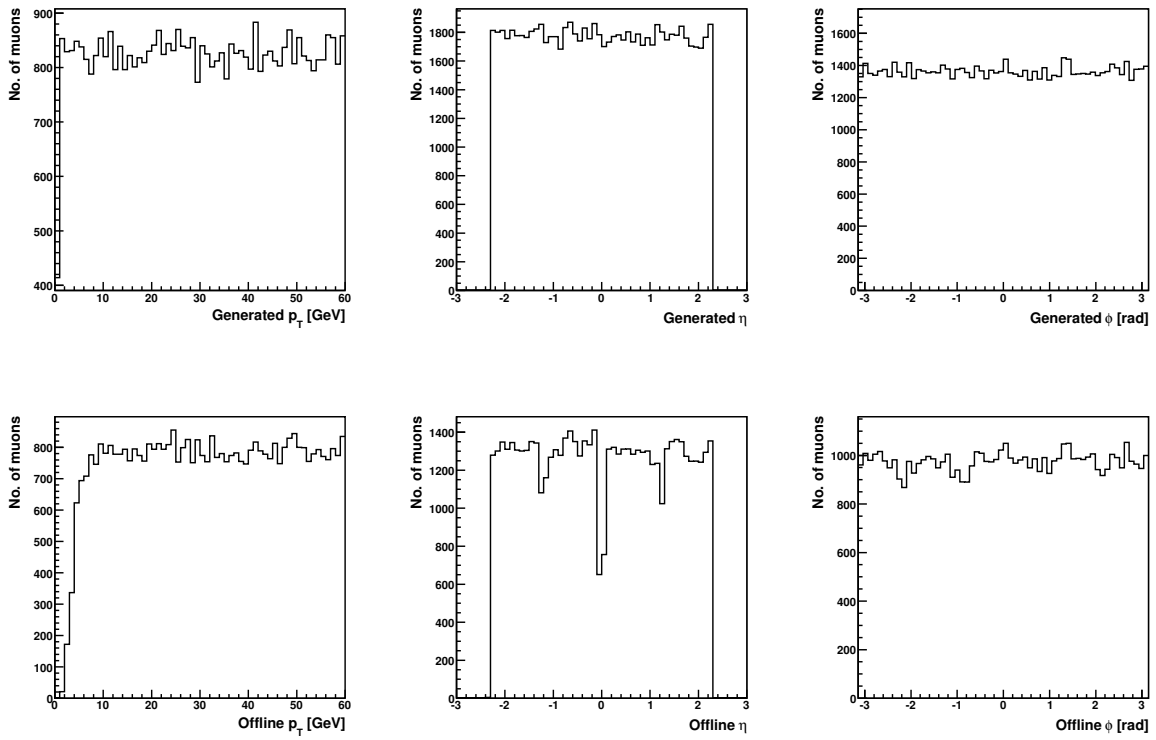

Figure F-3.10: Single muon kinematics (generated (top row) and offline (bottom row) variables), where all muons in the simulated sample were taken into account. Left: Muon transversal momentum (only upper constraint on p_{T} above 100 GeV); Middle: Muon pseudorapidity η in the centre-of-mass system; Right: Muon azimuthal angle ϕ.

For the higher Trigger levels, this is done by relating the triggered objects to the prior Trigger level, respectively.

The single muon efficiencies for all Trigger levels and all possible Trigger thresholds (6, 8, 10, 11, 20 and 40 GeV), parametrised in η and p_{T} respectively are shown in Figure F-3.11, including isolation criteria (where in the following isolation is defined by the energy deposited in the calorimeters in a ΔR-cone of 0.4 around the muon track $E_{\mathrm{ISO}}^{0.4} < 10\,\mathrm{GeV}$). These would resemble the High-Level Trigger Menus *mu6i*, *mu8i*, *mu10i*, *mu11i*, *mu20i* and *mu40i* as introduced in Chapter 2.4.4.

As expected from the resolution considerations made before, the p_{T} turn-on curves are sharper for the lower momentum thresholds, while in particular the LVL1 20 GeV and 40 GeV threshold turnons show exactly the described behaviour of a Gaussian Error Function with p_{T} dependent width, that is the turn-on not being symmetric with respect to the threshold value.

As a function of η, the Trigger efficiencies are basically constant over the whole range for the higher Trigger levels, while the LVL1 Trigger shows a different behaviour. The barrel region shows a decreased Trigger efficiency, mostly due to the ATLAS structural components, including feet, cryo and supply lines as mentioned before.

The statistical uncertainties of the efficiencies have been calculated with a Bayesian approach to account for the asymmetry of the underlying Binomial distribution the efficiency calculation is based on. This is discussed in more detail in the Appendix.

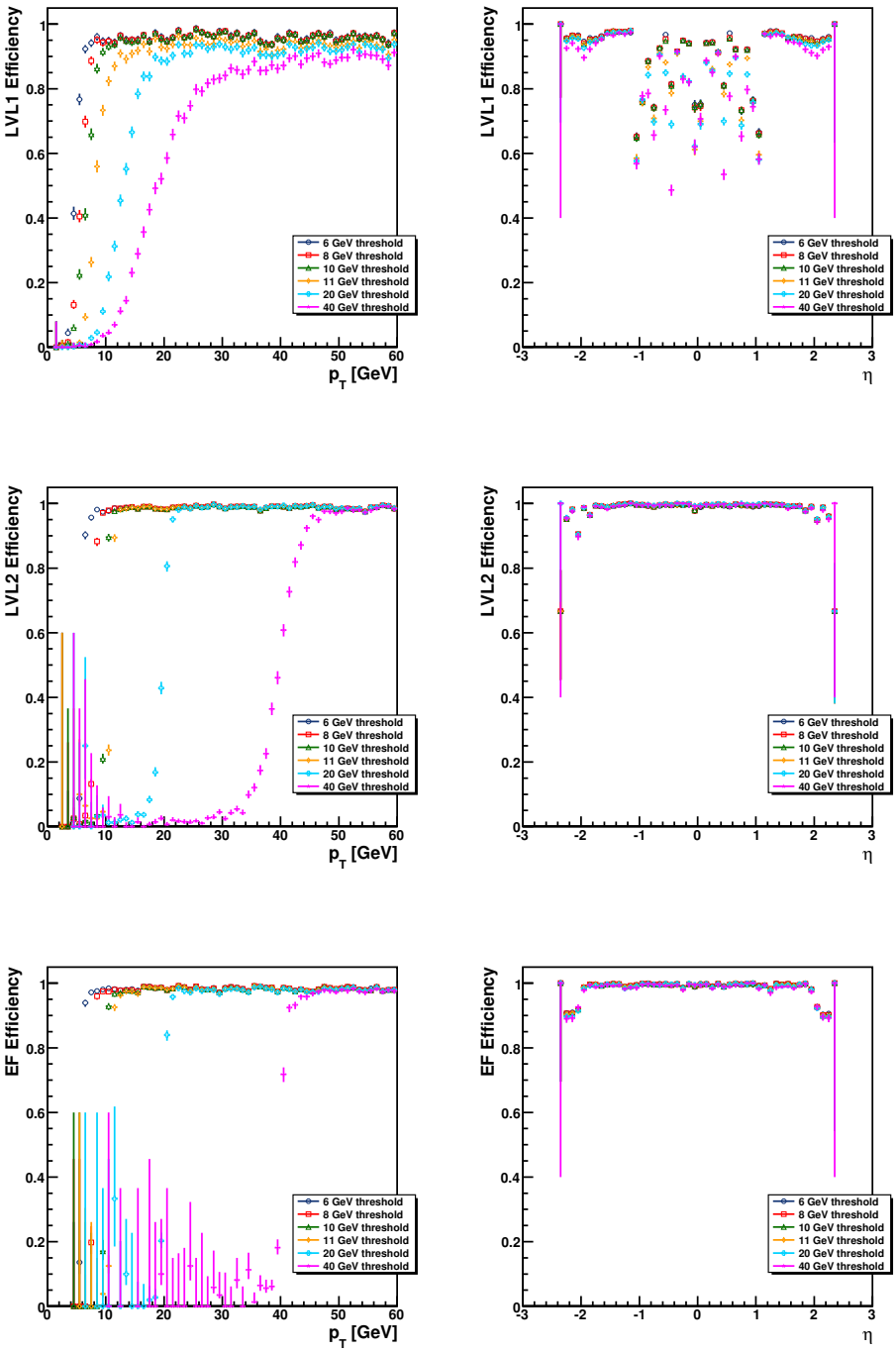

Figure F-3.11: Single muon Trigger efficiencies in p_{T} (left) and η (right), all available Trigger thresholds, determined with a Monte Carlo counting method. Top: LVL1; Middle: LVL2; Bottom: EF. All efficiencies are with respect to the prior Trigger level (or offline reconstruction level for LVL1 efficiency) and all p_{T} efficiencies have been corrected for detector acceptance. Efficiencies in η are shown for $p_{\mathrm{T}} > 1.25 \times$ Trigger threshold (plateau region only). Statistical uncertainties are calculated according to the method described in the Appendix.

3.2.1 Comparison of Single Muon Efficiencies and $Z^0/\gamma^* \to \mu\mu$ Efficiencies

In order to study the effects of the kinematics of the muons from the Z^0 decay, the Monte Carlo counting method is performed on the simulated $Z^0/\gamma^* \to \mu\mu$ sample in analogy to the single muon sample as a cross-check and to allow for a comparison.

When considering a single isolated muon with given η, ϕ and p_T, the Trigger efficiency is always identical for such a muon, no matter what its source may be. Thus, the resulting Trigger efficiency for one particular isolated muon from a single muon sample should be the same as for an identical muon from the $Z^0/\gamma^* \to \mu\mu$ process.

Nevertheless, when taking into account different process kinematics, it is expected that the integrated efficiencies (e.g. in η or p_T) show differences due to the loss of information when performing such an integration. This is depicted in Figure F-3.12, where the Trigger efficiencies in η and p_T are shown for both the single muons and the muons from the Z^0 sample in direct relation. As can be seen from the plots, the Trigger response is not identical for the two processes, especially on LVL1, where the impact of the kinematic differences is more pronounced.

Since the two processes obey different kinematics, it is very likely that the different Trigger response is due to the fact that the muons from the Z^0 decay are preferably produced in such a way that they emerge into detector regions with a lower Trigger probability, thus leading to a lower integrated Trigger efficiency. To be more precise, the Trigger efficiency for the higher levels in η is mostly constant over the whole rapidity range, as shown in the previous section, while this is not the case for the LVL1 Trigger. Thus, since muons from the Z^0 decay are preferably emerging into the barrel region (as shown in Figure F-3.3, where the LVL1 efficiency is basically lower than in the endcap region, the efficiency projection in p_T gets biased towards lower values, as observed.

Moreover, the integrated single muon efficiency ($0\,\mathrm{GeV} < p_T < 60\,\mathrm{GeV}$, separately for barrel and endcap) is higher than it is for the muons from the Z^0 decay, as shown in Table T-3.2.

Level	**Barrel Trigger efficiency**		**Endcap Trigger efficiency**	
	Single muons	$\mathbf{Z^0/\gamma^* \to \mu\mu}$	**Single muons**	$\mathbf{Z^0/\gamma^* \to \mu\mu}$
LVL1	$82.47^{+0.26}_{-0.25}\,\%$	$78.38^{+0.24}_{-0.23}\,\%$	$94.50^{+0.17}_{-0.16}\,\%$	$87.72^{+0.19}_{-0.19}\,\%$
LVL2	$91.65^{+0.19}_{-0.18}\,\%$	$83.60^{+0.22}_{-0.21}\,\%$	$91.38^{+0.16}_{-0.15}\,\%$	$81.34^{+0.21}_{-0.20}\,\%$
EF	$99.02^{+0.08}_{-0.07}\,\%$	$98.38^{+0.09}_{-0.08}\,\%$	$95.78^{+0.12}_{-0.11}\,\%$	$94.66^{+0.14}_{-0.13}\,\%$

Table T-3.2: Integrated Trigger efficiencies for single muons and muons from $Z^0/\gamma^* \to \mu\mu$ for barrel ($\eta \leq 1.0$) and endcap ($\eta > 1.0$) region ($0\,\mathrm{GeV} < p_T < 60\,\mathrm{GeV}$). Statistical uncertainties are calculated according to the method described in the Appendix.

As shown before, the resolution of the p_T measurement is not constant over the whole range. Thus, since the muons from $Z^0/\gamma^* \to \mu\mu$ follow a different (non-flat) transverse momentum distribution, this can create a bias in the integrated Trigger efficiency as well, in particular when considering that most muons produced by the Z^0 boson have large p_T.

If that hypothesis is true, the Trigger responses can be equalised by performing a reweighting of one of the two samples to the kinematic distribution of the second. Since the ϕ distributions are similar for both processes (cf. Figure F-3.3 and Figure F-3.10), the reweighting will be limited to two dimensions, η and p_T and will be performed at generator level.

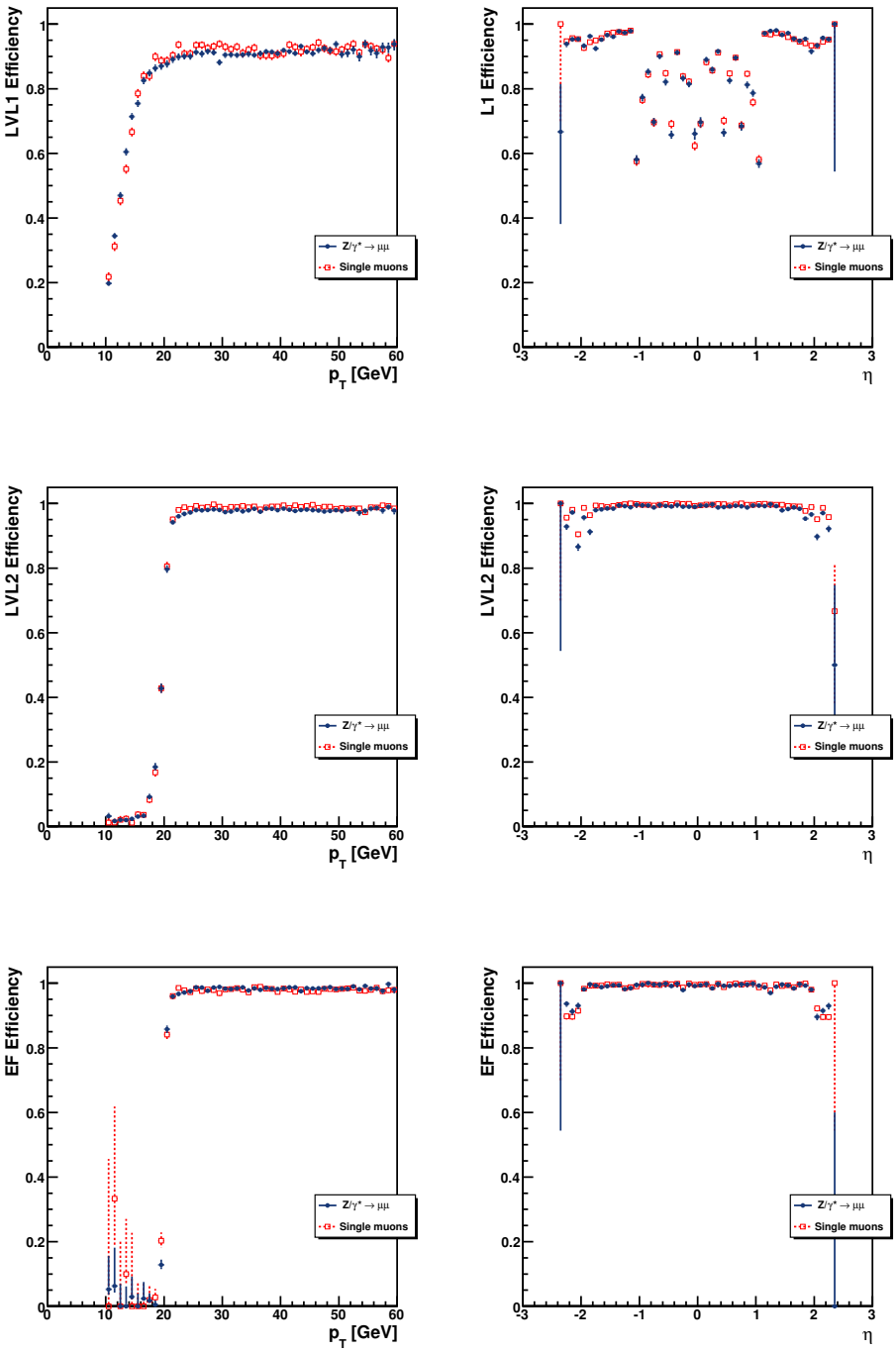

Figure F-3.12: Trigger efficiencies in p_{T} (left) and η (right) from single muons compared to muons from $\mathrm{Z}^0/\gamma^* \to \mu\mu$, determined with a Monte Carlo counting method. Top: LVL1; Middle: LVL2; Bottom: EF. All efficiencies are with respect to the prior Trigger level (or offline reconstruction level for LVL1 efficiency) and all p_{T} efficiencies have been corrected for detector acceptance. Efficiencies in η are shown for $p_{\mathrm{T}} > 25\,\mathrm{GeV}$ (plateau region only). Statistical uncertainties are calculated according to the method described in the Appendix.

In order to reweight the single muon kinematics to the $Z^0/\gamma^* \to \mu\mu$ kinematics (which is the physics process used for the development of the data method in the following), a two dimensional reweighting function was determined from single muon and $Z^0/\gamma^* \to \mu\mu$ events by calculating the binned reweighting ratio R_i of the normalised η-p_T distributions bin-by-bin i for all bins k (restricted to the region $|\eta| < 2.3$ and $p_T < 80\,\text{GeV}$). Empty bins were merged to adjacent bins where necessary to avoid discontinuities:

$$R_i = \frac{N_i^{Z^0/\gamma^* \to \mu\mu}}{N_i^{\text{single}}} \cdot \frac{\sum_{j=1}^{k} N_j^{\text{single}}}{\sum_{j=1}^{k} N_j^{Z^0/\gamma^* \to \mu\mu}} \quad ; \quad i = 1, \ldots, k \tag{3.7}$$

With the resulting reweighting function in η and p_T, which is shown in Figure F-3.13, the single

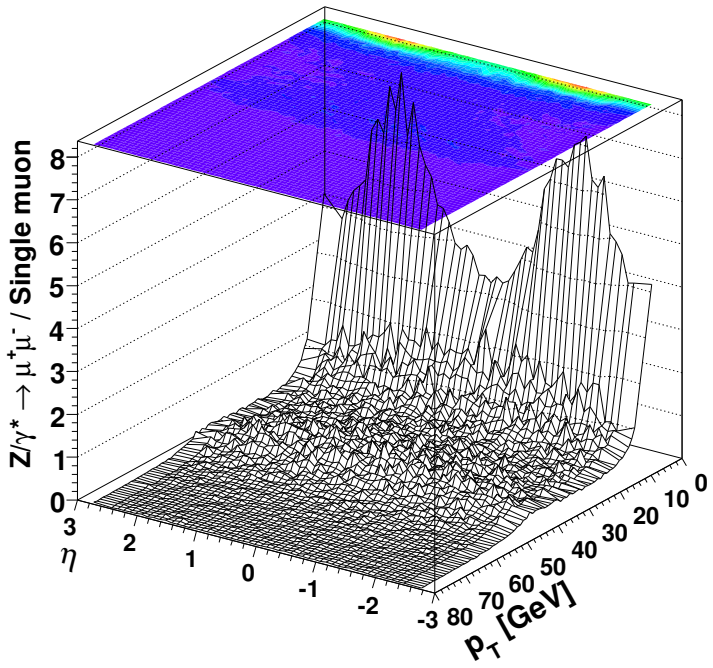

Figure F-3.13: Reweight function, parametrised in η and p_T. The relative uncertainty for the weight is of the order of 20 % in the region $0\,\text{GeV} < p_T < 60\,\text{GeV}$ and was calulated as described in the Appendix.

muon sample from the analysis can then be reweighted to the $Z^0/\gamma^* \to \mu\mu$ kinematics and a second comparison of Trigger efficiencies can be performed, which can be seen in Figure F-3.14.

As it is shown in the plots, the reweighted single muon kinematics now show a similar Trigger response as the true $Z^0/\gamma^* \to \mu\mu$ events within statistical uncertainties, in particular for the LVL1 p_T turn-on curve. The integrated efficiencies for the LVL1 Trigger confirm that, as summarised in Table T-3.3.

The LVL2 and EF results on the other hand are better with respect to the unweighted single muon kinematics while the LVL2 values are not compatible with the efficiencies for the $Z^0/\gamma^* \to \mu\mu$ decay within statistical uncertainties. This is caused by the bias in the LVL2 p_T estimate, which affects LVL2 and Event Filter slightly as well, since it is involved in both efficiency determinations. Only the LVL1 Trigger is unaffected by this bias and therefore yields consistent results.

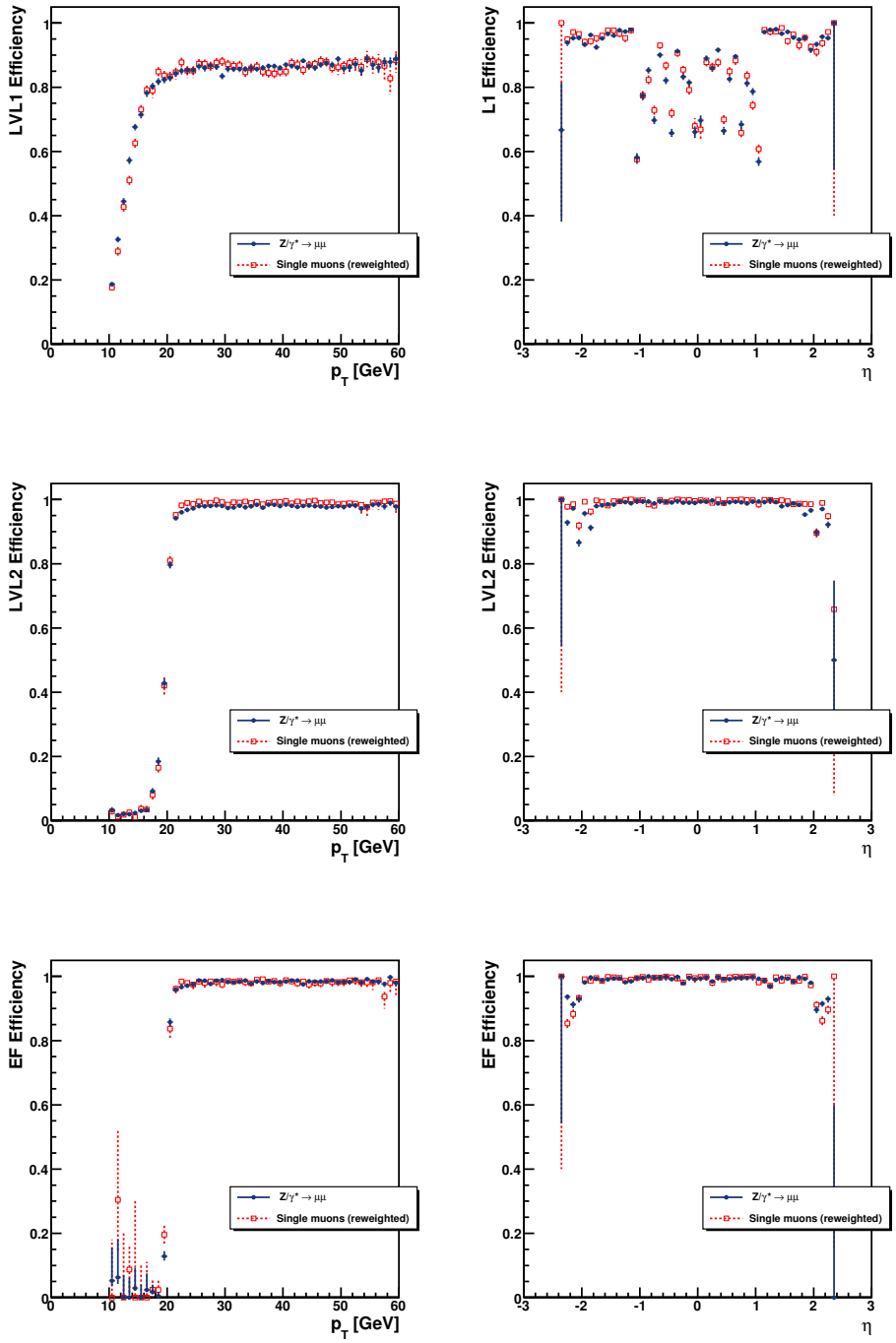

Figure F-3.14: Trigger efficiencies in p_{T} (left) and η (right) from single muons after kinematic reweighting compared to muons from $\mathrm{Z}^0/\gamma^* \to \mu\mu$, determined with a Monte Carlo counting method. Top: LVL1; Middle: LVL2; Bottom: EF. All efficiencies are with respect to the prior Trigger level (or offline reconstruction level for LVL1 efficiency) and all p_{T} efficiencies have been corrected for detector acceptance. Efficiencies in η are shown for $p_{\mathrm{T}} > 25\,\mathrm{GeV}$ (plateau region only). Statistical uncertainties are calculated according to the method described in the Appendix.

The stated hypothesis that the Trigger efficiency, when parametrised in η or p_{T}, only depends on the kinematics of the observed process is justified (although this could only be verified for the LVL1 Trigger for implementational reasons in the used ATHENA version). This means that the Trigger probability for a single, isolated muon does only depend on its location in the detector and its transverse momentum, regardless of the overall kinematics of the considered sample.

Level	**Barrel Trigger efficiency**		**Endcap Trigger efficiency**	
	Single muons (rew.)	$\mathbf{Z^0/\gamma^* \to \mu\mu}$	**Single muons (rew.)**	$\mathbf{Z^0/\gamma^* \to \mu\mu}$
LVL1	$78.32^{+0.37}_{-0.36}\,\%$	$78.38^{+0.24}_{-0.23}\,\%$	$88.21^{+0.29}_{-0.28}\,\%$	$87.72^{+0.19}_{-0.19}\,\%$
LVL2	$86.69^{+0.32}_{-0.31}\,\%$	$83.60^{+0.22}_{-0.21}\,\%$	$87.12^{+0.27}_{-0.26}\,\%$	$81.34^{+0.21}_{-0.20}\,\%$
EF	$98.85^{+0.12}_{-0.10}\,\%$	$98.38^{+0.09}_{-0.08}\,\%$	$95.26^{+0.19}_{-0.18}\,\%$	$94.66^{+0.14}_{-0.13}\,\%$

Table T-3.3: Integrated Trigger efficiencies for single muons, reweighted to $Z^0/\gamma^* \to \mu\mu$ kinematics and for muons from the actual $Z^0/\gamma^* \to \mu\mu$ sample itself for barrel ($\eta \leq 1.0$) and endcap ($\eta > 1.0$) region ($0\,\mathrm{GeV} < p_{\mathrm{T}} < 60\,\mathrm{GeV}$). Statistical uncertainties are calculated according to the method described in the Appendix.

This perception is a central point for this analysis, since it allows for the usage of Trigger efficiencies determined from one process on an entirely different process, if only well-parametrised.

3.2.2 Tag & Probe Method

In order to obtain the Trigger efficiency from data, a Monte Carlo counting method is no longer applicable as the non-triggered events are typically no longer available offline. Furthermore, it is not desireable to rely on Monte Carlo methods. To measure the Trigger efficiency from data, it is possible to select $Z^0/\gamma^* \to \mu\mu$ events from the data sample by application of a so called *Tag & Probe* data method, which is shown schematically in Figure F-3.15. The selection is achieved by making use of the fact that if one isolated muon is present in a $Z^0/\gamma^* \to \mu\mu$ event, there has to be a second muon in the observed event that is isolated as well, and on which the actual efficiency measurement can be performed. The basic concept of this method focuses on decoupling event selection and the actual determination of the Trigger efficiency to ensure the measurement to be done on objects from the studied process only without explicitly having to require isolation for the object from which the actual Trigger efficiency is obtained. For Trigger efficiency measurements from data it has to be taken into account that isolation depends on the instantaneous Luminosity due to interference with particles from other proton - proton collisions in the current bunch (*pile-up*). For this study, it is assumed that muons from the $Z^0/\gamma^* \to \mu\mu$ decay are always isolated.

These events can be selected by first identifying a muon that has definitively triggered the event, the *tag muon*. Moreover, several requirements are then to be applied to the tag muon, e.g. p_{T} and isolation criteria. To ensure the $Z^0/\gamma^* \to \mu\mu$ sample to be as pure as possible, these requirements should be very tight (leading to an enrichment with $Z^0/\gamma^* \to \mu\mu$ events).

If the tag muon meets all requirements, a second muon (if present) in the event is selected, the *probe muon,* which must comply to requirements that may be loosened with respect to the tag criteria since the probe muon is not involved in the actual event selection process. In this case, the same criteria as for the tag muon were chosen.

In addition to that, the dimuon invariant mass $M_{\mu\mu}$ has to sufficiently equal the Z^0 pole mass. If that is the case, there is a high probability that the constraint probe muon does not originate

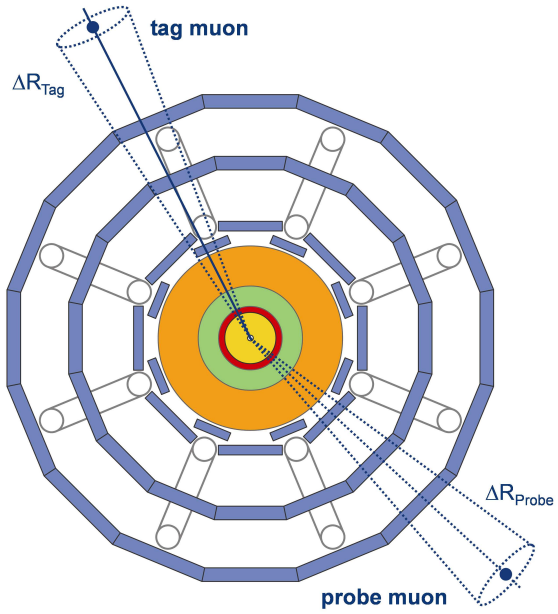

Figure F-3.15: The Tag & Probe Method. Event selection is done with the tag muon, while the actual Trigger efficiency is determined only with the probe muon to ensure independence of the two processes.

from a background process, but constitutes a muon from the $Z^0/\gamma^* \to \mu\mu$ signal.

The actual Trigger efficiency $\varepsilon_{\mathrm{TP}}$ for the Tag & Probe method can then be determined by the fraction of probe muons that have also been triggered, similar to the Monte Carlo counting method:

$$\varepsilon_{\mathrm{TP}} = \frac{\mathrm{N}_{\mu}^{\text{probe \& Trigger}}}{\mathrm{N}_{\mu}^{\text{probe}}}, \tag{3.8}$$

where both muons in an event are eligible as tag muon (if complying to the requirements) to enhance statistics.

Moreover, the applied criteria lead to an improvement of signal to background ratio in the sample. A detailed list of all applied requirements can be found in Table T-3.4.

Cut		Parameters
(1)	Transversal momentum (tag)	$p_T > 10\,\mathrm{GeV}$
(2)	Loose isolation (tag)	$E_{\mathrm{ISO}}^{0.4} < 10\,\mathrm{GeV}$ & High-Level triggered
(3)	Dimuon existence	$\exists$ second muon with $p_T > 10\,\mathrm{GeV}$
(4)	Tight isolation (probe)	$E_{\mathrm{ISO}}^{0.4} < 10\,\mathrm{GeV}$ for probe muon
(5)	Invariant mass (tag & probe)	$\lvert M_{\mathrm{Z}} - M_{\mu\mu}\rvert < 20\,\mathrm{GeV}$

Table T-3.4: Applied cuts for Tag & Probe method. These are object constraints (except for the invariant mass requirement) which are applied to offline variables. $E_{\mathrm{ISO}}^{0.4}$ is defined as the energy deposited in the calorimeters in a ΔR-cone of 0.4 around the reconstructed muon track. The invariant mass requirement constrains the dimuon invariant mass $M_{\mu\mu}$ to be within $\pm 20\,\mathrm{GeV}$ around the Z^0 pole mass M_{Z}.

After the transversal momentum (cut 1) and isolation (cut 2) constraints for the tag muon, an additional cut to ensure the existence of a second muon (cut 3) must be applied in order to deconvolute this probability from the probability of the probe muon to be isolated (cut 4). Finally, the invariant mass constraint (cut 5) is the only event requirement that links tag and probe muon in order to minimise the correlation between them.

Since this constraint directly relates the tag and the probe muon, it is obvious that the geometric correlation can create a bias in Trigger efficiency as well. This can, for example, be the case if one of the two muons produced in the Z^0 decay emerges into an acceptance gap of the detector, while the other muon is properly reconstructed. In the context of the Tag & Probe method, this muon could pass the tag muon criteria, but since there is no second muon in the event, no efficiency can be determined, the event not being taken into account at all. Hence, the Tag & Probe method does not cover any event where only one of the muons was found.

An exemplary cutflow for $Z^0/\gamma^* \to \mu\mu$ is shown in Table T-3.5, where the total object numbers together with the absolute and relative efficiencies for the respective requirements can be seen. Despite the fact that the applied criteria for background suppression have a strong impact on the signal sample as well, the absolute efficiency is still sufficient for an analysis.

muon CUT	**TOTAL NO.**	**ABS EFF.**	**REL EFF.**
no cut:	502 222	–	–
(1) $p_T > 10\,\mathrm{GeV}$	263 678	$52.50^{+0.07}_{-0.07}\%$	$52.50^{+0.07}_{-0.07}\%$
(2) $E^{0.4}_{\mathrm{ISO}} < 10\,\mathrm{GeV}$ + HLT	176 740	$35.19^{+0.07}_{-0.07}\%$	$67.03^{+0.09}_{-0.09}\%$
(3) $\exists\ 2^{\mathrm{nd}}$ muon	149 318	$29.73^{+0.06}_{-0.06}\%$	$84.48^{+0.09}_{-0.09}\%$
(4) $E^{0.4}_{\mathrm{ISO}}(2^{\mathrm{nd}}\mu) < 10\,\mathrm{GeV}$	145 752	$29.02^{+0.06}_{-0.06}\%$	$97.61^{+0.04}_{-0.04}\%$
(5) $\lvert M_{\mathrm{Z}} - M_{\mu\mu}\rvert < 20\,\mathrm{GeV}$	127 341	$25.36^{+0.06}_{-0.06}\%$	$87.37^{+0.09}_{-0.09}\%$

Table T-3.5: Tag & Probe cutflow for the muons from the $Z^0/\gamma^* \to \mu\mu$ sample, where the total number of objects (muons) is shown together with the respective absolute (with respect to the initial amount of objects) and relative cut efficiencies (with respect to the prior cut) for all applied constraints. The HLT p_{T} threshold used for the second requirement was 20 GeV.

3.2.3 Physics Background Sources

As mentioned before, real data consists not only of the $Z^0/\gamma^* \to \mu\mu$ process to be analysed, but contains (in most cases multiple) physics background processes as well. That is, events evoking detector signatures that are similar or identical to the ones caused by the reaction under study itself. Considering the $Z^0/\gamma^* \to \mu\mu$ process to be the analysis signal, this might be any event with two final state muons. In this context, the photon contribution to the Drell-Yan process in the Z^0 pole mass region may not be mistaken for background to the process itself, since the contribution is part of the overall physics interaction and may therefore not be neglected.

At the LHC (and at hadron colliders in general) with its 14 TeV centre-of-mass energy, the resulting multijet background is very high. As an example, the $b\bar{b}$ pair production dominates the $Z^0/\gamma^* \to \mu\mu$ process by several orders of magnitude, which can be seen in Figure F-2.11, making it a possible background when decaying into two final state muons via $W^{\pm}$ boson exchange.

This and some other potential physics background sources to $Z^0/\gamma^* \to \mu\mu$, mainly multijet processes, are illustrated with their respective leading order Feynman graphs in Figure F-3.16. These include, but are not limited to $b\bar{b} \to \mu\mu X$, $c\bar{c} \to \mu\mu X$, $t\bar{t} \to \mu\mu X$ and $Z^0 \to \tau\tau \to \mu\mu X$.

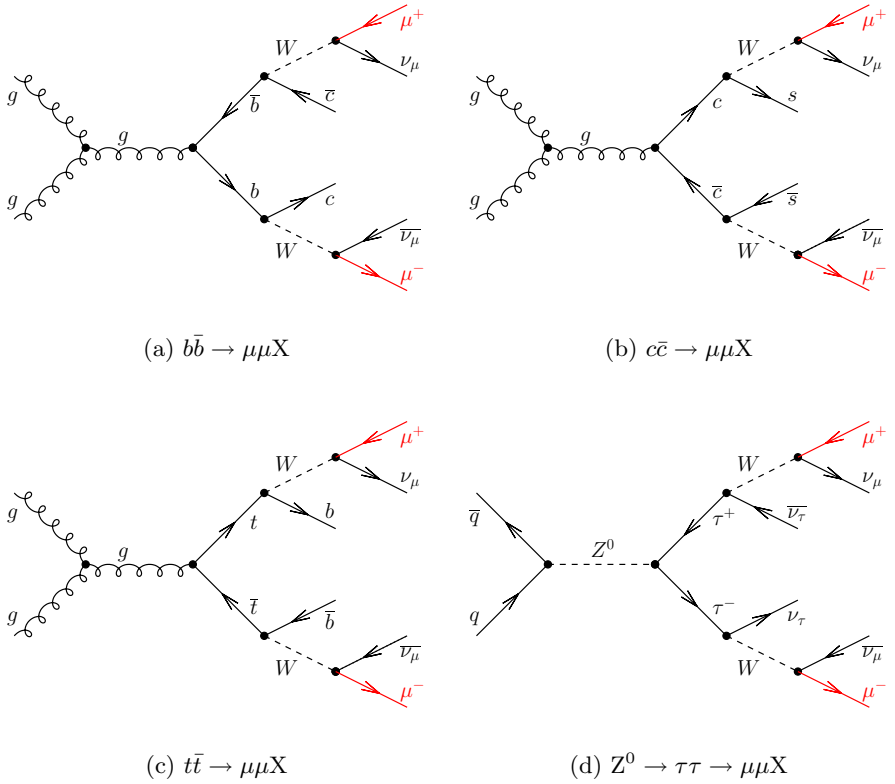

(a) $b\bar{b} \to \mu\mu X$ (b) $c\bar{c} \to \mu\mu X$

(c) $t\bar{t} \to \mu\mu X$ (d) $Z^0 \to \tau\tau \to \mu\mu X$

Figure F-3.16: Leading order Feynman graphs for some potential physics background sources to $Z^0/\gamma^* \to \mu\mu$.

The effects of the different requirements introduced in the previous section on the respective distributions of the signal and background samples without any scaling can be seen in Figure F-3.17, where these have been stacked for all analysed samples, each distribution prior to the corresponding kinematic constraint.

Apparently, the requirement on the muon transverse momentum is very effective to suppress background, in particular for the contribution from the multijet background samples and the low p_T photon contribution from Drell-Yan. The invariant mass constraint is very effective to suppress the $Z^0 \to \tau\tau \to \mu\mu X$ contribution to the background, since the invariant mass distribution of the muons emanating from the taus is biased towards lower masses due to the neutrinos carrying away transverse momentum in the decay process. An additional jet multiplicity cut may especially be used to further reduce the background from remaining $t\bar{t} \to \mu\mu X$ events (and of course all other multijet background contributions), since these events have a high jet multiplicity in the majority of cases. This was not performed in the following, while the corresponding distributions are shown in Figure F-3.17 for completeness.

Since the Trigger efficiency for a particular muon does not depend on its origin, these physics background sources should not affect the actual Tag & Probe measurement, which will be analysed in the following section of this chapter.

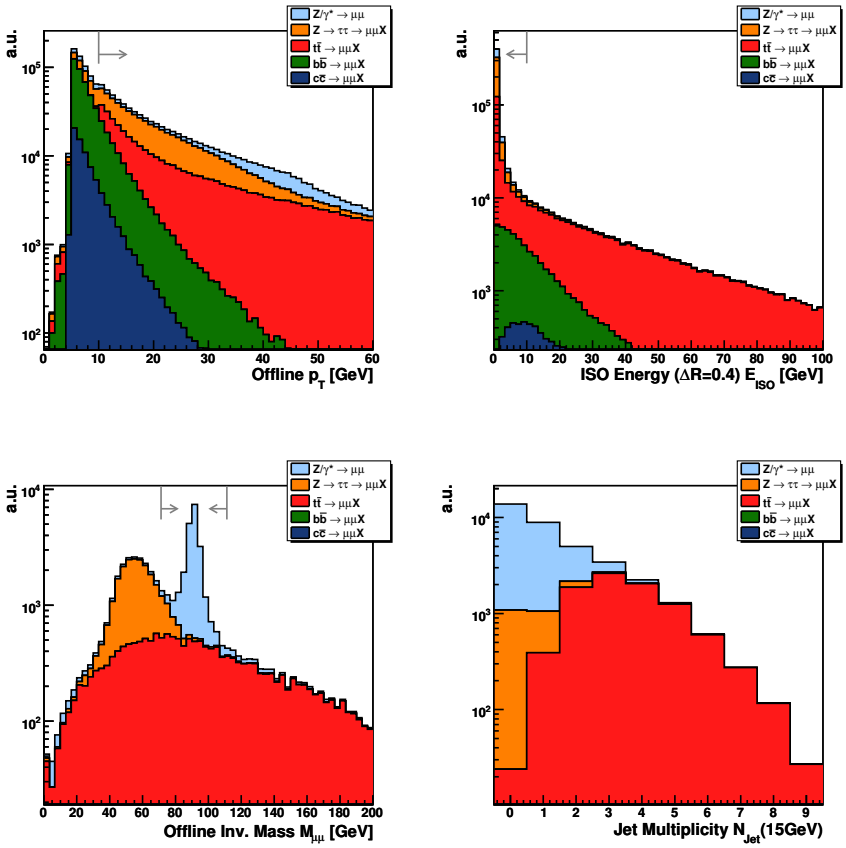

Figure F-3.17: Distributions of the kinematic variables in the cutflow process. Top left: transverse momentum prior to p_T constraint; Top right: Isolation energy prior to E_{ISO} constraint; Bottom left: Invariant mass prior to $M_{\mu\mu}$ constraint; Bottom right: Jet Multiplicity after $M_{\mu\mu}$ constraint. Arrows indicate kinematic cuts.

3.2.4 Comparison of Monte Carlo Counting Method and Tag & Probe Method

To analyse and quantify a possible bias introduced by the Tag & Probe method (in particular considering the presence of physics background), a direct comparison of the Trigger efficiencies from the Monte Carlo counting method and the actual data method was performed with the constraints applied as introduced in the previous section. The Trigger efficiencies in η and p_T can be found in Figure F-3.18. Evidently, the results are in very good agreement for all Trigger levels within the statistical uncertainties.

In addition, the effect of an admixture of the simulated physics background processes on the consistency of counting and Tag & Probe method is to be analysed. In order to do so, the events from the $b\bar{b} \to \mu\mu X$, $c\bar{c} \to \mu\mu X$, $t\bar{t} \to \mu\mu X$ and $Z^0 \to \tau\tau \to \mu\mu X$ samples were added to the signal without any relative normalisation and the comparison of both methods was repeated. The results are shown in Figure F-3.19.

Both methods are in good agreement, regardless of the physics background contribution as expected from the fact that the Trigger efficiency for a muon does not depend on the kinematics of the underlying process. Hence, the introduced requirements successfully suppress the physics background sources that were generated.

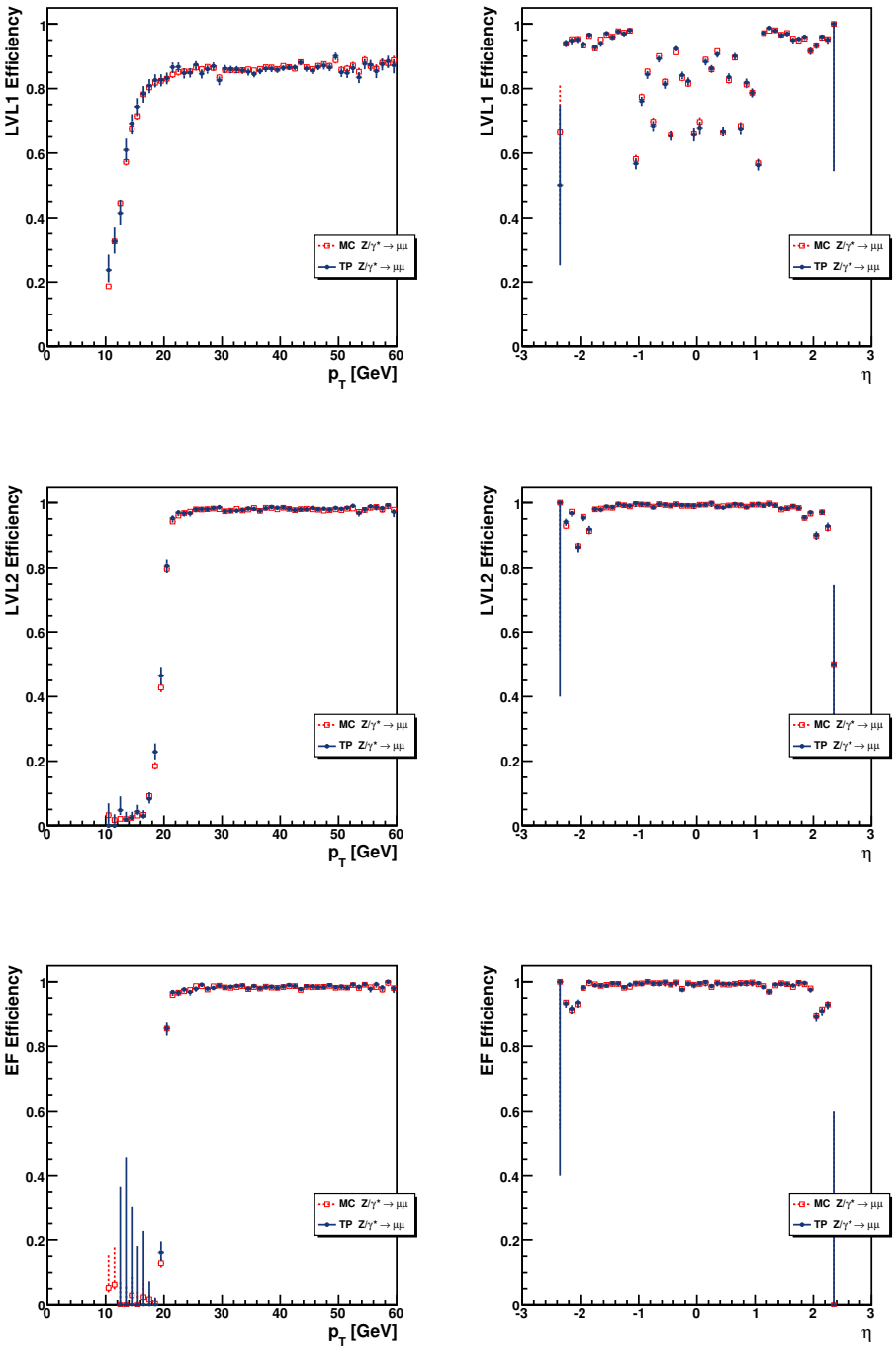

Figure F-3.18: Trigger efficiencies in p_{T} (left) and η (right) from the Tag & Probe data method compared to a Monte Carlo counting method. Top: LVL1; Middle: LVL2; Bottom: EF. All efficiencies are with respect to the prior Trigger level (or offline reconstruction level for LVL1 efficiency) and all p_{T} efficiencies have been corrected for detector acceptance. Efficiencies in η are shown for $p_{\mathrm{T}} > 25\,\mathrm{GeV}$ (plateau region only). Statistical uncertainties were calculated according to the method described in the Appendix.

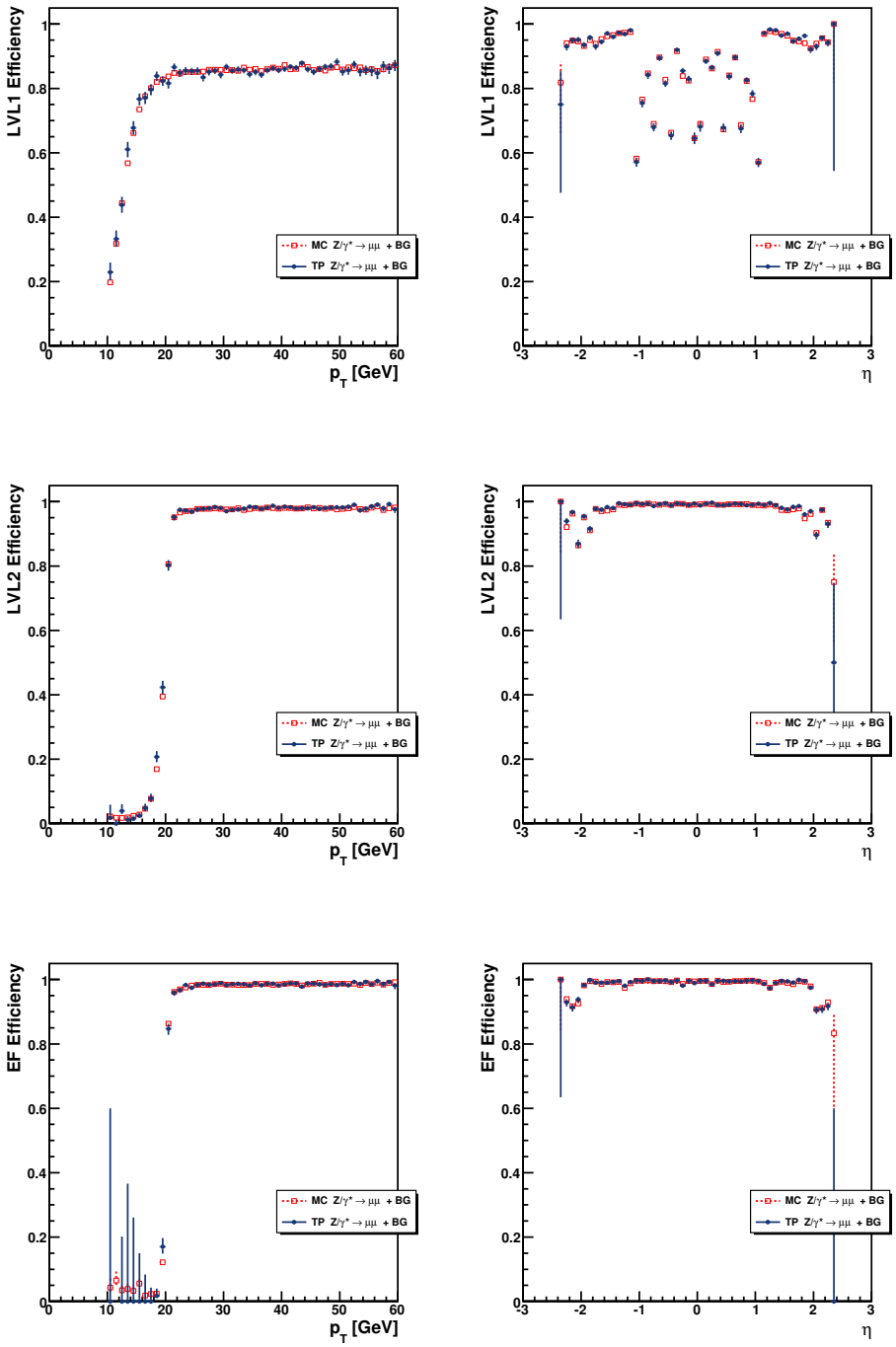

Figure F-3.19: Trigger efficiencies in p_{T} (left) and η (right) from Tag & Probe data method and Monte Carlo counting method, including the background contributions explained in the text (no relative scaling). Top: LVL1; Middle: LVL2; Bottom: EF. All efficiencies are with respect to prior Trigger level (or offline reconstruction level for LVL1 efficiency), p_{T} efficiencies have been corrected for detector acceptance. Efficiencies in η are shown for $p_{\mathrm{T}} > 25\,\mathrm{GeV}$ only. Stat. uncertainties are calculated according to the method described in the Appendix.

3.2.5 Comparison to $Z^0/\gamma^* \rightarrow ee$ Process

A similar method for the measurement of Trigger efficiencies for the electron channel is currently being developed at the University of Hamburg [52].

A comparison of Monte Carlo counting method and Tag & Probe method for both channels at all Trigger levels (without background taken into account) is shown in Figure F-3.20, where both methods and both channels are plotted together.

As can be seen, the Trigger efficiencies determined with the Tag & Probe method are in good agreement with Monte Carlo counting methods for both muon and electron Trigger. The resulting turn-on curves differ in shape and saturation level, especially on the first Trigger level, where the electron Trigger yields a higher plateau efficiency than the muon Trigger and a better coverage in η, while the LVL1 muon Trigger is more inclusive with respect to the p_{T} range.

The LVL2 Trigger situation is different to LVL1, since the plateau efficiencies for the muon Trigger are higher throughout the whole p_{T} range and the pseudorapidity coverage is slightly better, especially in the endcaps.

On EF level, both channels yield a similar and very steep turn-on at about 20 GeV and a saturation at almost 100 % efficiency in the plateau range, while the efficiency in η is almost flat over the complete range.

Regardless of the different Trigger concepts that are obviously used for muons and electrons, the Tag & Probe method yields consistent results for both Trigger slices.

3.2.6 Instrumental Background & Matrix Method

Unlike physics background, the occurrence of instrumental background can have an effect on the introduced method, where possible sources of instrumental background are in general:

- Falsely identified particles, e.g. pions, mistakenly identified as electrons in the detector or particles penetrating the calorimeters (*punch-through*) and advancing into the Muon Chambers (*fake muons*).
- Fake isolation (particles or energy depositions in the respective cone around the track are not or only partly detected) due to detector inacceptances and different isolation energy distributions (can be different for signal and physics background).
- Fake missing transverse energy, e.g. from calorimeter effects.

In the particular case of the ATLAS experiment it is assumed that muons are not very likely to be faked since the detector design should prohibit calorimeter punch-through effects, as explained in the calorimeter section of Chapter 2. Since the High-Level Trigger applies isolation criteria to the muons, only fake isolated muons constitute a potential instrumental background source for the study of muon Trigger efficiencies at ATLAS. Since the efficiency measurements to be conducted on the $Z^0/\gamma^* \rightarrow \mu\mu$ sample are relying on the Trigger isolation criteria, fake isolated muons should not be taken into account for the measurement of the Trigger efficiency. Although appearing as such, they are not part of the signal process, making it necessary to estimate the instrumental background contribution to the $Z^0/\gamma^* \rightarrow \mu\mu$ sample (here defined as signal).

Due to the fact that instrumental background is based on detector effects, it is much more difficult to simulate, especially with respect to reliability of the detector response simulation. In addition, the huge rate of dominating semileptonic decys of multijet events and the assumptions made on hadronic fragmentation aggravate the simulation process. Hence, it is not desirable

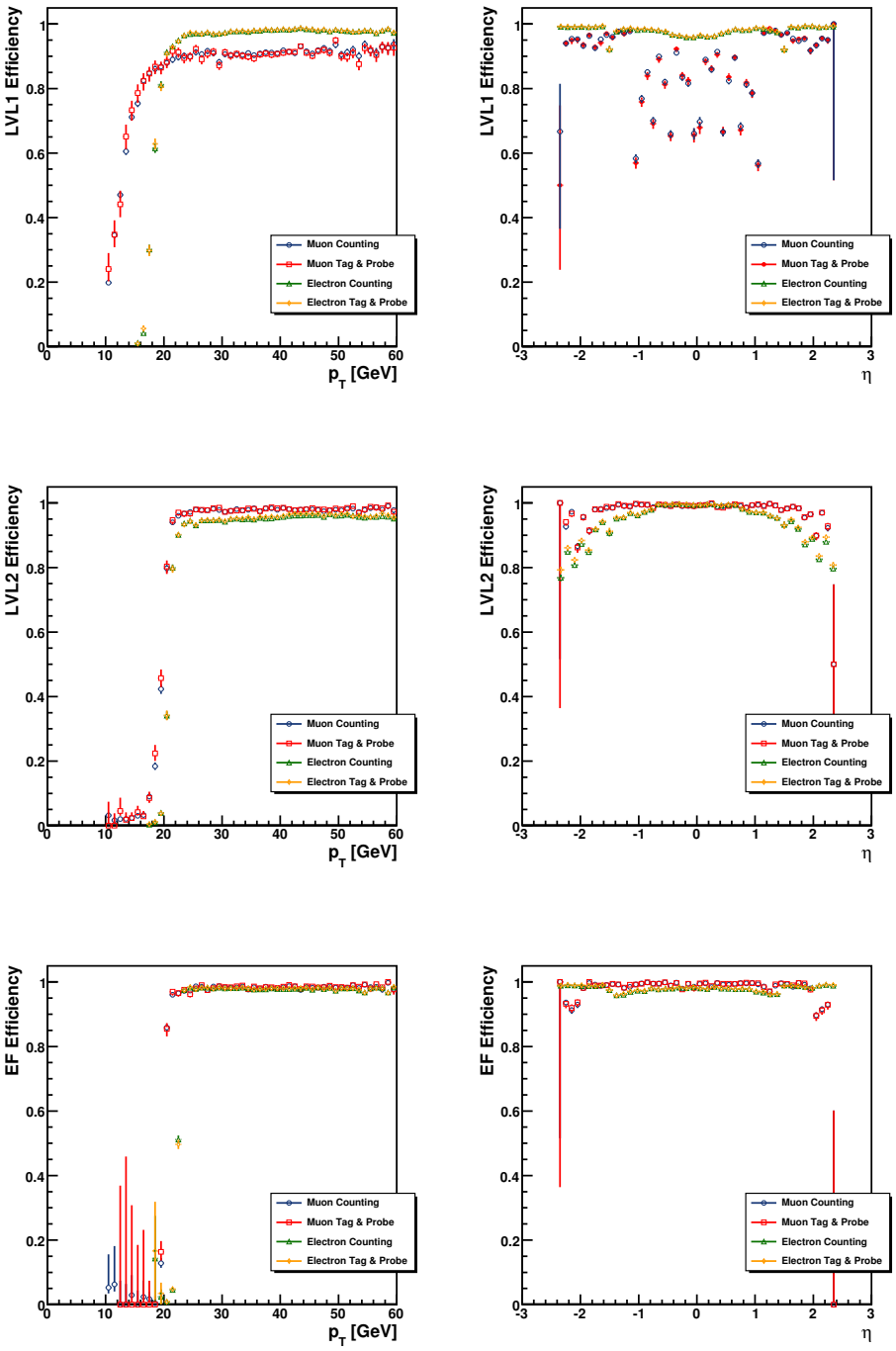

Figure F-3.20: Trigger efficiencies in p_{T} (left) and η (right) from the Tag & Probe data method compared to a Monte Carlo counting method for both the muon channel and the electron channel [52]. Top: LVL1; Middle: LVL2; Bottom: EF. All efficiencies are with respect to the prior Trigger level (or offline reconstruction level for LVL1 efficiency) and all p_{T} efficiencies have been corrected for detector acceptance. Efficiencies in η are shown for $p_{\mathrm{T}} > 25\,\mathrm{GeV}$ only. Statistical uncertainties for the muon Trigger were calculated according to the method described in the Appendix. For the electron Trigger, binomial uncertainties were assumed.

to rely on simulations to determine the instrumental background contribution and therefore, simulations are performed only for testing and verification purposes.

In order to estimate the fraction of instrumental background within a data sample, a data method, in this instance the Matrix Method [53], is utilised, which allows to statistically separate two contributions to a data sample.

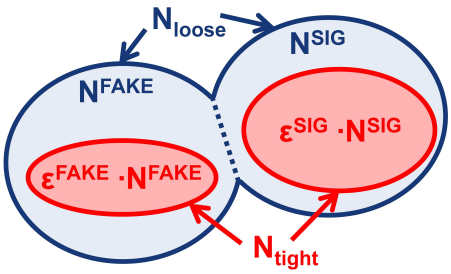

Figure F-3.21: An illustration of the Matrix Method and its effect on the underlying sample subsets.

The Matrix Method defines two subsets N_{loose} and N_{tight} of the data sample with respect to a particular object requirement from the cutflow, in this case the tight isolation constraint for the probe muon. Prior to the cut, the sample N_{loose} is the sum of the signal and the background contributions N^{SIG} and N^{FAKE}:

$$N_{\text{loose}} = N^{\text{SIG}} + N^{\text{FAKE}} \tag{3.9}$$

Afterwards, the tight isolation constraint is applied, which is passed by signal events with an efficiency of ε^{SIG} and by background events with an efficiency $\varepsilon^{\text{FAKE}}$. Hence, after the cut, the tight sample N_{tight} is the efficiency weighted sum of the original signal and background contributions, with the respective efficiencies for the isolation requirement for both fractions:

$$N_{\text{tight}} = \varepsilon^{\text{SIG}} N^{\text{SIG}} + \varepsilon^{\text{FAKE}} N^{\text{FAKE}} \tag{3.10}$$

This situation is illustrated in Figure F-3.21. The linear system of two equations with two unknown variables can be rewritten as matrix equation:

$$\begin{pmatrix} N_{\text{loose}} \\ N_{\text{tight}} \end{pmatrix} = \begin{pmatrix} 1 & 1 \\ \varepsilon^{\text{SIG}} & \varepsilon^{\text{FAKE}} \end{pmatrix} \begin{pmatrix} N^{\text{SIG}} \\ N^{\text{FAKE}} \end{pmatrix} \tag{3.11}$$

Solving this matrix equation yields the signal and background contributions in the data sample prior to the isolation cut:

$$N^{\text{FAKE}} = \frac{N_{\text{tight}} - \varepsilon^{\text{SIG}} N_{\text{loose}}}{\varepsilon^{\text{FAKE}} - \varepsilon^{\text{SIG}}} \tag{3.12}$$

$$N^{\text{SIG}} = \frac{\varepsilon^{\text{FAKE}} N_{\text{loose}} - N_{\text{tight}}}{\varepsilon^{\text{FAKE}} - \varepsilon^{\text{SIG}}} \tag{3.13}$$

The corresponding statistical uncertainties are calculated by taking into account the underlying distributions of the variables (which are known) and modelling the joint probability density of N^{FAKE} and N^{SIG}, respectively. This is performed with a Markov Chain method implemented in the Bayesian Analysis Toolkit [54].

While calculating the signal and background fractions from N_{loose} and N_{tight} is elementary given that the isolation efficiencies are known, determining those can be difficult. Since the respective selection efficiencies for the isolation requirements have to be derived independently by selecting representative signal and background events, specific methods have to be developed to obtain them from data.

A Method to determine $\varepsilon^{\mathrm{FAKE}}$ and $\varepsilon^{\mathrm{SIG}}$

In order to measure the efficiencies for the isolation criterion from a data sample, it is possible to proceed in a similar way as for the Tag & Probe method introduced earlier. Again, it is necessary to decouple event selection and efficiency determination, where the applied requirements should be as tight as possible to separate the signal and background fractions as effectively as feasible.

The isolation efficiency for the signal sample $\varepsilon^{\mathrm{SIG}}$ can be obtained again by requiring an isolated muon with high transverse momentum that has triggered the event as a tagging criterion in analogy to the Tag & Probe method for Trigger efficiency, as depicted in Figure F-3.22. If

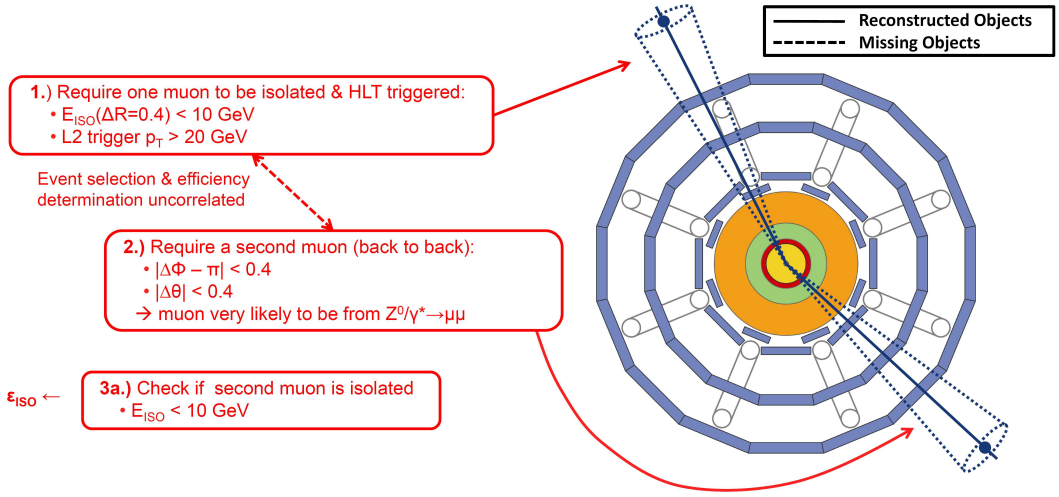

Figure F-3.22: Overview of the method to determine the isolation efficiency for the signal contribution from data.

the tag muon is accepted and another high p_{T} muon is present in the event, a dimuon invariant mass constraint with an increased tightness is applied to the tag and probe muons to further enhance the signal to background ratio. In addition, a cut on the jet multiplicity is performed to suppress particularly multijet background sources.

The isolation cut efficiency can then be determined by the fraction of isolated probe muons in the sample:

$$\varepsilon^{\mathrm{SIG}} = \frac{\mathrm{N}_{\mu}^{\mathrm{probe\,\&\,ISO}}}{\mathrm{N}_{\mu}^{\mathrm{probe}}} \tag{3.14}$$

Similarly, the fake efficiency $\varepsilon^{\mathrm{FAKE}}$ can be obtained by implementing a different tagging criterion to select the background fraction in the sample, which can be seen in Figure F-3.23.

As mentioned earlier, instrumental background for the $\mathrm{Z}^0/\gamma^* \rightarrow \mu\mu$ process is constituted by fake isolated muons. This can be the case if a jet, e.g. from $b\bar{b}$, contains a muon while the jet is not or only partly identified. Hence, the energy deposition around the muon may pass the isolation criterion despite the muon being not isolated. If a highly energetic jet is detected within an event and a high p_{T} muon is present in the opposite hemisphere of the detector, most probably it is not isolated. Hence, if the isolation energy for the muon is below the isolation threshold, the isolation is assumed to be faked.

Thus, a highly energetic jet that has triggered the event is required for the event to be perceived as background. If a high p_{T} muon is present in the opposite hemisphere of the detector, the fake

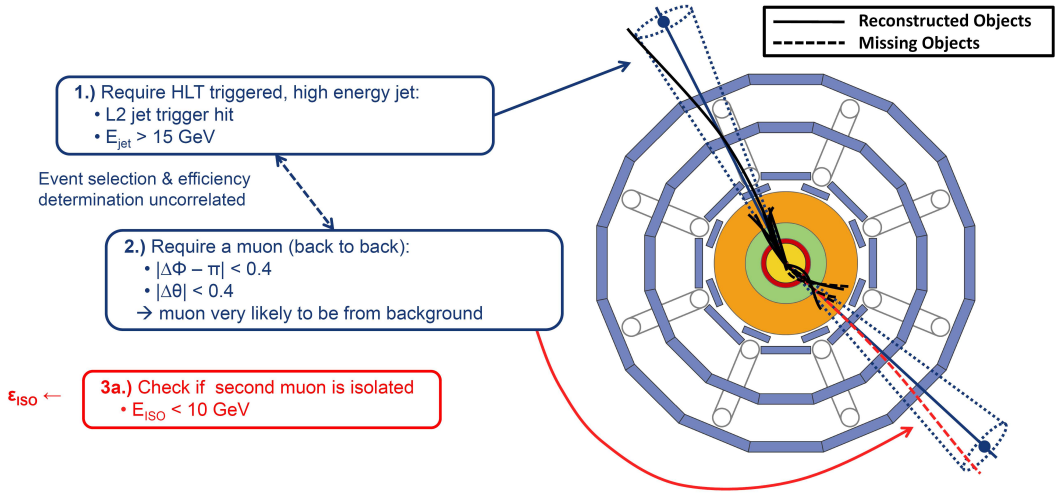

Figure F-3.23: Overview of the method to determine the isolation efficiency for the background contribution from data.

efficiency for that muon is given by

$$\varepsilon^{\mathrm{FAKE}} = \frac{\mathrm{N}_{\mu}^{\mathrm{probe\,\&\,ISO}}}{\mathrm{N}_{\mu}^{\mathrm{probe}}}. \tag{3.15}$$

3.2.7 Tests and Results for $\mathrm{Z}^0/\gamma^* \to \mu\mu$ Signal and $\mathrm{b\bar{b}} \to \mu\mu\mathrm{X}$ Background

To perform a basic consistency check of the introduced methods, it is possible to separately apply them to a simulated signal and background sample, respectively. Since the composition of the loose sample N_{loose} is known in this case, it can then be verified whether the Matrix Method yields consistent results with the derived cut efficiencies as a simple cross-check.

To perform the test, a $\mathrm{Z}^0/\gamma^* \to \mu\mu$ sample and a $b\bar{b} \to \mu\mu\mathrm{X}$ sample (both scaled to $1\,\mathrm{fb}^{-1}$) were analysed independently with the methods introduced in the previous section. The $\mathrm{Z}^0/\gamma^* \to \mu\mu$ sample was generated with at least two final state muons with a minimum p_{T} of 5 GeV. The $b\bar{b} \to \mu\mu\mathrm{X}$ sample had to be preselected more strongly on generator level in order to facilitate generation of an acceptable amount of events suitable for this analysis. Hence, the bottom and antibottom quarks were constraint to be generated with a minimum p_{T} of 6 GeV both and at least one final state muon with a minimum p_{T} of 5 GeV was required to generate the necessary sample within a reasonable amount of computing time. For further information on the applied preselection, refer to the Appendix.

The reconstructed amount of muons in the samples prior to the tight isolation constraint (and therefore the expected results for the background and signal fraction $N_{\mathrm{exp}}^{\mathrm{FAKE}}$ and $N_{\mathrm{exp}}^{\mathrm{SIG}}$) are

$$N_1^{\mathrm{FAKE}} = N_{\mathrm{exp}}^{\mathrm{FAKE}} = 273.1 \cdot 10^3 \quad \text{and} \quad N_1^{\mathrm{SIG}} = N_{\mathrm{exp}}^{\mathrm{SIG}} = 687.7 \cdot 10^3,$$

and in analogy, after the cut:

$$N_2^{\mathrm{FAKE}} = 160.3 \cdot 10^3 \quad \text{and} \quad N_2^{\mathrm{SIG}} = 668.9 \cdot 10^3,$$

Hence, the resulting total muon counts N_{loose} respectively N_{tight} before and after the cut for this test are given by

$$N_{\mathrm{loose}} = 960.8 \cdot 10^3 \quad \text{and} \quad N_{\mathrm{tight}} = 829.2 \cdot 10^3,$$

The signal and fake efficiencies obtained from the samples are

$$\varepsilon^{\mathrm{FAKE}} = \left(58.71^{+0.79}_{-0.76}\right)\ \% \quad \text{and} \quad \varepsilon^{\mathrm{SIG}} = \left(97.27^{+0.09}_{-0.07}\right)\ \%$$

With these results, the Matrix Method yields the following signal and background fractions:

$$N^{\mathrm{FAKE}} = \left(286.6^{+4.0}_{-4.6}\right) \cdot 10^3 \quad \text{and} \quad N^{\mathrm{SIG}} = \left(674.2^{+4.6}_{-4.0}\right) \cdot 10^3$$

Apparently, the results do not entirely coincide with the values the method should be able to reproduce, which is due to the preselection of the $b\bar{b} \to \mu\mu\mathrm{X}$ sample on generator level. This can be shown by using a different $b\bar{b} \to \mu\mu\mathrm{X}$ sample with different generator requirements. This was done with stronger constraints on the bottom and antibottom quarks, which were both constrained to have a minimum p_{T} of 12 GeV and by additionally requiring two muons with transversal momentum above 5 GeV instead of only one. More precisely, the preselection leads to a direct correlation of the muon isolation in the sample. The resulting correlation coefficients for the isolation energy E_{ISO} for two muons used for the determination of the isolation selection efficiency are

$$\mathrm{corr}(\mu_1, \mu_2)_{\mathrm{S1}} = 0.25$$

for the $b\bar{b} \to \mu\mu\mathrm{X}$ sample (S1) that was used for the Matrix Method test and

$$\mathrm{corr}(\mu_1, \mu_2)_{\mathrm{S2}} = 0.41$$

for the second sample (S2) with tighter generator constraints.

As can be seen, the isolation energy of both muons is correlated, where the effect is more pronounced for the second $b\bar{b} \to \mu\mu\mathrm{X}$ sample with the strengthened constraints. Since there were no additional constraints applied to the sample, this correlation can only be caused by the applied generator requirements.

This can be further optimised by loosening the generator requirements to a minimum in order to create a more representative sample for the $b\bar{b} \to \mu\mu\mathrm{X}$ background. But taking this into account, the Matrix Method already yields a very good estimate for the fraction of background in the analysed samples.

4 Applications of the Developed Method

As a further closure test of the developed methods, it is possible to apply the efficiencies determined from the $Z^0/\gamma^* \rightarrow \mu\mu$ sample to different simulated physics processes. This is done by weighting the corresponding kinematic distributions in η and p_T of the samples with the obtained efficiency map in η and p_T, weighting offline with LVL1 efficiencies, LVL1 matched offline muon kinematics with LVL2 efficiencies and LVL2 matched offline muons with EF efficiency, which are shown in Figure F-4.1 for all Trigger levels. Without actually having to use the contained Trigger information of the analysed samples this allows for the determination of the respective Trigger efficiencies. These can then be compared to the corresponding efficiencies from a Monte Carlo counting method performed on the samples directly.

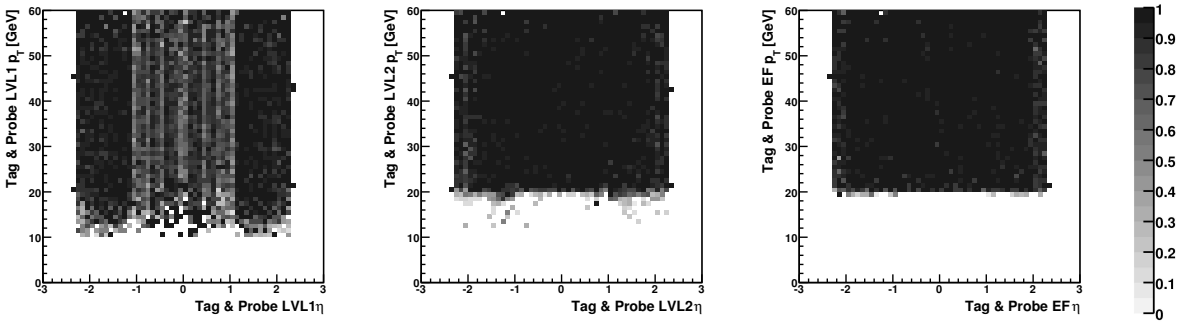

Figure F-4.1: Trigger Efficiencies, parameterised in η and p_T, determined with the Tag & Probe method from the simulated $Z^0/\gamma^* \rightarrow \mu\mu$ sample. Left: LVL1; Middle: LVL2; Right: EF. All efficiencies are with respect to the prior Trigger level (or offline reconstruction level for LVL1 efficiency). Light grey refers to low efficiency, dark grey to high efficiency. White refers to acceptance gaps or incalculable efficiencies.

To cover different processes and dependencies, three samples with different kinematics and different muon multiplicities were generated and tested:

- A Single Top sample, generated with at least one muon per event (production by $W^{\pm}$ exchange, without restriction to a specific decay channel).
- A $t\bar{t}$ sample, generated with at least two muons per event (without restriction to a specific decay channel).
- The SU1 (coannihilation) multi lepton Supersymmetry (*SUSY*) [55] sample (taken from CSC MC Production [56]).

There was no constraint on the origin of any muons applied in the samples (e.g. if they originate from a b jet or the $W^{\pm}$ decay). In addition, several instrumental background admixtures to the samples were simulated by adding a $b\bar{b} \rightarrow \mu\mu X$ sample with different normalisations to the three

processes prior to the application of the efficiency maps. The background distribution in p_{T} is shown in F-4.2.

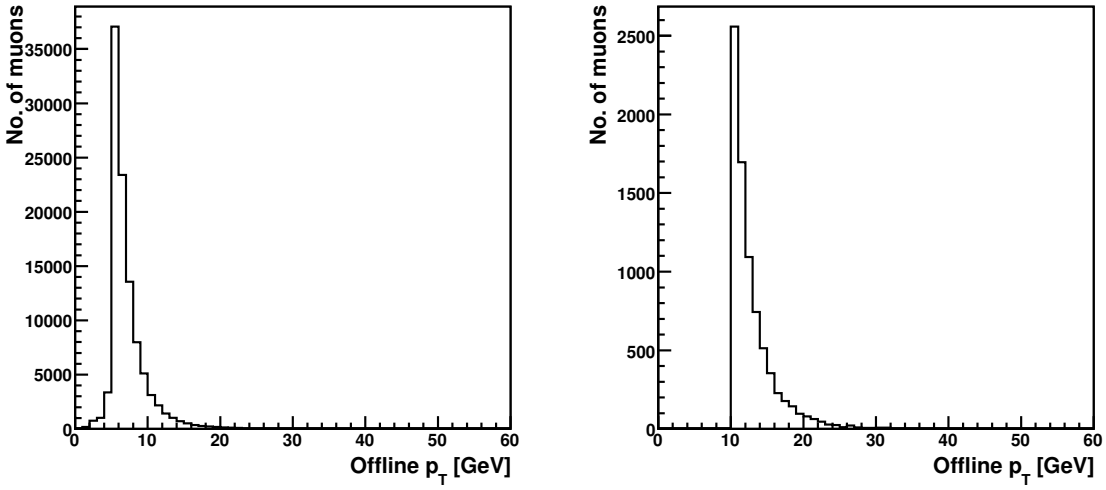

Figure F-4.2: offline kinematics in p_{T} for the $b\bar{b} \rightarrow \mu\mu\mathrm{X}$ background sample. Left: Prior to constraints on transverse momentum ($p_{\mathrm{T}} < 10\,\mathrm{GeV}$) and isolation energy ($E_{\mathrm{ISO}}^{0.4} < 10\,\mathrm{GeV}$); Right: After constraints.

This chapter focuses on the results obtained for the three samples and the effect of different muon multiplicities on the consistency of the developed data method and a Monte Carlo counting method.

4.1 Single Top Decay

A Single Top sample (production via $\mathrm{W}^{\pm}$ exchange) was generated with at least one muon with minimum transverse momentum of 5 GeV per event (without restriction to a specific decay channel). The offline kinematic distribution in p_{T} is shown in F-4.3, with the effect of the generator requirement on the muon transverse momentum clearly visible before any further criteria were applied. The second part of the distribution below 5 GeV is due to the requirement of *at least* one muon with p_{T} above the threshold, while there is no constraint on a possible second muon in the event.

Four different $b\bar{b} \rightarrow \mu\mu\mathrm{X}$ background normalisations were added to the Single Top offline distribution (with resulting signal to background ratios: 10.0, 1.0, 0.5 and 0.1) and the requirements on offline transverse momentum and muon isolation were introduced as it was done for the $\mathrm{Z}^0/\gamma^* \rightarrow \mu\mu$ sample to ensure consistency before applying the efficiency maps for all three Trigger levels. The corresponding distribution for the sample including the constraints is shown in F-4.3 as well. The results for the efficiency weighting (integrated over η and p_{T}) are shown in direct comparison with the efficiencies from a counting method performed on the sample by directly accessing the Trigger logic in T-4.1.

As can be seen, the Trigger efficiencies obtained with the efficiency map from $\mathrm{Z}^0/\gamma^* \rightarrow \mu\mu$ are in very good agreement within the statistical uncertainties for the High-Level Trigger, while the LVL1 efficiencies are slightly higher than the ones determined with the counting method when

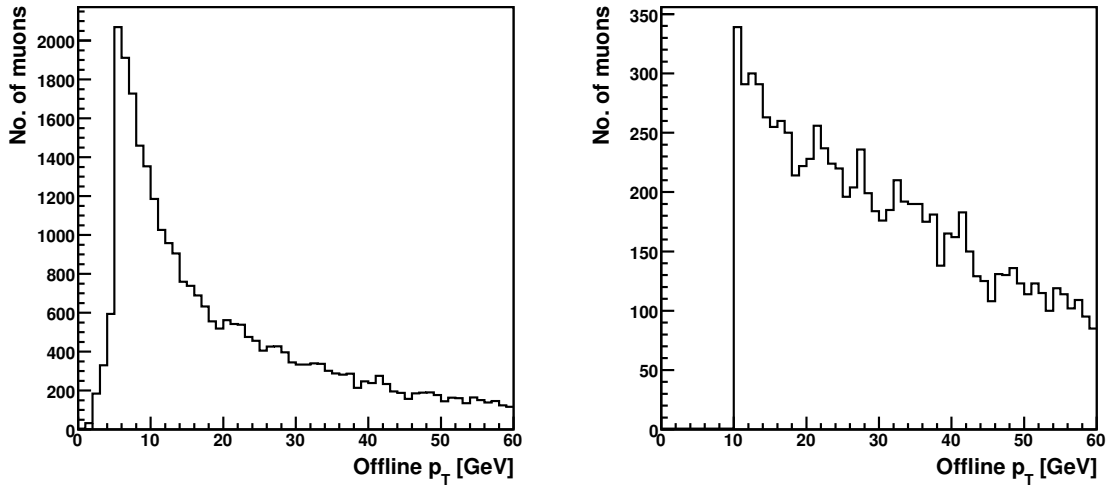

Figure F-4.3: offline kinematics in p_T for the Single Top sample. Left: Prior to constraints on transverse momentum ($p_T < 10\,\text{GeV}$) and isolation energy ($E_{ISO}^{0.4} < 10\,\text{GeV}$); Right: After constraints.

S/B	LVL1 Efficiency		LVL2 Efficiency		EF Efficiency	
	Data	counting	Data	counting	Data	counting
10.0	$75.38^{+0.33}_{-0.33}\,\%$	$75.08^{+0.34}_{-0.33}\,\%$	$79.05^{+0.44}_{-0.43}\,\%$	$78.80^{+0.44}_{-0.43}\,\%$	$96.59^{+0.26}_{-0.23}\,\%$	$96.30^{+0.26}_{-0.24}\,\%$
1.0	$57.45^{+0.33}_{-0.33}\,\%$	$56.74^{+0.34}_{-0.33}\,\%$	$59.05^{+0.44}_{-0.43}\,\%$	$58.98^{+0.44}_{-0.43}\,\%$	$95.32^{+0.26}_{-0.23}\,\%$	$95.12^{+0.26}_{-0.24}\,\%$
0.5	$50.15^{+0.33}_{-0.33}\,\%$	$49.27^{+0.34}_{-0.33}\,\%$	$46.64^{+0.44}_{-0.43}\,\%$	$46.67^{+0.44}_{-0.43}\,\%$	$94.00^{+0.26}_{-0.23}\,\%$	$93.89^{+0.26}_{-0.24}\,\%$
0.1	$39.53^{+0.33}_{-0.33}\,\%$	$38.40^{+0.34}_{-0.33}\,\%$	$19.96^{+0.44}_{-0.43}\,\%$	$20.23^{+0.44}_{-0.43}\,\%$	$85.75^{+0.26}_{-0.23}\,\%$	$86.14^{+0.26}_{-0.24}\,\%$

Table T-4.1: Integrated (η-p_T) Trigger efficiencies for the Single Top sample. All efficiencies are with respect to the prior Trigger level (or offline reconstruction level for LVL1 efficiency) and all p_T efficiencies have been corrected for detector acceptance. Statistical uncertainties are calculated according to the method described in the Appendix.

background is significantly present, with the effect mutually increasing with the background normalisation in the sample.

4.2 $t\bar{t} \rightarrow \mu\mu X$ Decay

In addition, a $t\bar{t} \rightarrow \mu\mu X$ sample was generated with at least two muons with a transverse momentum of at least 10 GeV to be present in the event to compare the results to a sample with different typical muon multiplicity in an event. The offline kinematic distribution in p_T before and after the kinematic constraints is shown in F-4.4. Again the generator constraint and its effect on the reconstructed p_T and a second part of the distribution below the threshold is visible.

The resulting efficiencies for the $t\bar{t} \rightarrow \mu\mu X$ sample obtained with the $Z^0/\gamma^* \rightarrow \mu\mu$ efficiency map after applying p_T and isolation constraints to the offline distribution of the sample with

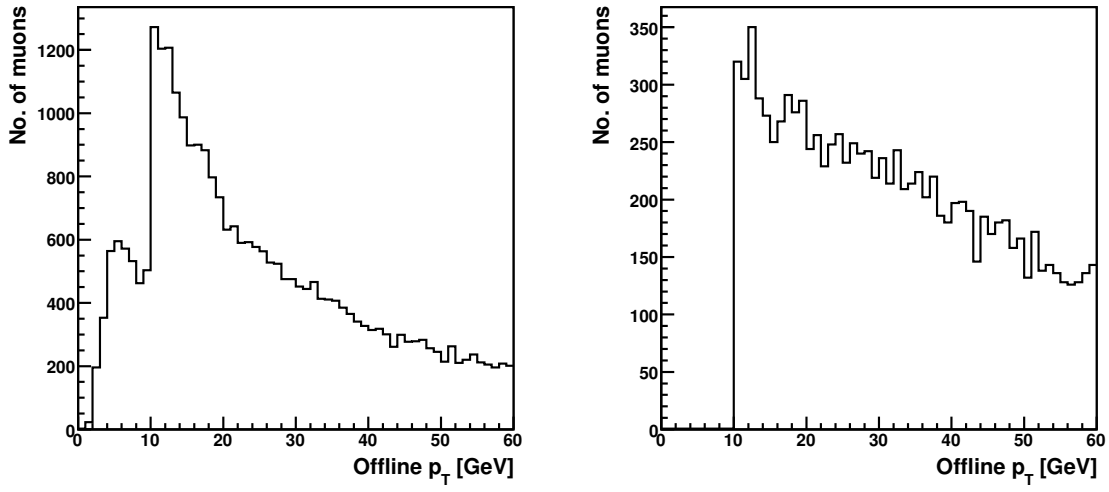

Figure F-4.4: offline kinematics in p_{T} for the $t\bar{t} \rightarrow \mu\mu$X sample. Left: Prior to constraints on transverse momentum ($p_{\mathrm{T}} < 10\,\mathrm{GeV}$) and isolation energy ($E^{0.4}_{\mathrm{ISO}} < 10\,\mathrm{GeV}$); Right: After constraints.

different signal to background ratios are shown in Table T-4.2.

S/B	LVL1 Efficiency		LVL2 Efficiency		EF Efficiency	
	Data	counting	Data	counting	Data	counting
10.0	$76.42^{+0.30}_{-0.29}\,\%$	$76.08^{+0.30}_{-0.29}\,\%$	$82.06^{+0.38}_{-0.37}\,\%$	$81.53^{+0.38}_{-0.37}\,\%$	$96.68^{+0.21}_{-0.19}\,\%$	$96.65^{+0.21}_{-0.19}\,\%$
1.0	$58.03^{+0.30}_{-0.29}\,\%$	$57.29^{+0.30}_{-0.29}\,\%$	$61.44^{+0.38}_{-0.37}\,\%$	$61.17^{+0.38}_{-0.37}\,\%$	$95.48^{+0.21}_{-0.19}\,\%$	$95.51^{+0.21}_{-0.19}\,\%$
0.5	$50.53^{+0.30}_{-0.29}\,\%$	$49.63^{+0.30}_{-0.29}\,\%$	$48.57^{+0.38}_{-0.37}\,\%$	$48.45^{+0.38}_{-0.37}\,\%$	$94.21^{+0.21}_{-0.19}\,\%$	$94.32^{+0.21}_{-0.19}\,\%$
0.1	$39.63^{+0.30}_{-0.29}\,\%$	$38.50^{+0.30}_{-0.29}\,\%$	$20.70^{+0.38}_{-0.37}\,\%$	$20.92^{+0.38}_{-0.37}\,\%$	$86.23^{+0.21}_{-0.19}\,\%$	$86.77^{+0.21}_{-0.19}\,\%$

Table T-4.2: Integrated (η-p_{T}) Trigger efficiencies for the $t\bar{t} \rightarrow \mu\mu$X sample. All efficiencies are with respect to the prior Trigger level (or offline reconstruction level for LVL1 efficiency) and all p_{T} efficiencies have been corrected for detector acceptance. Statistical uncertainties are calculated according to the method described in the Appendix.

As it was shown for the Single Top sample, the Trigger efficiencies obtained with the efficiency map method are statistically compatible with the counting method for the High-Level Trigger, while the LVL1 Trigger results show slightly higher efficiencies.

4.3 SUSY Decay

Finally, a SUSY simulation for the ATLAS performance point SU1 (coannihilation) was utilised (CSC MC production, CSC ID 005401 [56]) as a third sample to test the method on. The sample contains one to three muons per event. There where no generator constraints on the muon transverse momentum, as can be seen from the p_{T} distribution in Figure F-4.5, where no

p_T cut effects on the offline distribution are visible.

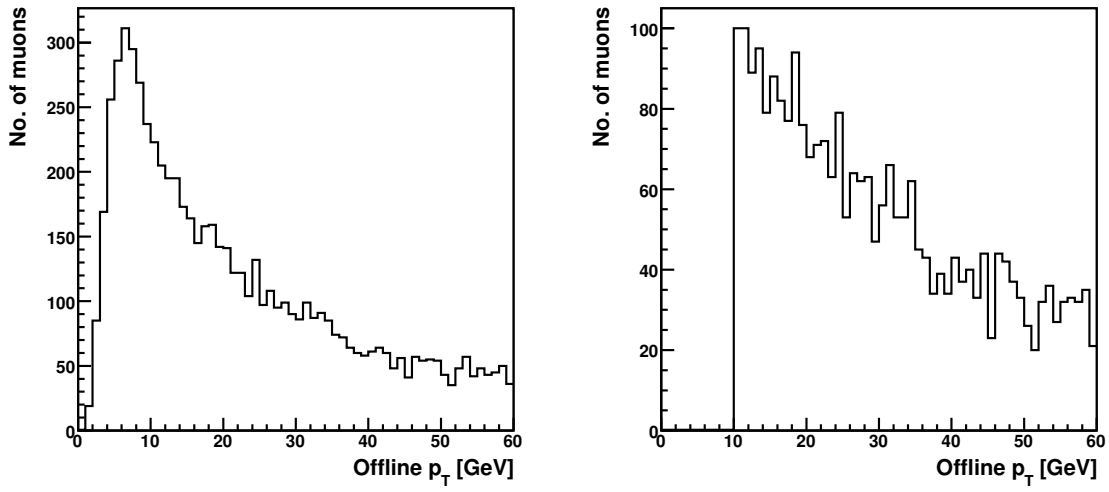

Figure F-4.5: offline kinematics in η and p_T for the SUSY sample. Left: Prior to constraints on transverse momentum ($p_T < 10\,\text{GeV}$) and isolation energy ($E_{ISO}^{0.4} < 10\,\text{GeV}$); Right: After constraints.

Like for the other samples, the results for the SUSY sample can be found in Table T-4.3, again for the efficiency map method together with the results from a Monte Carlo counting method, both performed on the different signal to background admixtures with p_T and isolation constraints applied.

S/B	LVL1 Efficiency		LVL2 Efficiency		EF Efficiency	
	Data	counting	Data	counting	Data	counting
10.0	$74.32^{+0.38}_{-0.38}\,\%$	$73.76^{+0.38}_{-0.38}\,\%$	$79.17^{+0.55}_{-0.56}\,\%$	$78.37^{+0.55}_{-0.56}\,\%$	$96.71^{+0.56}_{-0.50}\,\%$	$96.84^{+0.55}_{-0.49}\,\%$
1.0	$56.88^{+0.38}_{-0.38}\,\%$	$56.01^{+0.38}_{-0.38}\,\%$	$58.86^{+0.55}_{-0.56}\,\%$	$58.41^{+0.55}_{-0.56}\,\%$	$95.41^{+0.56}_{-0.50}\,\%$	$95.61^{+0.55}_{-0.49}\,\%$
0.5	$49.76^{+0.38}_{-0.38}\,\%$	$48.78^{+0.38}_{-0.38}\,\%$	$46.38^{+0.55}_{-0.56}\,\%$	$46.12^{+0.55}_{-0.56}\,\%$	$94.04^{+0.56}_{-0.50}\,\%$	$94.32^{+0.55}_{-0.49}\,\%$
0.1	$39.42^{+0.38}_{-0.38}\,\%$	$38.26^{+0.38}_{-0.38}\,\%$	$19.77^{+0.55}_{-0.56}\,\%$	$19.95^{+0.55}_{-0.56}\,\%$	$85.62^{+0.56}_{-0.50}\,\%$	$86.33^{+0.55}_{-0.49}\,\%$

Table T-4.3: Integrated (η-p_T) Trigger efficiencies for the SUSY sample. All efficiencies are with respect to the prior Trigger level (or offline reconstruction level for LVL1 efficiency) and all p_T efficiencies have been corrected for detector acceptance. Statistical uncertainties are calculated according to the method described in the Appendix.

The resulting efficiencies are in good agreement for LVL2 and EF as it was the case for the other processes, while the LVL1 efficiencies are again slightly higher than the results obtained with the counting method for higher background fractions in the sample.

4.4 Results & Summary

It was shown for the three test samples that the efficiencies obtained from the $Z^0/\gamma^* \rightarrow \mu\mu$ decay with the Tag & Probe method can successfully be applied to other physics processes, regardless of the underlying kinematic distributions without the need of using the Trigger information contained in the examined samples. The results are compatible with a Monte Carlo counting method within statistical uncertainties for the High-Level Trigger.

The LVL1 efficiencies determined with the data method are slightly higher than the results from the counting method, in particular for large background admixtures to the samples. The exact origin of this effect, although being small, is still under study.

Nevertheless, the observed effect might be even smaller for some physics analysis scenarios where harder requirements on transverse momentum would be set in order to restrict the analysis to a region of Trigger efficiency that is as independent from systematic effects as possible, that is the plateau region of the turn-on curve.

5 Conclusion & Outlook

This study was performed to develop a data driven method for the determination of Trigger efficiencies for muons.

It was shown that the Trigger efficiency for a single muon does not depend on its production mechanism (e.g. if the muon comes from a Z^0 decay or from any other process). Only if examining integrated quantities (e.g. in η or p_T or both) or in the case of taking into account isolation criteria the resulting efficiencies may vary, e.g. due to the loss of information when performing the integration. This was verified by comparison of two kinematically different samples (single muons, generated flat in η, ϕ and p_T and muons from a Drell-Yan subprocess, $Z^0/\gamma^* \to \mu\mu$). Furthermore, a kinematic reweighting was performed to take into account the different process kinematics, where perfect agreement was found after the reweighting process.

In order to measure Trigger efficiencies from data, a Tag & Probe method was applied to the simulated $Z^0/\gamma^* \to \mu\mu$ sample. It was shown that the Tag & Probe method can reliably obtain the Trigger efficiencies from the sample by selecting one muon and making use of the knowledge of a second muon to be present in an $Z^0/\gamma^* \to \mu\mu$ event. The obtained efficiencies were compared to the results from the Monte Carlo method performed on the same sample, with both methods being in good agreement for the p_T turn-on curve, especially in the saturation range.

In order to analyse the effect of the physics background contribution to the $Z^0/\gamma^* \to \mu\mu$ decay, several background sources were added and the Tag & Probe method was performed on the joint sample. It was shown that independent of the added background, the Tag & Probe method still yields results compatible with a Monte Carlo counting method within statistical uncertainties.

Aside from the physics background, instrumental background from fake isolated muons can affect the efficiency measurement. Since these muons only appear to be isolated, they should not be included in the actual efficiency determination (unlike the physics background). Hence, a data method to estimate the instrumental background contribution to a data sample, the Matrix Method was introduced, which relies on the efficiencies of an isolation requirement on the probe muon to determine the background fraction in the sample prior to the constraint. These efficiencies have to be independently obtained from data, where respective methods were developed and a simple closure test was performed for a signal ($Z^0/\gamma^* \to \mu\mu$) and a background ($b\bar{b} \to \mu\mu X$) sample independently.

It was shown that the Matrix Method already yields a very good estimate for the background fraction in a sample, especially when considering that the background sample used for the determination of the cut efficiency was not representative due to generator constraints on the transverse momentum of the (anti-)bottom quarks and the muon p_T. These were necessary to be able to generate a useful sample for the test within acceptable time of computation. The effect of this preselection on the resulting Matrix Method estimate was verified by analysing a different $b\bar{b} \to \mu\mu X$ sample with tighter constraints with respect to the introduced correlation of isolation of the tag and probe muons, where it could be shown that the effect increased and therefore the origin of the effect is well understood.

In addition to the methods introduced and the tests performed in this thesis, further de-

pendencies and topologies can be studied, e.g. the impact of jet multiplicities on the obtained results. Furthermore, the assumptions made in the course of this study should be verified where possible (e.g. the impact of an Underlying Event and pile-up on the isolation or the assumption of muons not to be faked at ATLAS).

In order to quantitatively improve the developed methods, additional numerical methods to compute the uncertainties of efficiencies with weights applied to the individual objects in the observed distributions could be implemented. Hence, it should be possible to preserve the underlying probability densities without having to rely on approximations that are valid only for sufficiently high statistics and cases where the efficiency is not close to zero or one. In that context, developing an appropriate parametrisation in η and p_{T} for the reweighting function and the Trigger efficiency to be measured from data instead of a binned efficiency map could further improve the results, especially with respect to discontinuities in low statistic areas.

To ensure the functionality of the developed methods for the measurement of isolation cut efficiencies on real data, the selection criteria, in particular for the signal cut efficiency, could be further enhanced to reduce background effects. A possible approach would be to apply constraints on the jet multiplicity to further tighten the $\mathrm{Z}^0/\gamma^* \rightarrow \mu\mu$ selection and to suppress especially multijet background contributions. In addition, the generation of a more representative sample used to verify the Matrix Method, e.g. by reducing the generator preselection constraints as much as possible for the simulated $b\bar{b} \rightarrow \mu\mu\mathrm{X}$ background sample would allow to further improve the verification of the performed instrumental background contribution estimation in the sample. In addition, the background selection could be further improved by utilising a b Tagging algorithm instead of the isolation criteria only.

Finally, the developed methods may be used to study other Trigger objects (electrons [52], jets, $\not{E}_T$,...) and the results could then be compared, as it was done for the results of the electron channel. As a conclusion, the determination of Trigger efficiencies from data will become more and more important when considering the upcoming ATLAS data.

A Monte Carlo Samples

All samples used in this thesis and their corresponding generator parameters alongside with their application in this document are shown in T-A.1.

Sample	Kinematics	Generator	Events	Purpose
Single μ, flat in η,ϕ,p_{T}	$p_{\mathrm{T}} < 100\,\mathrm{GeV}$	ParticleGenerator	300 505	Reweighting
$\mathrm{Z}^0/\gamma^* \to \mu\mu$	$2 \times \mu$ ($p_{\mathrm{T}} > 5\,\mathrm{GeV}$)	PYTHIA 6.403	500 000	Reweighting
Single μ, flat in η,ϕ,p_{T}	$p_{\mathrm{T}} < 100\,\mathrm{GeV}$	ParticleGenerator	100 000	Tag & Probe
$\mathrm{Z}^0/\gamma^* \to \mu\mu$	$2 \times \mu$ ($p_{\mathrm{T}} > 5\,\mathrm{GeV}$)	PYTHIA 6.403	100 000	Tag & Probe
$b\bar{b} \to \mu\mu\mathrm{X}$	$2 \times \mu$ ($p_{\mathrm{T}} > 5\,\mathrm{GeV}$) ($\mathrm{q}/\overline{\mathrm{q}}$ $p_{\mathrm{T}} > 6\,\mathrm{GeV}$)	PYTHIA 6.403	259 499	Tag & Probe
$c\bar{c} \to \mu\mu\mathrm{X}$	$2 \times \mu$ ($p_{\mathrm{T}} > 5\,\mathrm{GeV}$) ($\mathrm{q}/\overline{\mathrm{q}}$ $p_{\mathrm{T}} > 8\,\mathrm{GeV}$)	PYTHIA 6.403	48 800	Tag & Probe
$t\bar{t} \to \mu\mu\mathrm{X}$	$2 \times \mu$ ($p_{\mathrm{T}} > 5\,\mathrm{GeV}$)	PYTHIA 6.403	181 375	Tag & Probe
$\mathrm{Z}^0 \to \tau\tau \to \mu\mu\mathrm{X}$	$2 \times \mu$ ($p_{\mathrm{T}} > 5\,\mathrm{GeV}$)	PYTHIA 6.403	247 053	Tag & Probe
$\mathrm{Z}^0/\gamma^* \to \mu\mu$	$2 \times \mu$ ($p_{\mathrm{T}} > 5\,\mathrm{GeV}$)	PYTHIA 6.403	60 168	$\varepsilon^{\mathrm{SIG}}$ Method
$b\bar{b} \to \mu\mu\mathrm{X}$	$1 \times \mu$ ($p_{\mathrm{T}} > 5\,\mathrm{GeV}$) ($\mathrm{q}/\overline{\mathrm{q}}$ $p_{\mathrm{T}} > 6\,\mathrm{GeV}$)	PYTHIA 6.403	500 000	$\varepsilon^{\mathrm{FAKE}}$ Method
$b\bar{b} \to \mu\mu\mathrm{X}$	$2 \times \mu$ ($p_{\mathrm{T}} > 5\,\mathrm{GeV}$) ($\mathrm{q}/\overline{\mathrm{q}}$ $p_{\mathrm{T}} > 12\,\mathrm{GeV}$)	PYTHIA 6.403	147 242	$\varepsilon^{\mathrm{FAKE}}$ Method
$b\bar{b} \to \mu\mu\mathrm{X}$	$1 \times \mu$ ($p_{\mathrm{T}} > 5\,\mathrm{GeV}$) ($\mathrm{q}/\overline{\mathrm{q}}$ $p_{\mathrm{T}} > 6\,\mathrm{GeV}$)	PYTHIA 6.403	130 014	Closure Tests
Single Top	$1 \times \mu$ ($p_{\mathrm{T}} > 5\,\mathrm{GeV}$)	PYTHIA 6.403	32 000	Closure Tests
$t\bar{t} \to \mu\mu\mathrm{X}$	$2 \times \mu$ ($p_{\mathrm{T}} > 10\,\mathrm{GeV}$)	PYTHIA 6.403	30 400	Closure Tests
SUSY (SU1)	*Taken from CSC Production (005401)*		130 014	Closure Tests

Table T-A.1: Generated Monte Carlo samples. Abbreviations: Tag & Probe: Used to test the Tag & Probe method in comparison to the counting method in Chapter 3; Reweighting: Used as independent sample for the reweighting of single muons to the $\mathrm{Z}^0/\gamma^* \to \mu\mu$ kinematic in Chapter 3; $\varepsilon^{\mathrm{SIG}}/\varepsilon^{\mathrm{FAKE}}$ Method: Used for the closure tests performed for the Matrix Method in Chapter 3; Closure Tests: Used as sample for the application of the methods performed in Chapter 4.

B Calculation of Trigger Efficiency Uncertainties

B.1 A Frequentist Approach to Trigger Efficiency Uncertainties

A common approach to calculate statistical uncertainties for (Trigger) efficiencies is to consider the determination of the efficiency ε as Bernoulli Experiment (two possible outcomes for each element, triggered or not triggered), hence defining the efficiency ε for k triggered out of n objects:

$$\varepsilon = \frac{k}{n} \tag{B.1}$$

The probability of having exactly k out of n triggered objects for given efficiency ε obeys a Binomial distribution:

$$p(k) = \binom{n}{k} \varepsilon^k (1-\varepsilon)^{n-k} \tag{B.2}$$

In the following, the average and the variance as a measure of the spread respectively the statistical uncertainty of the Binomial distribution will be derived for completeness.

To compute the average, the expectation value $\sum_k kp(k)$ of the Binomial distribution can be computed:

$$\begin{aligned} < p(k) > &= \sum_{k=0}^{n} k \binom{n}{k} \varepsilon^k (1-\varepsilon)^{n-k} \\ &= \sum_{k=0}^{n} k \frac{n!}{(n-k)!k!} \varepsilon^k (1-\varepsilon)^{n-k} \end{aligned} \tag{B.3}$$

Extracting $n\varepsilon$ from the sum and dropping the $k = 0$ term (which is zero):

$$\begin{aligned} < p(k) > &= n\varepsilon \sum_{k=1}^{n} \frac{(n-1)!}{(n-k)!(k-1)!} \varepsilon^{k-1} (1-\varepsilon)^{n-k} \\ &= n\varepsilon \sum_{k=1}^{n} \binom{n-1}{k-1} \varepsilon^{k-1} (1-\varepsilon)^{(n-1)-(k-1)} \end{aligned} \tag{B.4}$$

Substituting $m = k - 1$ and $l = n - 1$:

$$\begin{aligned} < p(k) > &= n\varepsilon \sum_{m=0}^{n-1} \binom{n-1}{m} \varepsilon^m (1-\varepsilon)^{(n-1)-m} \\ &= n\varepsilon \sum_{m=0}^{l} \binom{l}{m} \varepsilon^m (1-\varepsilon)^{l-m} \end{aligned} \tag{B.5}$$

The sum is the Binomial expansion of the probability that the Bernoulli Experiment has an outcome at all (triggered or non-triggered) $[p + (1 - p)]^n = 1$ and thus

$$\begin{aligned} < p(k) > &= n\varepsilon \underbrace{\sum_{m=0}^{l} \binom{l}{m} \varepsilon^m (1-\varepsilon)^{l-m}}_{=1} \\ &= n\varepsilon \end{aligned} \tag{B.6}$$

This is just the predicted number of occurrences at a given value or bin.

To find the variance as a measure for the statistical uncertainty, consider

$$< p(k)(p(k)-1) >= \sum_{k=0}^{n} k(k-1) \binom{n}{k} \varepsilon^k (1-\varepsilon)^{n-k} \tag{B.7}$$

Taking out the factor $\varepsilon^2 n(n-1)$, dropping the $k = 0$ and $k = 1$ terms (which are now both zero) and substituting $m = k - 2$ and $l = n - 2$ and using that the sum is again 1, it follows:

$$\begin{aligned} < p(k)^2 - p(k) > &= \varepsilon^2 n(n-1) \underbrace{\sum_{m=0}^{l} \binom{l}{m} \varepsilon^m (1-\varepsilon)^{l-m}}_{=1} \\ &= \varepsilon^2 n(n-1) \end{aligned} \tag{B.8}$$

Using $< p(k) >= n\varepsilon$ and the fact that independent random variables are sampled:

$$\begin{aligned} < (p(k) - < p(k) >)^2 > &= \varepsilon^2 n(n-1) + n\varepsilon - (n\varepsilon)^2 \\ \sigma^2 &= n\varepsilon(1-\varepsilon) \end{aligned} \tag{B.9}$$

This yields the Binomial error for a given efficiency ε:

$$\sigma_n = \frac{\sigma}{n} = \frac{\sqrt{n\varepsilon(1-\varepsilon)}}{n} = \sqrt{\frac{\varepsilon(1-\varepsilon)}{n}} \tag{B.10}$$

Unfortunately, this (simplified) error model has two major deficiencies:

- The obtained uncertainty is symmetric and does not reflect the underlying asymmetric Binomial distribution, which is in particular the case for low statistics and for efficiencies close to zero or one.

- For certain cases, the resulting uncertainties are unrealistic. For efficiencies approaching $\varepsilon = 0$ or $\varepsilon = 1$, the resulting variance vanishes, with the extreme cases of zero and n out of n objects triggered, where the variance is zero, independent of the available statistics, as shown in Figure F-B.1.

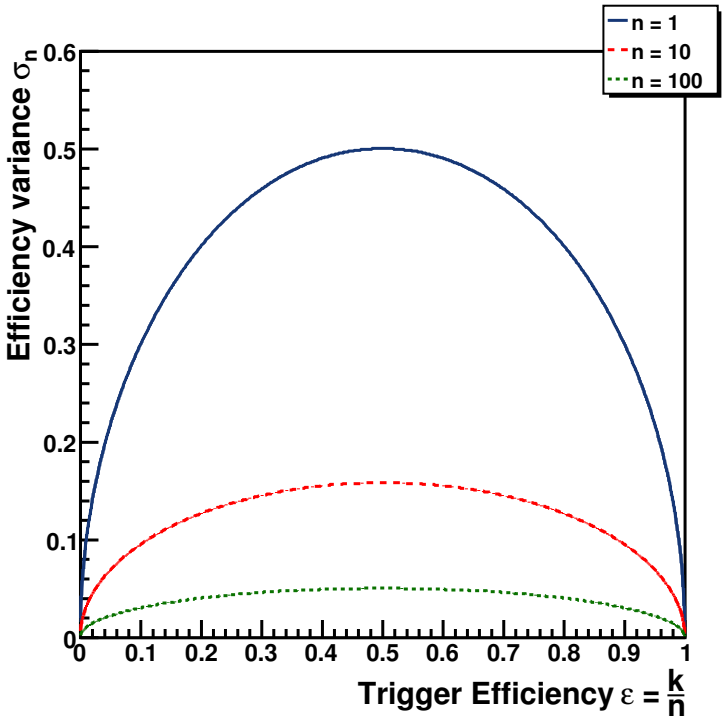

Figure F-B.1: Variance of the Binomial distribution as function of efficiency, as it was derived in Equation B.10, plotted for three different values for the denominator of the efficiency, n. The uncertainties for very high and very low efficiencies always approach zero, independent of the underlying statistics.

B.2 A Bayesian Approach to Trigger Efficiency Uncertainties

Alternatively, different Frequentist (e.g. Likelihood methods) and non-Frequentist approachs can be used to determine the uncertainties for the Trigger efficiency. In this case, a Bayesian approach was chosen to account for the asymmetry introduced by the Binomial distributed variables and to solve the problematic of boundary effects as well. Data analysis from a Bayesian perspective has been discussed in the literature [57–59]. Bayesian inference uses aspects of the examined scientific method, which involves collecting evidence that is meant to be consistent or inconsistent with a given hypothesis. The underlying Bayes' Theorem relates the conditional and marginal probabilities of two random events, being often used to compute posterior probabilities given observations. The Bayes' Theorem for probability densities $f(x)$ and $f(y)$ is given by:

$$f(x|y) = \frac{f(x,y)}{f(y)} = \frac{f(y|x)f(x)}{f(y)} \tag{B.11}$$

The Bayesian probability density for the particular case of an efficiency ε, given k and n, is

$$p(\varepsilon|k,n) = \frac{p(k,n|\varepsilon)\cdot p_0(\varepsilon)}{\int p(k,n|\varepsilon)\cdot p_0(\varepsilon)\,d\varepsilon}, \tag{B.12}$$

with $p(k,n|\varepsilon)$ being the probability density for k and n given ε and $p_0(\varepsilon)$ the a priori probability to have the efficiency ε. In this case, these a priori probabilities are considered flat, and thus:

$$p(\varepsilon|k,n) = \frac{p(k,n|\varepsilon)}{\int p(k,n|\varepsilon)\,d\varepsilon}. \tag{B.13}$$

The probability density for k and n given ε obeys a Binomial distribution as shown in Equation B.2:

$$p(k,n|\varepsilon) = \binom{n}{k}\varepsilon^k(1-\varepsilon)^{n-k},$$

yielding the probability density for ε, given k and n:

$$\begin{aligned} p(\varepsilon|k,n) &= \frac{\binom{n}{k}\varepsilon^k(1-\varepsilon)^{n-k}}{\int_0^1 \binom{n}{k}\varepsilon^k(1-\varepsilon)^{n-k}\,d\varepsilon} \\ &= \frac{\varepsilon^k(1-\varepsilon)^{n-k}}{\int_0^1 \varepsilon^k(1-\varepsilon)^{n-k}\,d\varepsilon}, \end{aligned} \tag{B.14}$$

where the integration has to be performed over the whole allowed ε range as a normalisation.

The Binomial probability and the integral in the denominator can be solved numerically for large n, yielding a probability distribution that preserves all information of the process. A practical approach to apply this to the Trigger efficiencies determined in this analysis involves the computation of the probability distribution as derived in Equation B.14 for each bin of the analysed efficiency parametrisation as follows:

- Filling a histogram with sufficient amount of bins ($> 1\,000$) with the values from the distribution in the numerator of Equation B.14. These are calculated with an C++ arbitrary precision library (GNU MP Bignum Library [60]) for large n.
- Extraction of the value of the normalisation integral from the histogram (area under the distribution).
- Determination of the 15.86 % and 84.15 % quantiles (In analogy to the 1σ region of a Gaussian probability distribution. This convention ensures convergence of the obtained uncertainties to Gaussian / Binomial uncertainties for symmetric distributions) from the histogram as uncertainties on the efficiency.

B.2.1 Low Statistics Example

Let $k = 4$, $n = 7$. The resulting probability distribution is shown in Figure F-B.2. The efficiency and the corresponding uncertainties for this case are given by:

$$\varepsilon_{\mathrm{B}}(4,7) = 57^{+15}_{-19}\,\%,$$

while the simplified approach yields

$$\varepsilon_{\mathrm{F}}(4,7) = 57 \pm 19\,\%.$$

Aside from being a symmetric estimate for the uncertainty, this approach clearly overestimates the upper bound on the efficiency due to the assumptions of the error model.

B.2.2 High Statistics Example

To show the relevance of an asymmetric approach for higher statistics cases, let $k = 9990$, $n = 10000$. The resulting probability distribution is shown in Figure F-B.3. The efficiency and the corresponding uncertainties for this case are given by:

$$\varepsilon_{\mathrm{B}}(9990,10000) = 99.00^{+0.22}_{-0.43}\,\%,$$

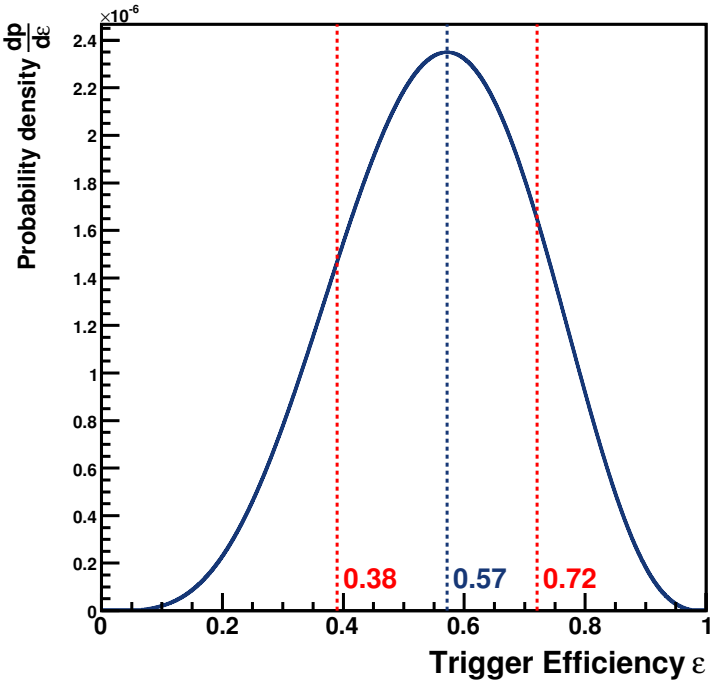

Figure F-B.2: Probability density for the efficiency given $k = 4$, $n = 7$. As can be seen, the distribution is not symmetric. In addition to the mode, the 15.86 % and 84.15 % quantiles, used as uncertainties on the efficiency, are shown.

while the simplified approach yields

$$\varepsilon_{\mathrm{F}}(9990, 10000) = (99.00 \pm 0.10)\ \%,$$

not only neglecting the underlying asymmetry but underestimating both bounds on the efficiency in this case as well.

B.3 Calculation of Uncertainties with Weights

For objects with weights applied to, in particular if each object gets weighted individually, a Binomial distribution and the described Bayesian approach is no longer applicable due to the fact that the resulting quantities (e.g. bin contents) are no longer integer numbers. Moreover, the resulting weighted values do not reflect the underlying statistics (e.g. if an entry gets weighted with a factor 10.0, this does not imply that the statistical uncertainty in this case gets reduced).

Hence, a different approach has to be made in the particular case of weighted objects to determine the uncertainty on the efficiency. First, the uncertainty on the weights has to be determined. Let a be the observed amount of objects (e.g. in a certain bin of η and p_{T}) for a process A and b the observed amount of objects for a second process B. The weight w is then determined as

$$w = \frac{a}{b} \tag{B.15}$$

or vice versa, depending on the direction of the performed weighting. Since both values are statistically uncorrelated and are obtained by counting objects, the underlying probability densities

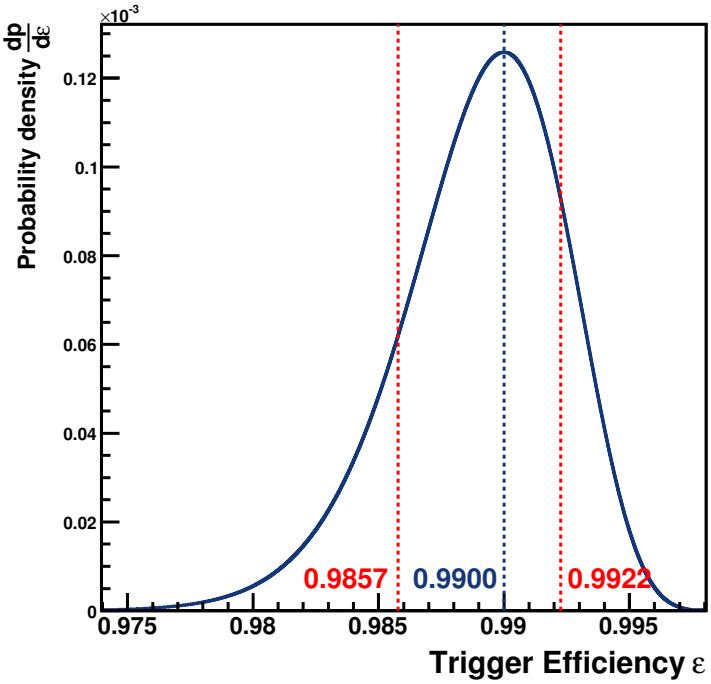

Figure F-B.3: Probability density for the efficiency given $k = 9990$, $n = 10000$. As can be seen, the distribution is not symmetric although this is a high statistics example, being close to an efficiency of one. In addition to the mode, the 15.86 % and 84.15 % quantiles, used as uncertainties on the efficiency, are shown.

obey Poisson distributions, so the corresponding uncertainties for the entries a, b are given by:

$$\sigma_a = \sqrt{a} \qquad \text{and} \qquad \sigma_b = \sqrt{b} \tag{B.16}$$

Assuming a and b to be sufficiently large, a Gaussian Error Propagation can be done, yielding for the uncertainty on the weight w:

$$\begin{aligned} \sigma_w &= \sqrt{a\left(\frac{1}{b}\right)^2 + b\left(\frac{a}{b^2}\right)^2} \\ &= \sqrt{\frac{a(b+a)}{b^3}} \end{aligned} \tag{B.17}$$

Now let v_k be the weights of the $k = 1, .., n$ accepted objects and let w_l be the weights of the $l = 1, .., m$ rejected objects in the Trigger decision. The resulting efficiency is then given by

$$\varepsilon = \frac{\sum_{k=1}^{n} v_k}{\sum_{k=1}^{n} v_k + \sum_{l=1}^{m} w_l} \equiv \frac{\sum_{k=1}^{n} v_k}{W}, \tag{B.18}$$

with

$$W = \sum_{k=1}^{n} v_k + \sum_{l=1}^{m} w_l$$

Now, assuming the v_k and w_l to be statistical uncorrelated and having uncertainties σ_{v_k} respectively σ_{w_l}, a Gaussian Error Propagation yields:

$$\sigma_\varepsilon = \sqrt{\sum_{k=1}^{n}\left[\sigma_{v_k}^2\left(\frac{\sum_{l=1}^{m} w_l}{W^2}\right)^2\right] + \sum_{l=1}^{m}\left[\sigma_{w_l}^2\left(\frac{\sum_{k=1}^{n} v_k}{W^2}\right)^2\right]} \tag{B.19}$$

Although this approach assumes the uncertainties to be Gaussian distributed and thus neglects the underlying asymmetry of the observed situation, it allows for the consideration of weighted objects and in particular of uncertainties on the individual weights.

Bibliography

[1] S. L. Glashow, *Partial Symmetries of Weak Interactions*, Nucl. Phys. **22** (1961) 579.

[2] S. Weinberg, *A Model of Leptons*, Phys. Rev. Lett. **19** (1967) 1264.

[3] A. Salam, *Weak and Electromagnetic Interactions*, in: W. Svartholm, editor, *Elementary Particle Theory*, Stockholm, (1968), Almquist and Wiksell, 1968 367.

[4] H. D. Politzer, *Reliable Pertubative Results for Strong Interactions?*, Phys. Rev. Lett. **30** (1973) 1346.

[5] D. J. Gross and F. Wilczek, *Ultraviolet Behaviour of Non-Abelian Gauge Theories*, Phys. Rev. Lett. **30** (1973) 1343.

[6] H. Fritzsch and M. Gell-Mann, *Current algebra: Quarks and what else?*, eConf **C720906V2** (1972) 135, `hep-ph/0208010`.

[7] F. Abe *et al.*, *Observation of Top Quark Production in $p\overline{p}$ Collisions with the Collider Detector at Fermilab*, Phys. Rev. Lett. **74(14)** (1995) 2626.

[8] S. Abachi *et al.*, *Observation of the Top Quark*, Phys. Rev. Lett. **74(14)** (1995) 2632.

[9] P. W. Higgs, *Broken Symmetries and the Masses of Gauge Bosons*, Phys. Rev. Lett. **13(16)** (1964) 508.

[10] G. S. Guralnik, C. R. Hagen, and T. W. B. Kibble, *Global Conservation Laws and Massless Particles*, Phys. Rev. Lett. **13(20)** (1964) 585.

[11] D. Griffiths, *Introduction to Elementary Particle Physics*, Wiley, (1987).

[12] F. Halzen and A. D. Martin, *Quarks & Leptons*, Wiley, (1984).

[13] W.-M. Yao *et al.*, *Review of Particle Physics*, J. Phys. G: Nucl. Part. Phys. **33(1)** (2006).

[14] The Tevatron Electroweak Working Group, *Combination of CDF and DØ Results on the Mass of the Top Quark*, (2008), publication in preparation.

[15] A. J. Buras, J. R. Ellis, M. K. Gaillard, and D. V. Nanopoulos, *Aspects of the Grand Unification of Strong, Weak and Electromagnetic Interactions*, Nucl. Phys. **B135** (1978) 66.

[16] S. Profumo and P. Ullio, *The role of antimatter searches in the hunt for supersymmetric dark matter*, JCAP **0407** (2004) 006, `hep-ph/0406018`.

[17] The LHC Machine Group reported by G. Brianti at theXVth Interm. conf. on High Energy Accelerators, Hamburg, Germany, *Status report on the CERN Large Hadron Collider (LHC)*, (1992), CERN/AC-DI/92-03 (LHC).

[18] CERN Document Server, *http://cdsweb.cern.ch/*, (2008).

[19] The ATLAS Collaboration, *ATLAS Detector and Physics Performance Technical Design Report - Volume I*, (1999).

[20] The CMS Collaboration, *CMS Physics Technical Design Report - Volume I*, (2006).

[21] The LHCb Collaboration, *LHCb Technical Proposal*, (1998).

[22] The ALICE Collaboration, *Technical Proposal for A Large Ion Collider Experiment at the CERN LHC*, (1995).

[23] The TOTEM Collaboration, *TOTEM Technical Design Report*, (2004).

[24] The LHCf Collaboration, *Technical Proposal for the CERN LHCf Experiment*, (2005).

[25] The ATLAS Experiment, *http://atlas.ch/*, (2008).

[26] ATLAS Trigger/DAQ Group, *ATLAS Computing Technical Design Report*, (2005).

[27] The ZEUS Collaboration, M. Derrick *et al.*, *Measurement of the proton structure function F_2 in e^+ p scattering at HERA*, Phys. Lett. **B316** (1993) 412.

[28] ATLAS Inner Detector Community, *ATLAS Inner Detector Technical Design Report*, (1997).

[29] The ATLAS Collaboration, *ATLAS Detector Paper, Draft 4*, (2007), publication in preparation.

[30] U. Egede, *The search for a standard model Higgs at the LHC and electron identification using transition radiation in the ATLAS tracker*, Ph.D. thesis, Lund University, (1997).

[31] The ATLAS Collaboration, *Calorimeter Performance Technical Design Report*, (1997).

[32] The ATLAS Collaboration, *Liquid Argon Calorimeter Technical Design Report*, (1996).

[33] The ATLAS Muon Collaboration, *ATLAS Muon Spectrometer Technical Design Report*, (1997).

[34] ICRU Report No. 49, *Stopping Powers and Ranges for Protons and Alpha Particles*, (1993).

[35] D. E. Groom, N. V. Mokhov, and S. I. Striganov, *Mass-Ratio Method Applied to the Measurement of L-Meson Masses and the Energy Balance in Pion Decay*, Atomic Data and Nuclear Data Tables **78(2)** (2001) 183.

[36] W. H. Barkas, W. Birnbaum, and F. M. Smith, *Mass-Ratio Method Applied to the Measurement of L-Meson Masses and the Energy Balance in Pion Decay*, Phys. Rev. **101(2)** (1956) 778.

[37] ATLAS Magnet Project Collaboration, *Central Solenoid Technical Design Report*, (1997).

[38] ATLAS Magnet Project Collaboration, *Barrel Toroid Technical Design Report*, (1997).

[39] ATLAS Level-1 Trigger Group, *Level-1 Trigger Technical Design Report*, (1998).

[40] ATLAS HLT/DAQ/DCS Group, *High-Level Trigger, Data Acquisition and Controls Technical Design Report*, (2003).

[41] The ATLAS Computing Workbook, *https://twiki.cern.ch/twiki/bin/view/Atlas/WorkBook*, (2008).

[42] *GAUDI: A Software Architecture and Framework for building HEP Data Processing Applications - CHEP 2000 proceedings*, (2000).

[43] T. Sjöstrand, P. Edén, C. Friberg, L. Lönnblad, G. Miu, S. Mrenna, and E. Norrbin, *High-Energy-Physics Event Generation with PYTHIA 6.1*, Computer Physics Commun. **135(238)** (2001).

[44] S. Frixione and B. R. Webber, *Matching NLO QCD computations and parton shower simulations*, Journal of High Energy Physics **2002(06)** (2002) 029.

[45] S. Frixione, P. Nason, and B. R. Webber, *Matching NLO QCD and parton showers in heavy flavour production*, Journal of High Energy Physics **2003(08)** (2003) 007.

[46] M. Dobbs and J. Hansen, *HepMC: a C++ Event Record for Monte Carlo Generators*, Computer Physics Commun. **134(41)** (2001).

[47] S. Agostinelli, J. Allison, K. Amako, J. Apostolakis, H. Araujo, P. Arce, M. Asai, D. Axen, S. Banerjee, G. Barrand, F. Behner, L. Bellagamba, J. Boudreau, L. Broglia, A. Brunengo, H. Burkhardt, S. Chauvie, J. Chuma, R. Chytracek, and G. C. et al., *GEANT 4 - a simulation toolkit*, Nuclear Instruments and Methods in Physics Research Section A **506(3)** (2003).

[48] E. Richter-Wąs, D. Froidevaux, and L. Poggioli, *ATLFAST 2.0 - A Fast Simulation Package For ATLAS*, (1998), ATLAS Note ATL-PHYS-98-131.

[49] Top level tags in the ATLAS Geometry Database, *https://twiki.cern.ch/twiki/bin/view/Atlas/AtlasGeomDBTags/*, (2008).

[50] ROOT: An Object-Oriented Data Analysis Framework, *http://root.cern.ch/*, (2008).

[51] S. D. Drell and T.-M. Yan, *Massive Lepton-Pair Production in Hadron-Hadron Collisions at High Energies*, Phys. Rev. Lett. **25(5)** (1970) 316.

[52] S. Mättig, *Effizienzbestimmung des Elektrontriggers am ATLAS Experiment*, Diploma Thesis, Institut f. Experimentalphysik, Universität Hamburg, (2007).

[53] M. Klute, *A Measurement of the $t\bar{t}$ Production Cross Section in Proton-Antiproton Collisions at $\sqrt{s} = 1.96\,\text{TeV}$ with the DØ Detector at the Tevatron using Final States with a Muon and Jets*, Universität Bonn, (2004).

[54] A. Caldwell, D. Kollar, and K. Kröninger, *BAT - The Bayesian Analysis Toolkit*, publication in preparation.

[55] J. Wess and B. Zumino, *Supergauge Transformations in Four-Dimensions*, Nucl. Phys. **B70** (1974) 39.

[56] MC Production status for SUSY CSC works, *https://twiki.cern.ch/twiki/bin/view/Atlas/SusyCscMcProduction/*, (2008).

[57] G. D'Agostini, *Bayesian Reasoning in Data Analysis*, World Scientific Publishing Company, (2003).

[58] D. S. Sivia, *Data Analysis. A Bayesian Tutorial*, Oxford University Press, (2006).

[59] E. T. Jaynes, *Probability Theory - The Logic of Science*, Cambridge University Press, (2003).

[60] The GNU MP Bignum Library, *http://gmplib.org/*, (2008).

Acknowledgements

Foremost, I would like to express my sincere gratitude to Prof. Dr. Arnulf Quadt, who has been my supervisor since the beginning of my study. He provided me with many helpful suggestions, important advice and constant encouragement during the course of this work.

On top of that, I would like to thank Prof. Dr. Markus Klute for consenting to be co-referee to this thesis.

I also like to thank Dr. Carsten Hensel and Dr. Jörg Meyer for supporting me during the time of my studies and for continuously providing constructive advice, numerous ideas and very helpful discussions. A special thank goes to both of them as well as to Dr. Michael Uhrmacher for the extensive proofreading of this thesis.

A special thank goes to all of my colleagues at the 2^{nd} Institute of Physics and in particular to Kevin Kröninger, Matthias Stein and Kathrin Störig for countless helpful discussions and support during my work.

Sincere thanks are extended to one of my best friends, Christian Bambach, who helped me proofreading this work with respect to language issues and added a very helpful *Non-Physicist's* view to the proofing process. Moreover, I particularly would like to thank him for providing diversion from work whenever I was in need of.

Furthermore, I would like to express my deepest gratitude to those who have helped keeping away "real life" problems from me to the best possible during my time of writing this thesis.

I cannot finish without saying how grateful I am with my parents, Günter Fuchs and Brigitte Kohn. They have always supported and encouraged me to do my best in all matters of life.